

Design of novel radiating elements for SATCOM phased arrays in Ku-Band

THÈSE N° 6921 (2016)

PRÉSENTÉE LE 21 JANVIER 2016

À LA FACULTÉ DES SCIENCES ET TECHNIQUES DE L'INGÉNIEUR
LABORATOIRE D'ÉLECTROMAGNÉTISME ET ANTENNES
PROGRAMME DOCTORAL EN GÉNIE ÉLECTRIQUE

ÉCOLE POLYTECHNIQUE FÉDÉRALE DE LAUSANNE

POUR L'OBTENTION DU GRADE DE DOCTEUR ÈS SCIENCES

PAR

Baptiste Fernand HORNECKER

acceptée sur proposition du jury:

Prof. A. Rufer, président du jury
Prof. J. R. Mosig, Dr N. Vukadinovic, directeurs de thèse
Prof. X. Begaud, rapporteur
Dr I. Stevanovic, rapporteur
Prof. F. Rachidi-Haeri, rapporteur



ÉCOLE POLYTECHNIQUE
FÉDÉRALE DE LAUSANNE

Suisse
2016

*Point n'est besoin d'espérer¹ pour entreprendre²
ni de réussir³ pour persévérer⁴.*

— *Guillaume le Taciturne (interprétation personnelle)*

(1) de bons résultats

(2) des simulations

(3) ses mesures

(4) à produire des prototypes

Je dédie cette thèse à ma famille.

Acknowledgements

My first thanks are for Dassault Aviation who supported financially most of this work through a 3-years contract with LEMA-EPFL. The last six months were generously supported by the IC1102 COST VISTA action, a european framework for the development of technologies and sciences.

Warm thanks are going to my two thesis directors, Juan R. Mosig and Nicolas Vukadinovic who made the whole adventure possible. Immediately after, follows Olivier Calvo-Perez, a Dassault engineer who was in particular my main supervisor during the two-months internship in St-Cloud. I am also thinking of Roberto Torres-Sanchez, the first researcher who allowed me to start my PhD with a proper methodology, and was very helpful for finding the right directions.

I shall be grateful then to the LEMA as a whole, without citing any name in particular (in this way, I won't forget anyone !), for the outstanding daily working environment. It is exceptional to find a place where work can become a pleasure to such an extent.

Next come the other jury members who accepted to carefully evaluate my work and to provide the final comments and improvement guidelines : Xavier Begaud, Ivica Stevanovic, Farhad Rachidi-Haeri and Alfred Rufer.

It would be unfair not to say a word about the workshop crew that made all the prototyping processes possible. One does not always have the chance to have such a high quality PCB production just next to its research laboratory, and they deserve to be mentioned for their patience every time practical issues and complicated situations raised.

Last but not least, the family. Geneviève Michaud together with my Parents, frequently ensured the presence of a human warmth at home and broke the monotony of the researcher's life. For this I have to be eternally thankful to them.

Lausanne, 14 October 2015

Baptiste HORNECKER.

Abstract

The present thesis deals with the design of a planar antenna array for the communication between a civil aircraft (Dassault Aviation's Falcon) and an Inmarsat satellite. The final goal is to provide high speed Internet access in X/Ku-Band (8-12GHz / 12-18GHz), and possibly even in K/Ka-Band (18-27GHz / 17-40GHz). The study starts with the Ku-Band only, then evolves towards the transmission band and finishes with their Ka-Band counterparts. The main constraint of the thesis is that the final result should be a low profile antenna that will be easy to integrate below the fuselage of an aircraft. At the same time, the antenna has to provide a beam steering mechanism in order to track the position of the targetted satellite while the aircraft is moving. The usual way to achieve it is to implement some dedicated electronic chips below each radiating element of array.

Dassault Aviation has its own alternate and more mechanical oriented solutions. Since the communication system is intended for top-notch business jets produced in small series, cost is not here a decisive criterion. This thesis assumes the existence of the beam-steering system and concentrates on a proof of concept and careful design of the antenna elements that will constitute the final array. They have to satisfy tight constraints in terms of size, return loss, mutual coupling with neighbors, efficiency, radiation pattern and dual circular polarization quality. Printed multilayer antennas have been retained as the best candidates, and the main parts of the thesis have been dedicated to their study.

The thesis concludes with the presentation of an apparently completely unrelated and independent topic, namely the simulation of nanoscale 2D planar structures based on Graphene. The rationale for this last chapter is to provide a prospective study of the use of Graphene to create a variable capacitance. This component is always needed in the beamforming network of reconfigurable and scanning arrays. Our laboratory is developing a deep knowledge of the electromagnetic properties of Graphene-based devices and these varicaps could lead to very interesting applications in high frequencies, once the Graphene technology has definitely progressed. Thanks to electrostatics Green's functions, a variable capacitor based on Graphene has been simulated, and a Quantum effect -the Quantum capacitance of Graphene- has been successfully tackled from a numerical point of view.

Key words: Satellite Communications, Ku-Band, Ka-Band, Phased Array, Dual Circular Polarisation, Sequential Rotation, Multilayer Printed Circuits, Dielectric Resonator Antennas, Green's Function, Graphene, Quantum Capacitors

Résumé

Ce travail de thèse s'intéresse à la conception d'un réseau d'antennes pour établir une communication entre un avion civil (le Falcon de Dassault Aviation) et un satellite Inmarsat. L'objectif est de fournir une liaison Internet haut débit en bande Ku, et même potentiellement en bande Ka. L'étude commence par la bande de réception seule, puis évolue vers la bande de transmission et termine enfin par leurs transpositions respectives en bande Ka. La contrainte principale de cette thèse est de produire une antenne conforme aussi compacte que possible pour une intégration plus aisée sous le fuselage de l'avion. En même temps, cette dernière doit fournir un mécanisme de balayage du faisceau pour garder le contact avec le satellite souhaité durant le voyage. La manière habituelle de procéder dans ce cas est d'employer des puces électroniques dédiées sous chaque élément rayonnant du réseau.

Dassault Aviation dispose de ses propres solutions mécaniques; du fait que ce projet est destiné à des avions haut de gamme produits en faible quantité, le coût n'est pas ici un critère décisif. Il est supposé dans cette thèse que le système de dépointage du faisceau est disponible, pour pouvoir se concentrer sur la conception des éléments qui constitueront le réseau final. Ils doivent satisfaire à des contraintes fortes en termes de taille, d'adaptation d'impédance, de couplage mutuel avec les voisins, de rendement, de diagramme de rayonnement et enfin de qualité de la double polarisation circulaire. Les antennes imprimées multi-couches ont été retenues comme étant les meilleurs candidats, et la plus grande partie du travail est dédié à leur étude.

La thèse se conclut sur un sujet apparemment éloigné de celui des antennes, à savoir la simulation de nano-structures 2D planaires basées sur du Graphène. La raison d'être de ce dernier chapitre est d'étudier l'emploi possible du Graphène pour créer des capacités variables. Ce composant est toujours requis pour la conception de réseaux d'antennes reconfigurables ou à balayage. Notre laboratoire est en train de développer un savoir-faire dans la manipulation des propriétés électromagnétiques du Graphène et ces varicaps pourraient trouver des applications à hautes fréquences, dès que le Graphène atteindra un niveau de maturité suffisant. Grâce aux fonctions de Green électrostatiques, une capacité variable a été ainsi simulée et un effet Quantique -la capacité Quantique du Graphène- a été caractérisée numériquement.

Mots clefs: Communications par Satellite, Bande Ku, Bande Ka, Réseau d'Antennes, Polarisation Circulaire Double, Rotation Séquentielle, Circuits Imprimés Multicouche, Antennes à Résonateur Diélectrique, Fonction de Green, Graphène, Capacité Quantique

Contents

Acknowledgements	i
Abstract (English/Français)	iii
List of figures	ix
List of tables	xiii
1 Introduction	1
1.1 Main targets of the thesis	1
1.2 A previous project as a starting point : NATALIA	6
1.3 Thesis organisation and original contributions	8
2 Global architecture of the array	9
2.1 Series feeding : The beam squinting effect and its consequences	9
2.2 Vertical corporate feeding	15
2.3 The beam steering system	19
2.3.1 A first solution using mechanical delay lines	19
2.3.2 A bibliographic review of beam steering systems	23
2.3.3 A recent SIW-based mechanical system	27
3 A first Rx-Band Element	29
3.1 Generalities about circularly polarized planar antennas	30
3.1.1 Some definitions about the Axial Ratio	30
3.1.2 General properties of patch antennas	33
3.1.3 Design of a stacked patch antennas	36
3.2 Choice and modification of a directional coupler	42
3.3 A first complete antenna element	49
4 Improving the Axial Ratio of a planar array	51
4.1 Sequential rotations in principles	53
4.2 Sequential feeding at element scale	55
4.3 A novel patch antenna sequentially-fed through a circular slot	57
4.4 Design of a feeding system for the antenna	62
4.4.1 A survey of existing phase shifter topologies	62

Contents

4.4.2	A simpler and more compact solution using Wilkinson splitters	67
5	Dielectric Resonator Antennas (DRA)	77
5.1	Generalities on DRAs	77
5.2	Hidra Element	81
6	Antenna arrays and the Dassault Aviation's SPECTRE software	85
6.1	Simulation of large arrays in SPECTRE	87
6.2	Conclusion and remaining issues	98
7	The particular case of a narrow bandwidth	101
7.1	A Tx Band element with directionnal coupler	101
7.2	Measurement results	107
7.3	Simplification of the element - 2x2 subarray	110
7.4	Some words about the Ka-Band	116
8	Numerical study of a graphene-based variable capacitor	119
8.1	A simplified theory of a quantum capacitor	120
8.2	The Green's Functions of a point charge	124
8.3	Global structure of a code implementing the Method of Moments	130
8.4	Validation of the code with benchmarks	133
8.5	Simulation of a graphene capacitance	138
8.6	Final example and conclusion	140
9	Conclusion and perspectives	141
A	Appendix 1 : Microwave connectors.	143
B	Appendix 2 : Green's function.	147
	Bibliography	149
	Curriculum Vitae	157

List of Figures

1.1	Dassault Aviation's Falcon aircraft.	2
1.2	Illustration of the polarization tracking principle - how to decompose a linear polarization -green- into the sum of two circular ones -red, LHCP and RHCP- (Courtesy of Dassault Aviation).	3
1.3	Schematic side view of the antenna (Courtesy of Dassault Aviation).	3
1.4	Perspective view of the antenna (Courtesy of Dassault Aviation).	4
1.5	Frequency Bands potentially involved in SATCOM links.	4
1.6	Perspective view of a printed radiating element in Ku-Band with a single patch - taken from [1].	7
2.1	Series feeding vs corporate feeding - beam steering and beam squinting.	10
2.2	Beam squinting effect quantified with Matlab for the different bands of interest.	12
2.3	Comparison between a usual series feeding and a metamaterial based series feeding for beam squinting reduction. Courtesy of [2].	14
2.4	A vertical corporate distribution system elementary block : the T-junction.	15
2.5	Simulation results for the T-junction.	17
2.6	Schematic view of a beam steering; each "element" here would be a line of elements in our array.	20
2.7	Originally proposed solutions for a mechanical phase shifter / delay between radiating lines (in french).	22
2.8	A variable TTD system using chirped delay lines.	23
2.9	A typical microstrip Rotman lens in Ku-Band, with 43 inputs (on the left) and 16 outputs (right); courtesy of [3].	25
2.10	Photo of a Distributed MEMS Delay Line (DMTL) usable as a variable delay in phased arrays. Courtesy of [4].	26
2.11	A purely mechanical system for beam-steering. SIW design in Ka-Band, around 24GHz.	28
3.1	Illustration of an elliptically polarized electromagnetic wave. Courtesy of [1].	31
3.2	Basic printed planar antennas and their most classical feedings. Courtesy of [1].	34
3.3	Top view of a stacked patch antenna excited through a cross-shaped aperture by two orthogonal microstrip lines.	37
3.4	HFSS model of the stacked patch antennas.	41

List of Figures

3.5	A survey of various existing directional couplers.	43
3.6	The recent evolution of aperture-coupled directional couplers. Courtesy of [5], [6] and [7]	44
3.7	S parameters and phase shift for an UWB elliptically-shaped directional coupler. Courtesy of [7].	45
3.8	Model, simulations and prototyping of the proposed stripline version of the coupler.	46
3.9	Measurements of the coupler prototype (post-processed in Matlab).	48
3.10	HFSS model and simulation results for a complete antenna element.	50
4.1	Two illustrations of the sequential rotation principle (courtesy of [8] and [1]).	54
4.2	Sequentially-fed cavity around 300MHz (early 1970s). Courtesy of [9].	56
4.3	Example of a sequentially-fed patch using Schiffman phase shifters (2000s). Courtesy of [10].	56
4.4	Recent works that inspired the new antenna (courtesy of [11] [12]).	57
4.5	Layer view and Top view of the proposed structure.	59
4.6	Results for the sequentially-fed stacked patches.	61
4.7	A non-exhaustive list of existing phase shifters.	63
4.8	Description of a microstrip phase shifter made up of only elementary matching sections and stubs (courtesy of [13]).	64
4.9	Simulation of the retained 180° phase shifter.	65
4.10	Feeding system using Wilkinson splitters.	67
4.11	Simulation of the proposed antenna element (CST).	70
4.12	Simulated Axial Ratio results for $\phi = 0$ (CST).	71
4.13	Photo of the PCB layers for the prototype and measurement setup in anechoic chamber.	72
4.14	Measured S parameters and Axial Ratio results for $\phi = 0^\circ$	74
4.15	Prototype photos and measured Radiation Pattern for $\phi = 0^\circ$	75
5.1	Generalities about DRAs - Some exotic shapes.	78
5.2	Building DRA arrays with the perforation method - Array examples.	80
5.3	Sequentially-fed DRA	82
5.4	DRA simulation results.	83
6.1	Illustration of the Dassault Aviation toolchain : parameterization of an ideal DRA in SPMB before the SPECTRE simulation.	88
6.2	Perspective view of a 2x2 array of DRA in Catia.	89
6.3	Spectre simulation of an isolated DRA with ideal excitations.	90
6.4	Spectre simulation of an isolated sequentially-fed stacked patches antenna with ideal excitations.	91
6.5	Beam steering for a 2x2 Array of DRA : post-processing of the SPECTRE results in Matlab (90° corresponds to the broadside direction).	93
6.6	Beam steering with an 8x8 array in the $\phi = 0^\circ$ plane.	95

6.7	Simulation of an 8x8 array of planar antenna elements : setting up the factorization method of SPECTRE.	96
6.8	Beam steering for a 8x8 array of DRA : post-processing of the SPECTRE results in Matlab (90° corresponds to the broadside direction).	97
7.1	Tx-band antenna inside a cavity.	102
7.2	Tx-band antenna with hybrid coupler.	105
7.3	Photo of the Tx-Band antenna with hybrid coupler - Measured S parameters.	108
7.4	Measurement results for the Tx-Band antenna with hybrid coupler (both polarizations and principle planes).	109
7.5	Description of the simplified element and of a 2x2 subarray surrounded by dummy patches.	111
7.6	Simulated results for a 2x2 subarray surrounded by dummy patches (beam steering in the plane $\Phi = 0$).	112
7.7	Simulation results around 20GHz.	117
8.1	Interdigitated capacitors and the introduction of graphene in this technology.	121
8.2	Case of a point charge in vacuum - description and parameters.	125
8.3	A 2D Fourier Transform with azimuthal symmetry, also called "Hankel Transform".	126
8.4	A point charge and three 2D-infinite dielectric layers; parameterization of the problem.	128
8.5	General structure of the Matlab code. In red : main file; in yellow : subroutines and arrows indicating the execution flow; in green : files only called during the preparation / debugging process.	131
8.6	Illustration of Image Theory for a point charge near dielectric interfaces. The first case is a classical single-interface problem, the second case was solved more recently and consists of a dielectric slab in vacuum (double-interface).	135
8.7	Benchmarks for the Green's Function computation - Comparison between our code (in blue) and some particular closed-form results using image theory (in red). See table 8.1 for a description of each test performed.	136
8.8	Benchmark plots (end).	137
8.9	Simulations on nanometric structures using our MoM code.	139
8.10	Evolution of the complete capacitance vs quantum capacitance.	140
A.1	Rosenberger connector dimensions extracted from the datasheet (SMA JACK PCB 32K243-40ML5).	144
A.2	Rosenberger connectors studied with HFSS.	145

List of Tables

1.1	Main requirements for the high gain phased array antenna.	5
1.2	Main requirements for the NATALIA project (array and radiating elements). . .	7
2.1	The beam squinting effect in different frequency bands : some data.	12
2.2	Optimal dimensions for a vertical T-junction.	16
4.1	Best values found for the ideal sequentially-fed antenna.	60
4.2	Phase shifter dimension values.	66
4.3	Dimensions for the antenna element and its feeding system.	70
7.1	Best values found for the ideal sequentially-fed Tx-band antenna.	104
7.2	Dimensions for the 2x2 subarray in Tx-Band.	113
7.3	Dimensions for an element around 20GHz.	116
8.1	Parameters and dimensions used for the Matlab benchmarks (comparing our code with image theory results).	135
A.1	Geometrical parameters for an optimized Rosenberger connector footprint. . .	146

List of Acronyms

AR Axial Ratio

Co-pol Copolarization

Xpol Cross Polarization

CP Circular Polarization

LP Linear Polarization

RHCP Right Hand Circular Polarization

LHCP Left Hand Circular Polarization

DBS Direct Broadcasting Satellite

UWB Ultra Wide Band

EPFL Ecole Polytechnique Fédérale de Lausanne

LEMA Laboratoire d'ElectroMagnétisme et d'Antennes

HFSS High Frequency Structural Simulator

CST Computer Simulation Technology

FBR Front-to-Back Ratio

HPBW Half-Power Beam-Width

NATALIA New Automotive Tracking Antenna for Low-cost Innovative Applications

PCB Printed Circuit Board

PPWM Parallel Plate Waveguide Mode

S3FIP Shielded Strip Slot Foam Inverted Patch

SSFIP Strip Slot Foam Inverted Patch

TRL Thru-Reflect-Line

TTD True Time Delay

VCO Voltage Controlled Oscillator

NDL Nonlinear Delay Line

SIW Substrate Integrated Waveguide

List of Tables

DRA Dielectric Resonator Antenna

MoM Method of Moments

GF Green's function

FEM Finite Elements Method

FDTD Finite Differences Time Domain

QC Quantum Capacitance

1 Introduction

Have patience. All things are difficult before they become easy.

Saadi

1.1 Main targets of the thesis

Internet access in aircrafts is only possible through a satellite communication link, or SATCOM. Nowadays, the service available for business-class aircrafts goes through the Inmarsat network. The bitrate is nonetheless limited to around 150-200 kbps, because this network operates in L Band (around 1.5GHz) and uses an outdated IP protocol for Data transfer. In order to increase the bitrate of a factor of 10 or more, it is necessary to increase the frequencies involved in the transmission. In this way, the same frequency bandwidth in percentage will correspond to a much larger absolute bandwidth.

The X-Band (8GHz to 12GHz) and the Ku-Band (12GHz to 18GHz) can allow this improvement compared to the L-Band. Moreover, going to the K-Band (18GHz to 27GHz) or to the Ka-Band (27GHz to 40GHz) would even bring an additional improvement. Currently, Viasat provides a high rate service in Ku-Band (uplink from 128kBps to 256kBps, downlink from 2.25MBps to 4MBps) but the exploitation cost remains too high; in particular, the parabolic antenna proposed by Viasat is difficult to install on an aircraft because they are cumbersome and unadapted to aerodynamical constraints (source : private Dassault Aviation / LEMA-EPFL contract).

Consequently, the use of high gain antennas for SATCOM services implies the development of novel integration methods. The purpose of this thesis is to progress in the design of high gain antennas that could be used in the middle or long term for these high rate SATCOM links, while having a small volume and keeping a low profile (ideally they should be flush mounted in the fuselage). These antennas typically include two main parts in the electromagnetic RF

Chapter 1. Introduction

layer : an array of radiating elements, and a beam steering system made up of phase shifters and attenuators of some kind.



Figure 1.1: Dassault Aviation's Falcon aircraft.

The thesis will keep the focus on the first RF part. The target is to address the design of an array of radiating elements in Ku-Band, which is split in two subbands. The reception band (Rx) ranges from 10.7GHz to 12.75GHz, while the transmission band Tx ranges from 14GHz to 14.5GHz. A quite stringent constraint about these elements is that they will have to support a dual-circular polarization, while keeping an Axial Ratio below 3dB for a wide range of angles -namely from broadside to 60° or ideally 70° - in order to be able to keep track of satellites wherever the aircraft is travelling.

Also, a quite high gain of 33dB is ideally expected, together with a very tight steering precision of around 0.5° . It will indeed be necessary for the terminal to be able to discriminate between geostationary stationary that lie 2° - 3° away from each other on their orbit. According to the official specifications, the amount of elements in the array has to reach around a thousand to satisfy this requirement. We can start with a basis of 32×32 elements -namely 1024 of them- in order to keep it as a power of two, as it will simplify the design of the distribution system. All this will be studied in detail in later chapters.

The requirement of dual-circular polarization is quite classical in phased arrays; it stems from the fact that SATCOM links, at least in Ku-Band, use two orthogonal linear polarizations named *Horizontal (H)* and *Vertical (V)* in order to carry two channels at the same frequency. In order to keep track of the desired channel, an important and simple result is used, namely the fact that each linear polarization can be decomposed in the sum of a *Right Hand* and a *Left Hand* Circular Polarizations, abbreviated respectively as RHCP and LHCP (See Fig. 1.2). The electronics dedicated to the polarization tracking is out of the scope of this thesis.

When Dassault Aviation came with the idea of this thesis, the intended goal was to provide on the middle term a SATCOM antenna for their civil aircraft, the Falcon (Fig. 1.1). They had an idea of what the final antenna should look like, and especially they provided a rather original

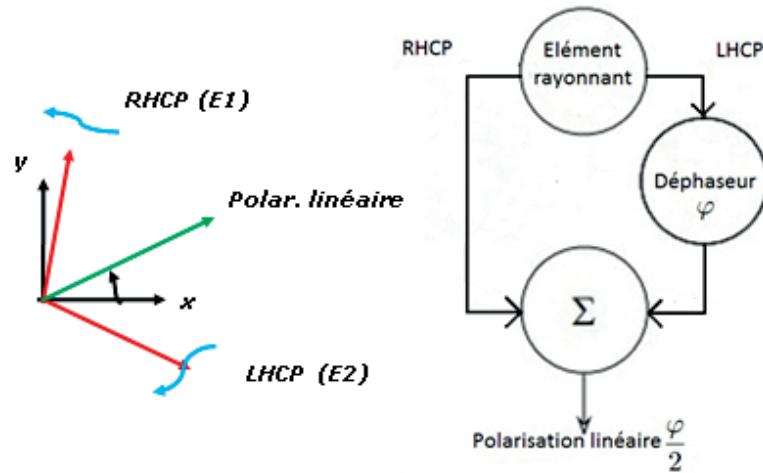


Figure 1.2: Illustration of the polarization tracking principle - how to decompose a linear polarization -green- into the sum of two circular ones -red, LHCP and RHCP- (Courtesy of Dassault Aviation).

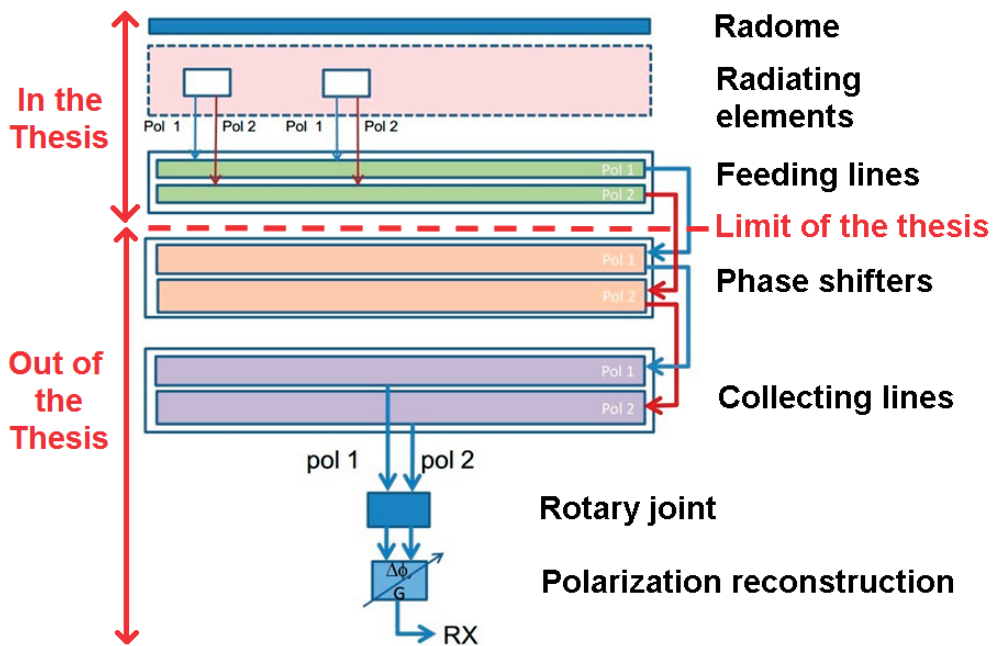


Figure 1.3: Schematic side view of the antenna (Courtesy of Dassault Aviation).

perspective on the way the beam steering should be produced. A schematic side view of the desired antenna is provided in Fig. 1.3, and a perspective view is visible in Fig. 1.4.

The main issue to address is that usually commercial phased arrays make extensive use of specific chips that contain phase shifters, Low Noise Amplifiers (LNA) and sometimes even circuits for polarization treatment. This kind of chips is not immediately available for purchase -except for LNA- and it is often required to design a custom chip for such a project, usually

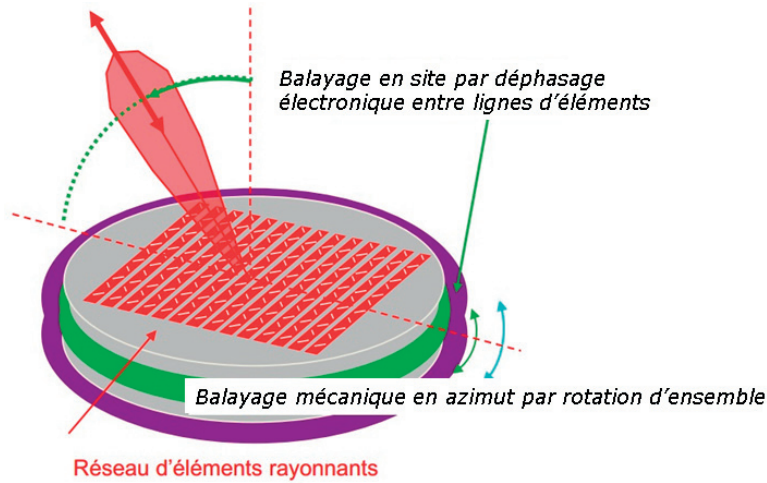


Figure 1.4: Perspective view of the antenna (Courtesy of Dassault Aviation).

with the help of a partner company. This can be costly, and because these antennas are not expected to be produced at a massive scale, Dassault Aviation looking for an alternative way to produce the beam steering.

The guiding idea will be to consider the array as a set of parallel lines of radiating elements; all the elements of a line have to be fed in phase, while a variable phase shift has to be applied between consecutive lines. In this way, a beam steering in elevation is performed; on the other hand, the azimuthal beam steering is simply performed by a mechanical rotation. The main question is : how do we apply a phase shift between lines ? Dassault Aviation's suggestion is to use some kind of mechanical system, involving for example coaxial lines of variable length (visible in Fig. 1.4). This idea will be discussed and criticized in the first chapter.

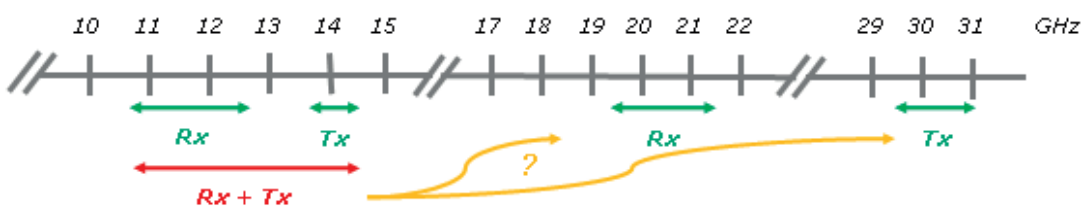


Figure 1.5: Frequency Bands potentially involved in SATCOM links.

Coming back to the frequency bands, the priority in this project was given to the Rx-Band upon Dassault Aviation's suggestion. Tx-Band can be included afterwards in the study. Two approaches are then possible : either a dual-band or wideband array is designed in order to include them, or two separate arrays are considered. The second solution simplifies for sure the design tasks a lot, due to the fact that the frequency bandwidth required by each array is reduced. Additionnaly the electronics and the mechanical systems dedicated to the beam steering, the amplification or the polarization treatment will be clearly separated for reception

Table 1.1: Main requirements for the high gain phased array antenna.

Name	Ideal Value
Gain	33dB
Half Power Beam Width (HPBW) angle	3°
Elevation angle covering	0° to 60° / 70°
Side Lobe Level (SLL)	< -13dB
Steering precision	< 0.5°
Overall efficiency	> 75%
Axial Ratio	< 3dB
Polarization	Dual Circular
Directivity (element)	(5-7dB)
Radiation Pattern (element)	Azimuthal symmetry, monotonous
Port Isolation	> 20dB
Mutual coupling with neighbors	< 20dB
Return Loss	< 20dB
Maximal antenna thickness	90mm

and transmission. This solution will thus be preferred, unfortunately at the expense of the overall size.

Another aspect is the growing interest for K/Ka-Band services. Industry and research in general are more and more looking towards these higher frequencies. Although strictly speaking it is not in the scope of the thesis, the potential transposition of the radiating elements from Ku-Band to K/Ka-Band will be discussed at the end of the thesis (See Fig. 1.5). For SATCOM links, the Rx-Band ranges from 19.7GHz to 21.2GHz, while the Tx-Band ranges from 29.5GHz to 31GHz.

It is likely that Dassault Aviation could make use of the K/Ka-Band instead of the Ku-Band on the long term for civil applications. A appreciable property of K/Ka-Band communication terminals is that they do not use two circular polarizations at the same time for polarization tracking : they only need to be able to switch between RHCP and LHCP, which for sure simplifies the whole electronics. Moreover, the relative bandwidths required in K/Ka-Band are smaller than the ones required for the same service in Ku-Band (especially for the Rx-Band in fact), which potentially brings a serious simplification in the design. Yet the main drawback of increasing frequency is obviously that the antenna manufacturing process can become more sensitive to any kind of tolerances.

1.2 A previous project as a starting point : NATALIA

The first step while dealing with a research project of this extent is to search for a previous project that could become a starting point, a reference or a source of inspiration. In our case, the NATALIA Project -which stands for *New Automotive Tracking Antenna for Low-cost Innovative Applications*- turned out to be the best fitted for this purpose. This topic was developed in a previous thesis defended in 2011 at LEMA by Roberto Torres Sanchez [1], in coordination with the JAST company (now bought by Viasat).

The main purpose of this thesis was to design a phased array antenna for the Reception of Direct Broadcasting Satellite (DBS) services. These services mainly cover safety, telemetry & control, tolling, real-time driver information and entertainment. The frequency band covered is exactly matching our requirement, and ranges indeed from 10.7GHz to 12.75GHz. Table 1.2 makes a list of the constraints that the NATALIA antenna had to respect; it can be used for a comparison purpose with 1.1.

Some of the specifications are sensitively the same in both cases, but there are also notable differences; they provide additional challenges for this thesis, and even beyond for the Dassault Aviation/SATCOM project in general :

- There were no investigations in the NATALIA project in any frequency band except in the 10.7GHz-12.75GHz range.
- The feeding part was mainly designed by JAST, using custom chips for controlling the beam steering.
- The expected final gain is around 20dB, which is much below our constraints. The HPBW is accordingly higher, and although not specified, one can assume that the steering precision will be of several degrees.

The NATALIA radiating element is a printed antenna, also known as microstrip patch antenna and visible in Fig. 1.6; in a nutshell, it consists of two stacked patches, excited by a stripline through an aperture in the ground plane. The presence of two patches allows to extend the bandwidth by merging their respective resonances. The use of foam as a substrate is a classical method to improve the bandwidth of such antennas, due to the fact that the permittivity of foam is very close to the one of air. These structures, named SSFIP antennas (Strip Slot Foam Inverted Planar antennas) were first explored by J. F. Zurcher in the late 1980s [14] and described a few years later in a dedicated book [15].

In general, stacked aperture coupled patch antennas are appreciated for their low profile and their ease of fabrication with usual PCB techniques; but also for their natural ability to be included as elementary radiating cells in phased arrays, supporting dual circular polarization if necessary. On top of this, they can still operate on a relatively wide bandwidth (15%-20%

1.2. A previous project as a starting point : NATALIA

typically). We will come back on this technology in more detail in chapter 3, when the NATALIA element will be progressively adapted and improved for our needs.

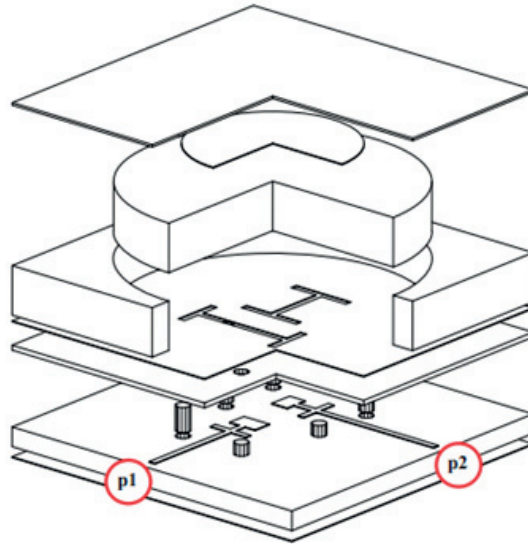


Figure 1.6: Perspective view of a printed radiating element in Ku-Band with a single patch - taken from [1].

Table 1.2: Main requirements for the NATALIA project (array and radiating elements).

Name	Ideal Value
Gain	20dB
Half Power Beam Width (HPBW) angle	< 9° in azimuth, < 18° in elevation
Elevation angle covering	0° to 60°/70°
Side Lobe Level (SLL)	< -13dB
Steering precision	< unspecified
Overall efficiency	> 80%
Axial Ratio	< 3dB
Polarization	Dual Circular
Directivity (element)	(5-7dB)
Radiation Pattern (element)	Azimuthal symmetry, monotonous
Port Isolation	> 20dB
Mutual coupling with neighbors	< 20dB
Return Loss	< 20dB
Maximal antenna thickness	10mm

1.3 Thesis organisation and original contributions

In this section, we provide a small outline of the global organization of the chapters; the original contributions of this thesis are mentioned in bold.

Chapter 2 : Chapter 2 discusses the global architecture of the array and aims at presenting everything that is related to the feeding system and the beam steering. It contains in particular a bibliographic study of existing beam steering systems.

Chapter 3 : Starts the design of printed antennas in Ku-Band, with simple examples that turned out not to be efficient enough. Potential directional couplers for dual-circular polarization are studied as well. **A wideband directional coupler was selected, rescaled and adapted to our specific context, resulting in a conference paper in Dubrovnik ICECOM conference, 2013.**

Chapter 4 : This chapter explores the possibility to improve the polarization quality of elements by using feeding schemes with improved symmetry (sequential rotation). **A more robust Rx-Band element with a novel feeding topology was designed. A paper was submitted to the LAPC conference, Loughborough, 2014.**

Chapter 5 : Dielectric Resonator Antennas (DRA) have been considered at some point during the thesis as outsider element candidates, and all the bibliography and research linked to them is described here. **A Rectangular DRA with improved dual-circular polarization was designed and presented during the Lisbon Eucap conference, 2015.**

Chapter 6 : Subarrays of elements are simulated in order to study their radiation pattern, but also the effect of mutual coupling. The 2015 internship in Dassault Aviation (St-Cloud, France) and the use of their proprietary SPECTRE Software is described here.

Chapter 7 : The novel element developed for the Rx-Band is adapted to the Tx-Band. Because the bandwidth is much smaller in that case, it is proven that more efforts can be successfully deployed to decrease the coupling between neighboring elements, by embedding the patches in a metallic cavity. **In the end, a 2x2 array of elements is designed, involving an additional sequential rotation for an improved polarization quality.** The possible rescale of this antenna in Ka-Band is also briefly discussed.

Chapter 8 : In this last chapter, a different topic is covered. Variable Quantum Capacitors involving the recent Graphene technology are briefly described. The study of these components is motivated by the fact that they are likely to be applied to phased arrays in the future. **A software was developed to help the simulation of these capacitors, involving infinite 2D Green's functions for multi-layered systems at nanoscale.**

2 Global architecture of the array

It always takes longer than you expect,
even when you take into account
Hofstadter's Law.

Hofstadter's Law

2.1 Series feeding : The beam squinting effect and its consequences

As was explained in the previous chapter, the array developed in this thesis is seen as a set of parallel lines of elements. Each line is a subarray, a "fundamental" constitutive piece of the overall structure, and a phase shift is applied between them in order to perform the beam steering. The practical question that comes next is to know how exactly the signal is going to be distributed among the elements. Essentially, there exist two alternatives, namely the series feeding and the corporate feeding [16]. With the latter, the signal is split recursively over several stages, leading to a kind of "tree-shaped" topology. With the former, a single distribution line is feeding the radiating elements, and the signal is splitted periodically all along the line (illustrated in Fig. 2.1a).

The corporate feeding is preferred in practice for most arrays. This structure is more cumbersome than its series counterpart, but it is highly symmetrical by essence, and in particular all the elements are fed in phase at all frequencies. In the most classical approach, a square-shaped array is thus excited with a corporate network, and electronic chips are set at element level for implementing amplification, phase shifts, delays and maybe some more exotic functionalities related to polarization, as can be seen in Fig. 2.1b.

Yet in our situation, it seems clear that a series-feeding would suit much more the philosophy of the work, since lines are supposed to be the basic blocks of the whole construction. The main advantage of series feeding is that it turns out to be the most compact approach that can be imagined, while it looks difficult to fit a corporate network for each single line. Moreover,

Chapter 2. Global architecture of the array

one can expect the losses to be lower with series feeding than with corporate feeding.

Unfortunately, two drawbacks appear quite quickly; first, it is necessary to separate the signal in such a way that each of the elements gets an equal power, which requires unbalanced splitters with very different -and sometimes extreme- ratios between their outputs. The corporate feeding on the other hand, only requires the same symmetric splitters, at least if the amount of elements is a power of two. The now classical work of Young and Cristal [17] could bring a solution with coupled line directional couplers, but one should not underestimate this practical difficulty. It is also necessary to mention that the small reflections that occur along the line will quickly degrade the overall quality by creating undesired standing waves, especially when the line gets very long.

The second issue is even more fundamental, and is called the *beam squinting effect*, roughly translated in french as "strabisme de faisceau" and described for example in [18]. The situation is depicted in Fig. 2.1a; each of the consecutive elements is separated from its neighbors with a piece of line that induces a non-zero phase shift ϕ . This phase depends on the frequency, as will be shown below. If the line length is chosen in such a way that this phase shift is 2π at central frequency, the elements are all in phase and the radiation is broadside as expected. But whenever the frequency changes, a phase shift of $\Delta\phi$, $2\Delta\phi$, $3\Delta\phi$... is virtually applied to the elements, and the beam starts to tilt accordingly.

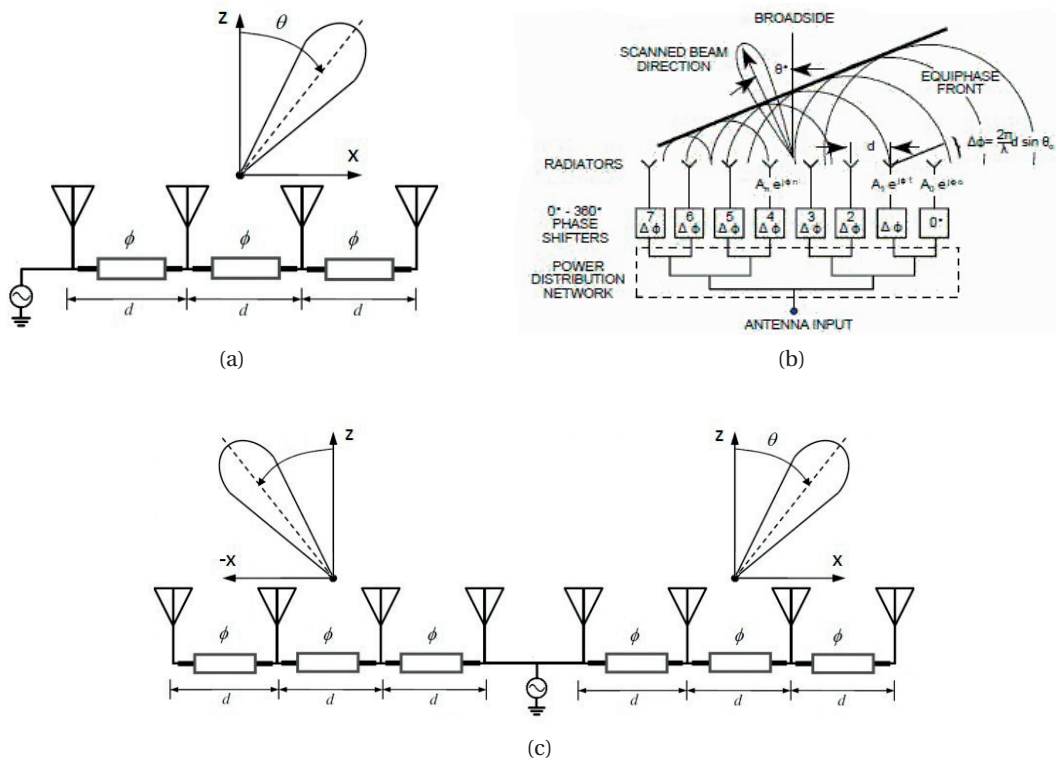


Figure 2.1: Series feeding vs corporate feeding - beam steering and beam squinting.

2.1. Series feeding : The beam squinting effect and its consequences

Let's make this idea more accurate with some equations. From now on, the subscript "0" will be associated with the central value of the frequency band. The speed of a wave, its frequency and its wavelength are linked by the well-known proportionality relation $f\lambda = v$. From this we can deduce an equation that will be our starting point:

$$f_0\lambda_0 = f\lambda \rightarrow \lambda = \frac{f_0\lambda_0}{f} \quad (2.1)$$

If the distance between consecutive elements is chosen so that the phase shift at central frequency is 2π , then the phase shift ϕ at any frequency can be deduced by proportionality. The phase discrepancy $\Delta\phi = \phi - \phi_0$ follows :

$$\phi = \frac{2\pi f_0}{f} \rightarrow \Delta\phi = 2\pi \frac{f_0 - f}{f} \quad (2.2)$$

And according to the theory of linear arrays, this phase shift is linked to the tilt angle, the wave number in vacuum and the distance between radiating elements by :

$$k = \frac{2\pi}{\lambda} = \frac{2\pi f}{c} \rightarrow kd \sin(\theta) = \Delta\phi \quad (2.3)$$

Isolating the angle, we get the fundamental relation :

$$\sin(\theta) = \frac{\lambda}{d} \frac{f_0 - f}{f} \quad (2.4)$$

It is also useful to recall that the distance between elements is constrained by both the maximal frequency of operation and the maximal steering angle, as was explained in the previous section :

$$d = \frac{\lambda_{min}}{1 + \sin(\theta_{max})} \quad (2.5)$$

With all those elements, a Matlab script was implemented to assess the impact of this effect for all the bands that we may be interested in. This includes of course the Rx/Tx bands in Ku-band alone, but also the larger merged band Rx+Tx.

Chapter 2. Global architecture of the array

Table 2.1: The beam squinting effect in different frequency bands : some data.

Name	f_min (GHz)	f_0 (GHz)	f_max (GHz)	d (mm)	Squint (°)
Ku-Rx	10.7	11.7	12.7	12.7	11
Ku-Tx	14	14.25	14.5	11	2
Ku-Rx+Tx	10.7	12.6	14.5	11	22
Ka-Rx	19.7	20.4	21.2	8	4
Ka-Tx	29.5	30.25	31	5.5	2.2

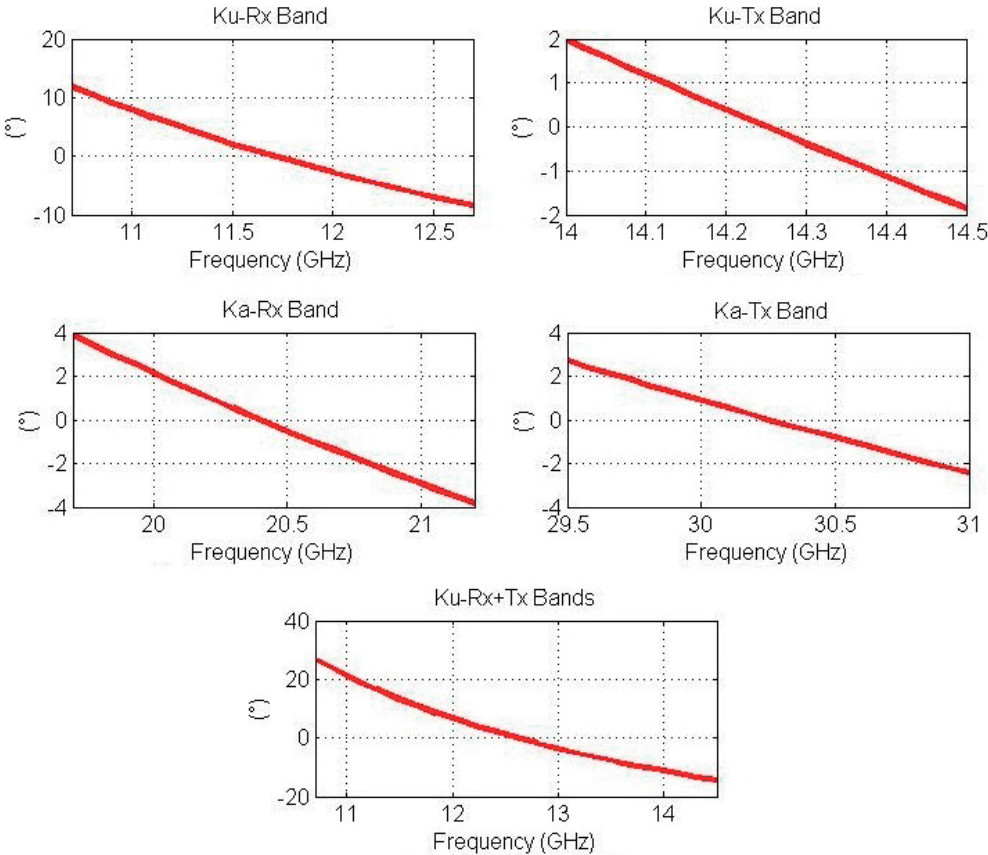


Figure 2.2: Beam squinting effect quantified with Matlab for the different bands of interest.

2.1. Series feeding : The beam squinting effect and its consequences

The phase shift curves for all those combinations are plotted in Fig. 2.2, and the key data are reported in table 2.1. A few remarks stem from the observation of these results :

- It is clear from equation 2.4 that the tilt angle does not depend on the number of elements at all, which is not immediately intuitive. Yet, the directivity obviously depends on it, and in general the squinting effect is more damaging for very directive beams that are pointing in an accurate direction.
- On the other hand and still from equation 2.4, the maximal squinting value depends on the relative bandwidth and not on any absolute value. This means that using higher frequency bands may reduce this parasitic effect.
- Because of the nonlinearity of equation 2.4, the curves for the tilt angle are not exactly linear, and a frequency f_0 slightly below the middle of each band could be a better choice for optimizing the maximal deviation.

We recall that a precision of 0.5° is expected, and we are very far from it in Ku-band. In Ka-band yet, and even in Ku-Tx band, the tilt angles remain below a few degrees. It is also worth mentioning that, if a single frequency channel is considered at a time -and not the whole frequency band- the squinting effect is automatically reduced.

The next step in this discussion is naturally to criticize very briefly some solutions to mitigate the beam-squinting effect. A first idea is to follow the pattern presented in Fig. 2.1c : if a line of elements is fed in its middle point, both half-lines exhibit beam-squints in opposite directions. One could think that they would "compensate" somehow; unfortunately the practical effect is just to spread the beam, and even to split it progressively in two distinct and divergent beams as the frequency increases. We can thus reject this method.

A second approach would be to compensate the time delay between consecutive elements by adding a meandered line below each of them. In that case, the very last element would need no additional length while the first element would need a very long one (equal to the length of the whole line). Here again, it is clear that this method is impracticable; it would require so much place to fit these meanders that using a series feeding would no longer present any advantage compared to a corporate feeding.

It is worth mentioning now that there are more serious and systematic ways of mitigating the beam squinting effect developed in the recent literature. There is essentially one family of methods, which is based on metamaterials. The reader unfamiliar with this topic is sent to the famous monograph by Caloz and Itoh [19], and we are just going to discuss an example in order to point out the limits of this approach.

In Fig. 2.3, a small series-fed array of four dipole elements is excited in two different ways : first, a simple meander whose length corresponds to a phase shift of 2π at central frequency is used for the feeding. Then, it is replaced by a piece of transmission line in series with

Chapter 2. Global architecture of the array

a piece of Negative Refractive Index metamaterial. These two lines are optimized in such a way that the phase response around the central frequency will be as flat as possible in a neighborhood of 0° . This method is approximative, and the results in Fig. 2.3 show indeed a beam squinting reduction, but it remains very far from being a practical solution for us. Some other publications present similar results [20] [21], but none of them would bring a practical, conclusive and industrial solution. Consequently and from now, we are going to strongly recommend the use of a corporate distribution network instead.

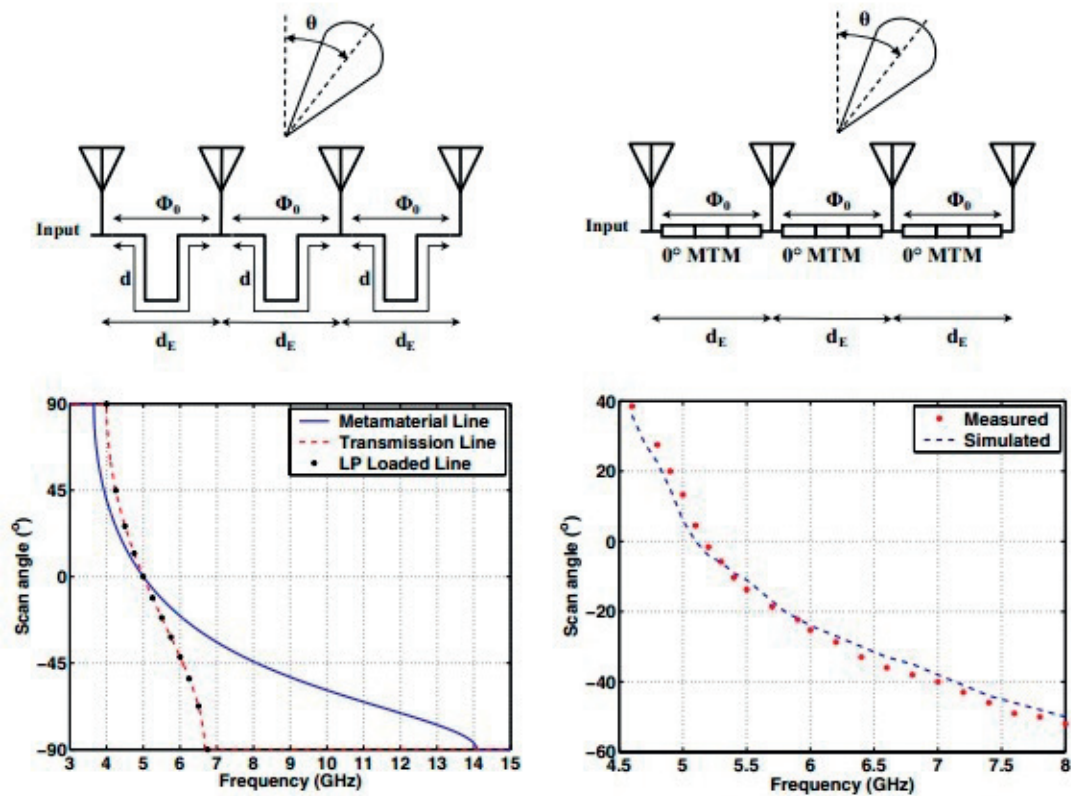


Figure 2.3: Comparison between a usual series feeding and a metamaterial based series feeding for beam squinting reduction. Courtesy of [2].

2.2 Vertical corporate feeding

At first sight, the series feeding approach looked to be the best suited for an antenna array which can be thought as a set of parallel lines of radiating elements. Yet, it appeared over the last sections that the inherent drawbacks of this method -especially the beam-squinting effect- are at the same time so damaging for the correct operation and so difficult to overcome that one had better to resort to the more classical but also more cumbersome corporate topology. Considering the necessity that we have to distribute a signal with a specific phase over each line of 32 elements, it is then necessary to be able to fit a corporate distribution system below each of them. In fact and because of the dual circular polarization requirement, even two distribution systems per line will be necessary. It is thus quite clear that a vertical construction shall be expected as a solution to these topological problems.

The solution proposed to build a vertical corporate feeding system (implicitly assuming that the number of elements is a power of two) consists in building recursively over the structure depicted in Fig. 2.4. It is a vertical T-junction between two identical asymmetric stripline feeding layers, which consist in a stack of a 0.508mm RO4003C substrate and of another 0.203mm one.

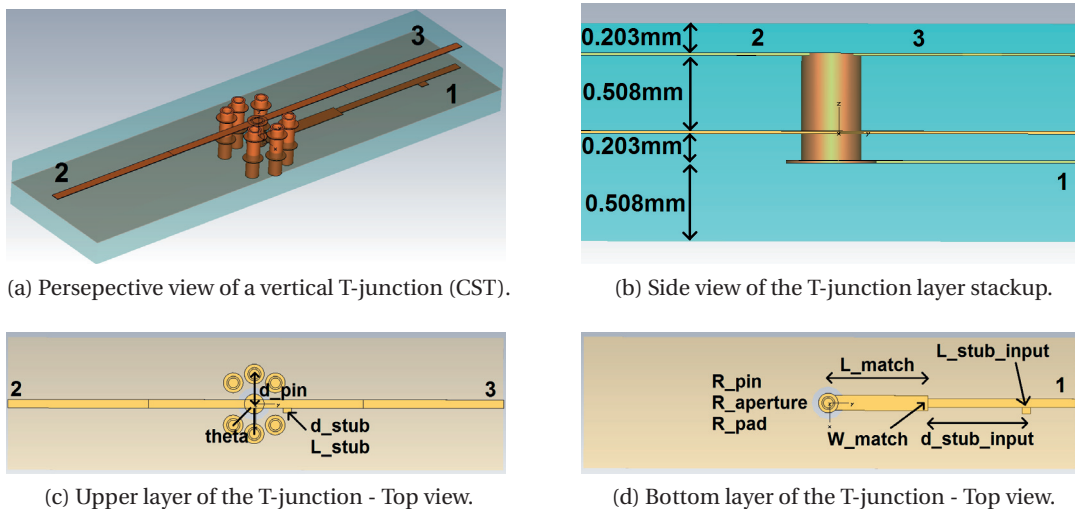


Figure 2.4: A vertical corporate distribution system elementary block : the T-junction.

It is necessary to stop here on the choice of the substrate, because RO4003C will remain the preferred substrate for prototypes all over this thesis and it is somewhat motivated by practical reasons. Firstly, its thickness needs to be thin enough to ensure that the final structure would remain as flat as possible; for 32 elements, five of these stages are required, which would maintain the overall thickness below 4mm. Secondly, this substrate is particularly suited for designs involving metallized holes. Some other Rogers substrates -in fact, all those containing PTFE- require a specific chemical treatment between the drilling and the metallizing operation, in order to get rid of some very small particles of glass created by the local overheating. Since

Chapter 2. Global architecture of the array

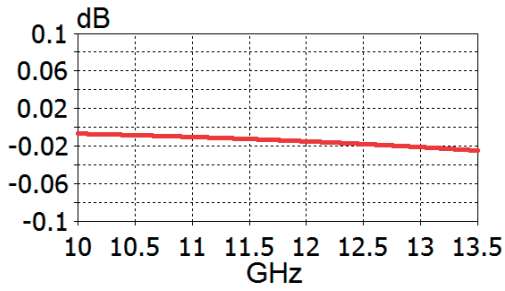
this process is not available at EPFL, it is fortunate that the Ceramic-based RO4003C is totally immune to this effect. Finally, the availability and low cost of RO4003C justifies its extensive use for research prototypes.

Table 2.2: Optimal dimensions for a vertical T-junction.

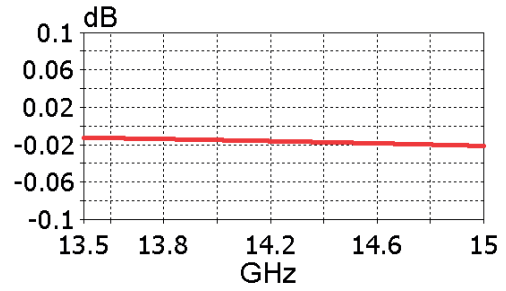
Parameter	Rx value	Tx value	unit
d_pin	0.2	0.2	mm
d_stub	1.05	0.95	mm
d_stub_2	3.2	3	mm
L_stub	0.1	0.15	mm
L_stub_2	0.15	0.2	mm
d_pin	0.2	0.2	mm
L_match	3.8	3	mm
angle	45	45	(°)
R_aperture	0.5	0.5	mm
R_pad	0.1	0.1	mm
W_adapter	0.45	0.45	mm
W_feed	0.26	0.26	mm

The transition between the two layers is performed by a via passing through an aperture in the ground plane; this via is surrounded by a "belt" of six other vias that can be seen clearly in both top views 2.4c and 2.4d. In this way the signal is confined on its vertical travel as it would be in a coaxial cable. In the upper layer, it is split in two outputs whose impedance are set to be 100Ω . This impedance also corresponds to the input impedance of the structure, in order to allow a recursive use of the T-junction.

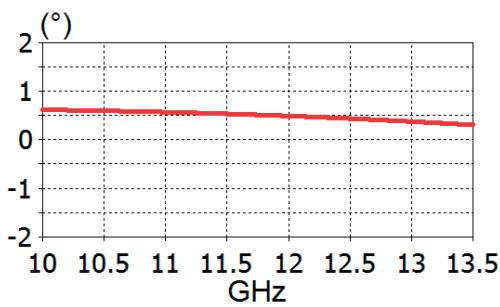
In order to adapt the impedance from the coaxial part (around 50Ω in principle), a classical quarter-wavelength adapter is employed; a small stub is also placed before the matching line, as a secondary fine-tuning element for the impedance matching (Fig. 2.4d). It appears then that almost all the circuit has been described so far, except a small detail that stems from the following remark : the overall circuit is not completely symmetric, because the input signal is not perpendicular to the T-junction. Even if this dissymmetry seems very slight, it turned out to yield some imbalance between the outputs in terms of both amplitude and phase. Fortunately, it was found with a purely empirical approach that these effects could be compensated thanks to a small stub placed at one of the outputs (Fig. 2.4c).



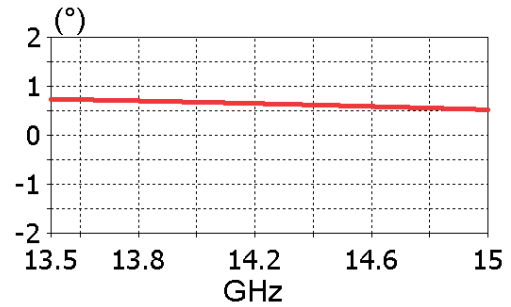
(a) Imbalance between T-junction outputs (Rx-band).



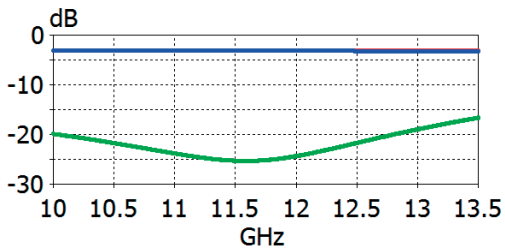
(b) Imbalance between T-junction outputs (Tx-band).



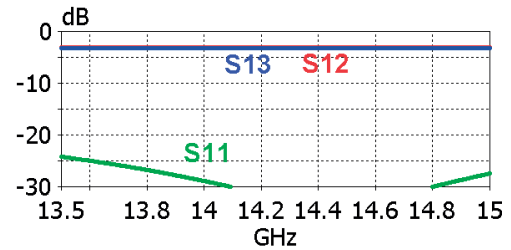
(c) Phase shift between T-junction outputs (Rx-band).



(d) Phase shift between T-junction outputs (Tx-band).



(e) S parameters for the T-junction (Rx-band).



(f) S parameters for the T-junction (Tx-band).

Figure 2.5: Simulation results for the T-junction.

Chapter 2. Global architecture of the array

The optimization process for the geometrical parameters defined in Fig. 2.4 was performed for both the Rx-band and the Tx-band, because no solution was found to be satisfying for both at the same time; the results are presented in table 2.2, and the design steps were the following :

- Some parameters were fixed from the beginning, such as the pin diameters, the input/output line widths, and the stub widths (identical to the previous one).
- A massive parameter sweep was then performed on most dimensions in order to achieve the matching. The starting values for the quarter-wavelength adapter were first set to their theoretical values.
- The output stub was optimized finally in order to obtain a balanced output.

The simulation results are shown in Fig. 2.5 for both bands, and it appears that :

- The phase imbalance is always below a degree.
- The amplitude imbalance is maintained much below 0.1dB.
- The return loss is kept below -20dB with a comfortable margin.

2.3 The beam steering system

2.3.1 A first solution using mechanical delay lines

We start by recalling that the beam steering operation in our perspective is supposed to take place in two times. First, a purely mechanical rotation is performed in order to reach the azimuthal angle that is targetted. Then, a *phase shift*, or a *delay*, has to be applied linearly between the constitutive parallel lines of the array in order to perform a proper elevation scanning. Here, we are temporarily making a confusion between *phase shift* and *delay*, two ideas that were opposed when the series feeding was being discussed previously. We saw that a misinterpretation of these notions could have a dangerous consequence, namely the occurrence of the *beam-squinting* effect. And here again the beam-squinting effect is going to appear in a slightly different way.

While the concept of phase shift for a sinusoidal signal is well-known, the concept of delay needs to be clarified. Let's assume that we have a piece of coaxial cable of length L , with a TEM mode propagating at the speed of light in vacuum -namely c -. Then the *time delay* for this signal to flow through this piece of line is given by :

$$\Delta T = \frac{L}{c}$$

The phase shift corresponding to this piece of line, or delay, is then for a frequency f :

$$f\lambda = c \rightarrow \Delta\Phi = 2\pi \frac{L}{\lambda} = 2\pi \frac{fL}{c}$$

Which means that a delay corresponds to a linearly increasing phase shift with respect to frequency. Very often in antenna engineering, a device implementing such a delay is referred to as a (*variable*) *True Time Delay*, or TTD. But then one may ask : shall we apply a delay or a phase shift between consecutive lines in order to perform a proper beam steering ? If the array considered is operating at a single frequency -as is the case for academic exercises given to undergraduate students- only phase shifts are considered and the question does not make sense. But whenever a larger frequency band is covered, it becomes increasingly important to make the difference.

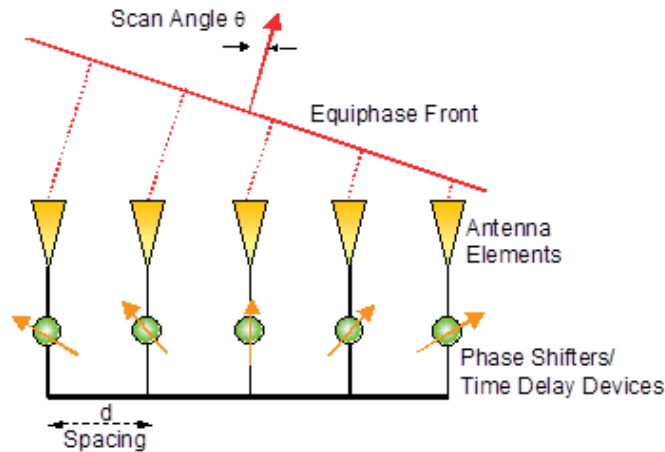


Figure 2.6: Schematic view of a beam steering; each "element" here would be a line of elements in our array.

In order to solve this problem with engineering intuition, let's consider the situation depicted in Fig. 2.6. In order to obtain a constructive interference -and thus to steer the beam towards a certain angle θ - the radiation from each line must be in phase on the wavefront for each frequency. The difference of distance that the wave travels between neighboring lines is $d \sin(\theta)$, which corresponds by definition to a delay and not to a phase shift. Consequently, one needs to "compensate" these delays by implementing variable TTD between lines to build a wavefront pointing in the required direction; if a phase shift is applied instead, the beam-squinting effect described previously will appear again and potentially deviate the pointing direction of several degrees.

Once these concepts have been clarified, it is necessary to quantify the TTD that should be achievable. For a broadside radiation, the TDD between lines is obviously zero. The other extreme case, corresponds to a steering angle of 60° ; we will consider a distance of 12.7mm between elements (Rx band) and 32 parallel lines, and we consider the TTD between what would be the rightmost and the leftmost lines in Fig. 2.6 :

$$31 \cdot 12.7 \cdot \sin(60^\circ) = 341 \text{ mm} \rightarrow \Delta t = 1.137 \text{ ns}$$

There is an additional information that is required, which is the precision, or tolerances, on this delay. Unsurprisingly, it is directly related to the steering precision, which was previously defined to be 0.5° . If we need to be able to distinguish an angle of 59.5° from an angle of 60° , the maximal discrepancy allowed between two consecutive lines is given by :

$$12.7 \text{ mm} \cdot (\sin(60^\circ) - \sin(59.5^\circ)) = 55.8 \mu\text{m} \rightarrow \delta t = 0.18 \text{ ps}$$

The first striking fact about these figures is how tight they are : one should be able to achieve

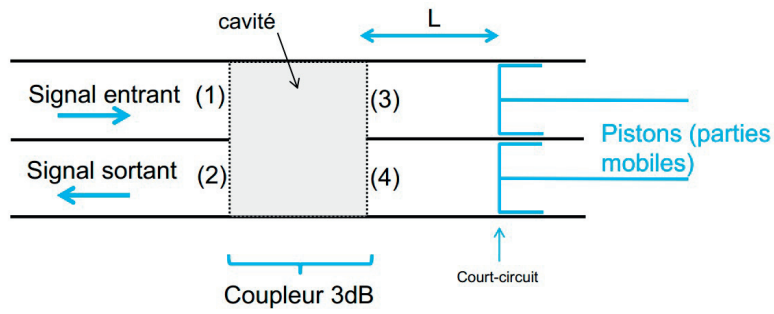
a delay of more than a nanosecond with a precision below the ps. In terms of optical path length it corresponds to hundreds of mm, with a precision of a few dozens of micrometers. It is not necessarily impossible, but taking into account both the limited space available and all the fabrication tolerances that could have an impact on the propagation of the signal, it is indeed challenging. As a comparison, the NATALIA project developed previously at LEMA [1] required an elevation half-power beamwidth of around 18° , which implies a steering accuracy of several degrees easily.

We can now discuss the practical aspect of creating a beam steering, and we thus start by presenting the ideas that Dassault Aviation brought as a suggestion; these ideas were suggested *in principle*, but no prototype of any kind was produced to validate them, and they are really open for discussion. The first suggested possibility (shown in Fig. 2.7a) consists of a hybrid coupler with its four accesses; two of them are used as input, and the remaining two are loaded with tunable stubs. Thanks to these two degrees of freedom, variable phase shift / delay and proper impedance matching can be achieved. It is unfortunately unclear whether it is indeed a phase shift or a delay, because of the nature of the hybrid coupler that basically acts as a phase shifter.

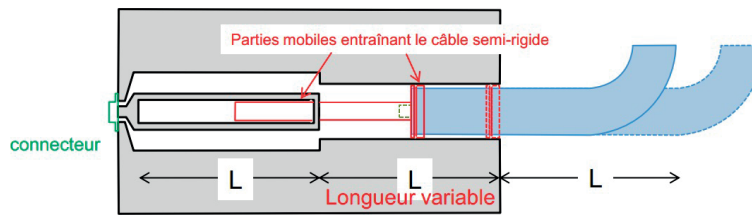
Anyway, a second solution was also proposed by Dassault Aviation and is reported in Fig. 2.7b. The idea stems from a patent issued in 1989 by Knorr (Patent number : 4 843 355), who simply proposed to obtain a variable delay by mechanically changing the length of some flexible coaxial cable. A variation over this idea, still imagined by Dassault Aviation, consists in variable length waveguides with TE modes propagating (Fig. 2.7c and 2.7d). But TE modes, contrary to TEM modes typical from coaxial cables, exhibit a propagation speed (and a guided wavelength) that depend on frequency, and we strongly suspect that it could again lead to a squinting effect; this remark is also valid for the hybrid-coupler solution, and thus only the original Knorr solution would be preferred from now.

Our criticism will now more evolve to the practical feasibility of this system in a Ku-band, and even more in Ka-band contexts. Each line of elements requires its own variable delay line; is it possible to fit 32 such coaxial cables below an array ? It turns out to be quite challenging, even if one considers the possibility of bending them somehow (as was suggested by Dassault Aviation). But then, is it easy to manufacture bended coaxial cables, and to achieve a precision of a few dozens of microns ? Moreover, the tolerances would become even tighter in Ka-band, due to the decrease of the overall size of the array.

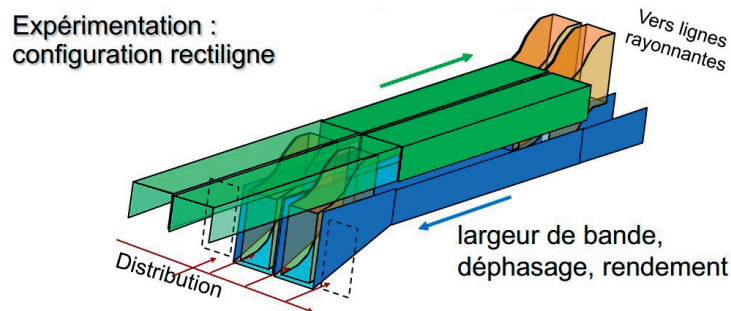
Considering all these problems that rised progressively over the first semester of research, we decided to make a bibliographic study of existing systems for beam-steering. It doesn't pretend to be exhaustive, but it gives at least a good idea of potential solutions, or at least it makes a list of systems that would *not* lead to a solution. Among those systems, one of them looks very promising, and it will be presented separately in the end. It is indeed a purely mechanical design, well adapted to the global requirements, that could replace Dassault aviation's original idea and perform what was intuitively intended to be done in a somehow different way.



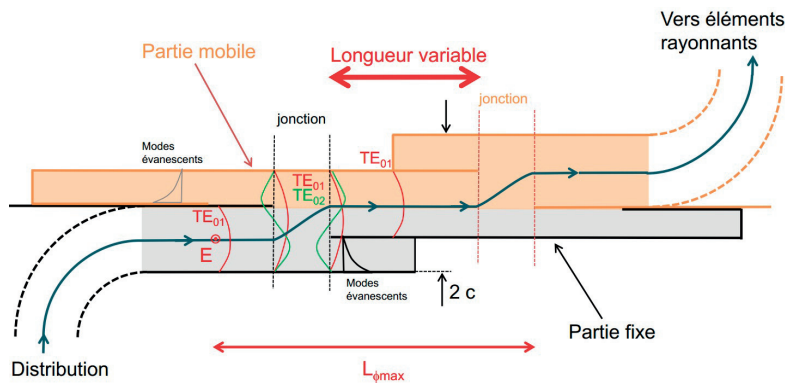
(a) A mechanical phase shifter based on a hybrid coupler.



(b) Delay line made up of a variable length coaxial cable.



(c) Parallel variable delay lines for beam steering.



(d) Cross view of a possible variable delay line more details.

Figure 2.7: Originally proposed solutions for a mechanical phase shifter / delay between radiating lines (in french).

2.3.2 A bibliographic review of beam steering systems

In this part, we chose to present three solutions found in the literature for beam steering, which looked to be promising at first sight. We don't have any intention to be exhaustive at all.

Solution 1 : Electronic solutions involving mixers

The first solution that we present here is particularly appealing, and looks to be well suited for our requirements; it was published in 2008 [22] and involves only basic electronics. Starting from Fig. 2.8, we can give a description of its operation :

- The signal entering on the left is mixed with the output of a Voltage Controlled Oscillator (VCO), which shifts its spectrum around some frequency value.
- Then it flows through a circulator and a so-called *chirped delay line*. This line exhibits a quite complex characteristic impedance profile, first described in [23] and then adapted from optic fibers to microstrip technology [24] [25]. We are not going to report it in detail for the sake of brevity, and the only things that need to be known are the following : the profile is chosen in such a way that, when a signal enters this line, it will be completely reflected at some point, which depends on its frequency. Thus, the time delay for the signal to enter the line and to come back depends directly on the VCO frequency. Thanks to a second mixer, we restore it to its original frequency.
- Some amplification stages follow to compensate the losses induced by both the chirped line and the mixer; but most important is the presence of a second chirped line, used to compensate the dispersive effect of the first one. Indeed, chirped lines are *by definition* dispersive and it obviously has a strong impact on the input signal.

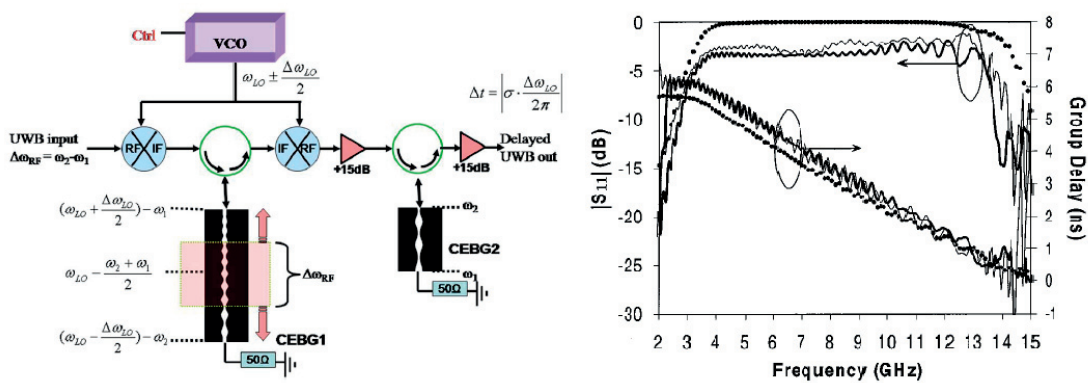


Figure 2.8: A variable TTD system using chirped delay lines.

An apparently weak point of this design is the necessity to use several circulators, especially if many of these circuits have to be implemented in an array. It was proven that one can

Chapter 2. Global architecture of the array

circumvent this issue by using two coupled chirped lines instead of a simple one [26]. But some practical problems arrive then, such as the very long simulation times. The worst of them is the appearance of a ripple in the delay (Fig. 2.8, right chart) that can easily reach several hundreds of picoseconds. It is neither accidental nor due to tolerances issues, and it can only be mitigated by increasing the chirped line length in a prohibitive way, or by compensating it with second slightly different line. We tried both of these methods, and they were far from giving a reasonable solution with a good accuracy.

We can also mention the existence of a similar design using a metamaterial line instead of a chirped delay line [27], but although it is free from any ripple it turns out to be a fundamentally narrow band solution which cannot fulfil our very tight requirements. These designs were consequently rejected as potential candidates.

Solution 2 : Rotman lenses

A popular solution for squint-free beam forming networks is given by Rotman lenses. As their name suggest, they belong to the family of systems inspired from geometrical optics, namely systems whose overall size is much larger than the wavelength. A typical microstrip Rotman lens can be seen in Fig. 2.9; it is simply a printed circuit with the shape of a classical lens, whose inputs and outputs are microstrip lines respectively with blue and red caps on the connectors. Following the analogy with optical lenses, and if all the dimensions are properly determined, we have the following correspondances :

- Inputs correspond to focus points, isolated from each other (in optics, light from a punctual source doesn't flow "back" when it passes through a lens).
- Outputs correspond to a wavefront with different delay distributions depending on which input is excited.
- Outputs covered in black on the picture correspond to matched isolated ports, which need to be there to model what would be "vacuum" around the lens.

A recent and quite complete reference for Rotman lenses is the PhD thesis of Leonard Thomas Hall (2009) [3], from which the picture was taken. It explains from the very beginning to the most advanced points how to design and simulate these beamforming networks. Although this solution is squint-free, easy to manufacture and quite compact, the following practical drawbacks turn out to appear :

- In order to obtain a proper impedance matching as well as a good isolation between accesses, it is necessary to use tapered transition between them and the lens. This results quickly in a huge -if not prohibitive- amount of parameters to co-optimize in simulations, once the closed-form expressions reach their limits.

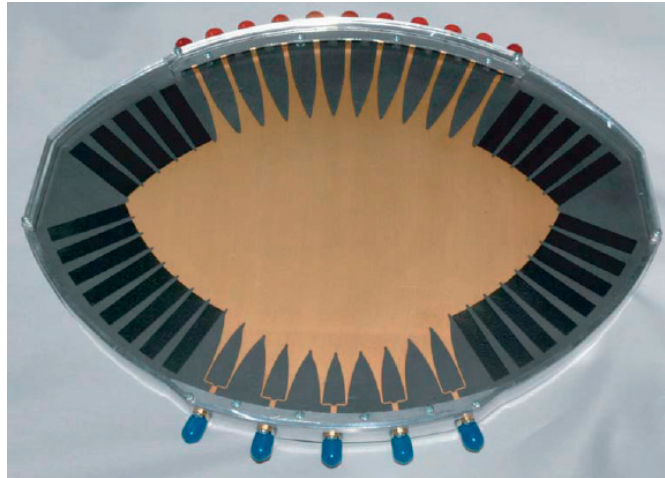


Figure 2.9: A typical microstrip Rotman lens in Ku-Band, with 43 inputs (on the left) and 16 outputs (right); courtesy of [3].

- Even if lots of efforts are devoted to these optimizations, impedance matching and isolation between accesses seem to remain a weak point, at least as far as we could see in the literature. Return losses of -10dB are quite standard values.
- It is not strictly speaking a system that allows continuous beam steering, but it rather generates a plenty of discrete beam positions. In order to achieve beam steering from 0° to 60° with a precision of 0.5° , 121 inputs would be needed, plus 32 -or more- outputs for the radiating lines.

We will thus put this idea aside, and come back on the quasi-optical systems family in the next section where a slightly different but more promising setup will be presented.

Solution 3 : Nonlinear Delay Lines (NDL)

Nonlinear Delay Lines (NDL) appear as a quite natural way of implementing a variable TTD for phased arrays. It stems from a simple idea : delays are simply produced by microwave transmission lines, and they depend on both its physical length and its constant of propagation. Earlier in this chapter, we tried to modify mechanically the length of a coaxial cable in order to control the delay, and now this method is about studying the complementary point of view; in order to control the propagation constant of the line, it is suggested to load periodically the line with varactor diodes. The capacitance of these diodes changes when a DC bias voltage is applied to them. The distance between the capacitances has to be kept small compared to the wavelength, in such a way that the loading appears as a continuous contribution to the natural per-unit-length capacitance of the line. The propagation constant thus becomes :

$$\beta = \omega \sqrt{L_{line}(C_{line} + C_{diode}(V))}$$

The NDL technology was implemented with lumped varicaps for Ka-Band in [28] and [29]. Unfortunately, a lot of very small (and, in Ka-Band, expensive) resistors are required, and the resulting delay line becomes quickly long, costly and difficult to build. An alternative implementation scheme that was studied at LEMA a few years ago is the so-called *Distributed MEMS Transmission Line* (DMTL), where MEMS stands for *Micro ElectroMechanical Systems* [4] [30]. In that case, the transmission line is integrated in a chip and the lineic capacitance is -very roughly speaking- varied by "opening and closing" microscopic switches; Fig. 2.10 shows a photo of such a switch.

Here again, the practical manufacturing does not involve simple mechanical or PCB process, and we can be sceptical about the use of this technology in our context. But there are even worse drawbacks inherent to the NDL system. First, the characteristic impedance of the line changes together with the propagation constant, which can degrade the return loss. But also, the insertion loss turns out to stay frequently below -6dB and -10dB, for lines producing around 200ps of maximal delay. Much longer -and lossy- lines would be required to approach 1ns of delay, which looks impracticable. Moreover, it is not even sure that the precision obtained with this technology would be sufficient.

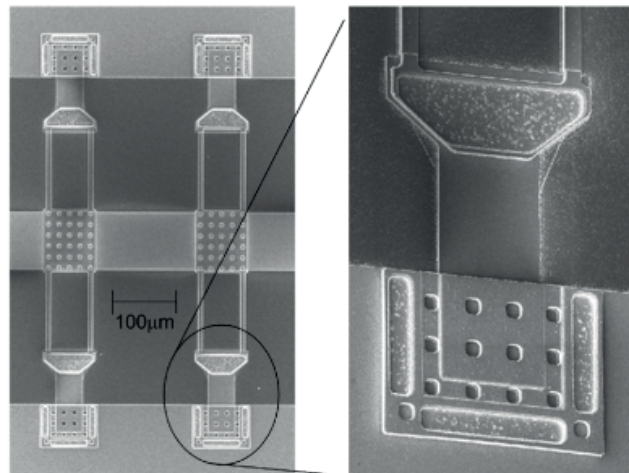


Figure 2.10: Photo of a Distributed MEMS Delay Line (DMTL) usable as a variable delay in phased arrays. Courtesy of [4].

2.3.3 A recent SIW-based mechanical system

Recent works have been led in Rennes since 2012 to investigate a class of mechanical beam steering system based on Substrate Integrated Waveguide (SIW) technology. It is reported here with a particular interest because it may be exactly the kind of system that would be required for our purposes. In a nutshell, this solution is quite compact, purely mechanical, and has been proving to produce squint-free beam steering in Ka-Band on a wide range of angles. This design is originally intended for low-cost automotive radar applications.

The concept presented here is referred to as "SIW Slotted Waveguide Array With Pillbox Transition" and is presented in a couple of papers [31] [32]. Perspective, top and side views are visible respectively in Fig. 2.11a, 2.11b, and 2.11c. Let's decompose and analyse it part by part :

- The overall system is made up of a stack of two PCB produced in identical substrates; the SIW technology was chosen to produce easily the metallic walls required for guiding the waves.
- The interface between the upper part and the bottom part consists of an integrated parabola reflector, and a set of apertures for the energy to flow from the bottom to the top.
- In the upper part, a set of parallel slotted waveguides are used for radiation. This aspect is not the most important, and in principle this radiating part could be replaced with a solution based on patch antennas.
- The feeding part is based on a horn that is moved along the focal plane. The global dimensions of the circuit are large compared to the wavelength, so the approximations of Physical Optics are valid and a qualitative explanation for the operation can be given as follows. The input horn excites a quasi-Transverse Electromagnetic (quasi-TEM) mode in the bottom substrate, with a cylindrical phase wavefront. The parabola achieves then a double role : first, it reflects the wave through the apertures to the upper substrate, exciting a quasi-TEM mode also. Second, it transforms the cylindrical wavefront into a planar one, whose direction classically depends on the position of the feed on the focal plane.

To be more accurate, the TEM-mode propagation direction depends on the ratio between the distance from the feed to the axis of the parabola and the parabola focal length. This effect provides the proper delay distribution for a continuous beam scanning. We can now reproduce some key parameters that are given by the authors, even though some geometrical distances were not disclosed. Both substrates were chosen to have thicknesses of 0.508mm, and relative permittivities of 2.2; it would correspond to some Rogers RT/5870. In this substrate, the wavelength at central frequency (24.15GHz) is $\lambda_d = 8.37mm$. The focal length and diameter of the reflector equal $10\lambda_d$ and $15\lambda_d$ respectively, leading to a ratio $F/D = 0.67$.

Chapter 2. Global architecture of the array

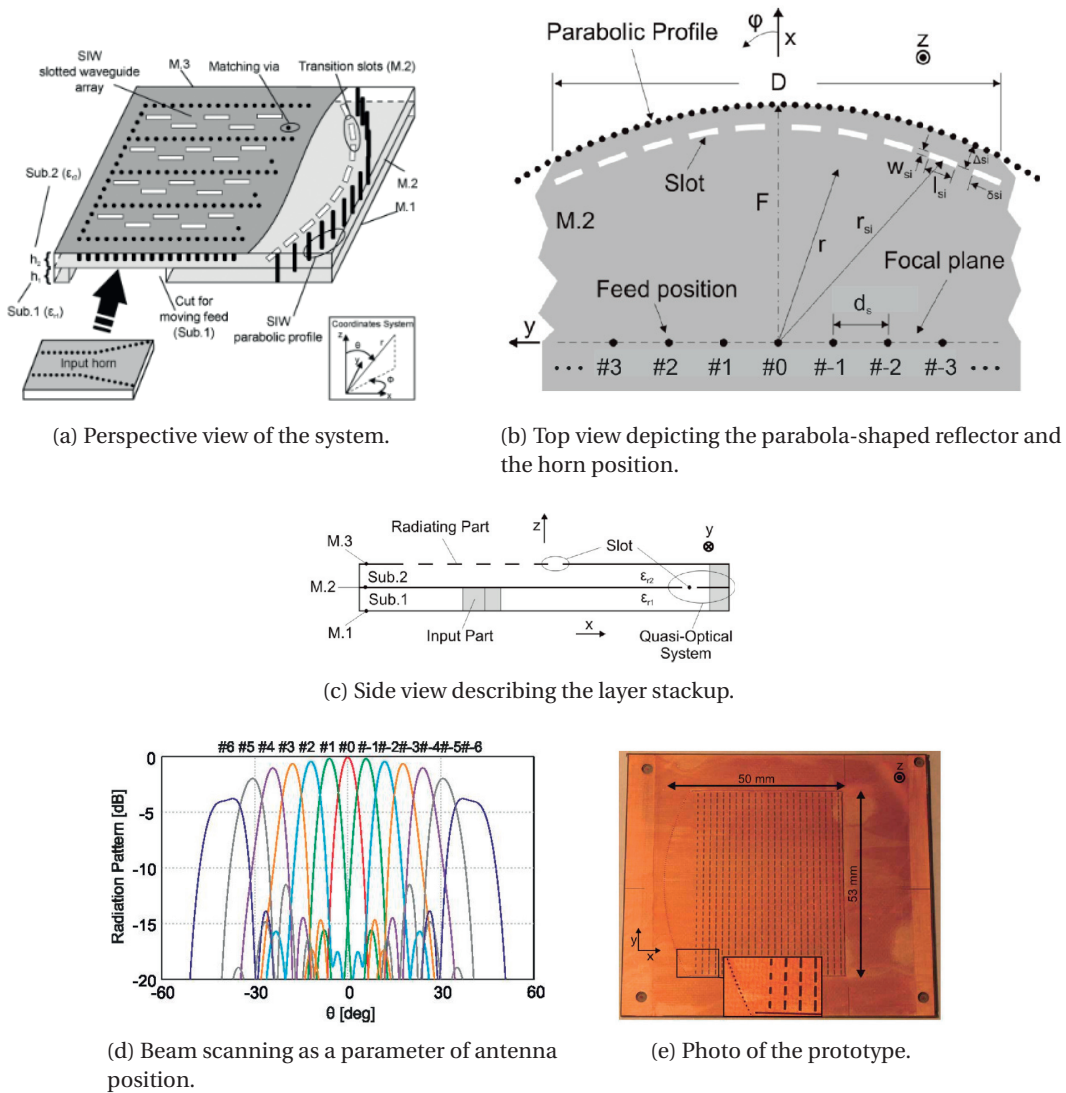


Figure 2.11: A purely mechanical system for beam-steering. SIW design in Ka-Band, around 24GHz.

The horn aperture width is $1.5\lambda_d$, the pin radii 0.4mm and the distance between the parabola pins 0.8mm.

Considering our goals, encouraging results have been obtained by the authors around 24GHz : an -10dB impedance of 5%, an efficiency around 70% and a clean beam steering beyond 30° for an array made up of 23 radiating waveguides (See Fig. 2.11d).

3 A first Rx-Band Element

Why do simple when one can do complicated ?

Fundamental Shadok rule

In this chapter, we enter for the first time inside the heart of the thesis, namely the design of printed antenna elements. Since dual-circular polarization is required, directional couplers will be involved somehow and a part of this chapter will be devoted to them. The study is subdivided in the following parts.

First, a small section will be devoted to the definition and basic properties of the Axial Ratio (AR). This term already appeared in the introduction of this thesis, and it was then assumed that the reader was familiar with it. Still, it is necessary to make clear the specific definition of AR being used in this thesis amid the many possible ones.

Then, the qualitative study of a first stacked patches structure will be performed as a starting point to understand the underlying concepts important for planar antennas. We will continue with a review of existing directional coupler topologies, in order to choose the best-suited one for our bandwidth requirements, at least for the relatively wide Rx Ku-Band (10.7GHz-12.7GHz). As will also be described, it turned out to be necessary to bring an improvement to this coupler in order to be able to use it in our context.

At the end of this chapter we present an element that was the first serious attempt to get an antenna working in the Rx Ku-Band. Results were lukewarm and can be definitely improved. Therefore the conclusion of this chapter summarizes the lessons learned and paves the way for the corrections and improvements to be described in the next chapter.

3.1 Generalities about circularly polarized planar antennas

3.1.1 Some definitions about the Axial Ratio

The Axial Ratio (AR) is a well known figure of merit used to characterize the purity of a circular polarization. Yet, it is not obvious to set a definition for it and historically, several of them have been produced. The classical book of Kraus [33] provides a discussion on this topic, and the more recent and very famous 1973 paper by Ludwig [34] threw the basis of what are now called to *Ludwig definitions* of the Cross-Polarization, used in most simulation softwares. In that context, this section is nothing more than a reminder of what is usually being taught to students in antenna courses.

In the far field of an antenna, the direction of propagation of an electromagnetic wave is perpendicular to the sphere that is used to define the spherical coordinates. Since the electric field is itself perpendicular to the direction of propagation (or equivalently to the Poynting vector) one can work in the plane defined by the \vec{e}_θ and the \vec{e}_ϕ vectors of the spherical coordinates. The electric field can then be decomposed into the sum of two linearly polarized waves following these vectors and oscillating at the same frequency, which results in three possible situations. Either the field is in fact reduced to a single linearly polarized wave; or if both linearly polarized waves are in phase and of same amplitude (perfect circular polarization). Or, in any other cases, an elliptically polarized wave is obtained.

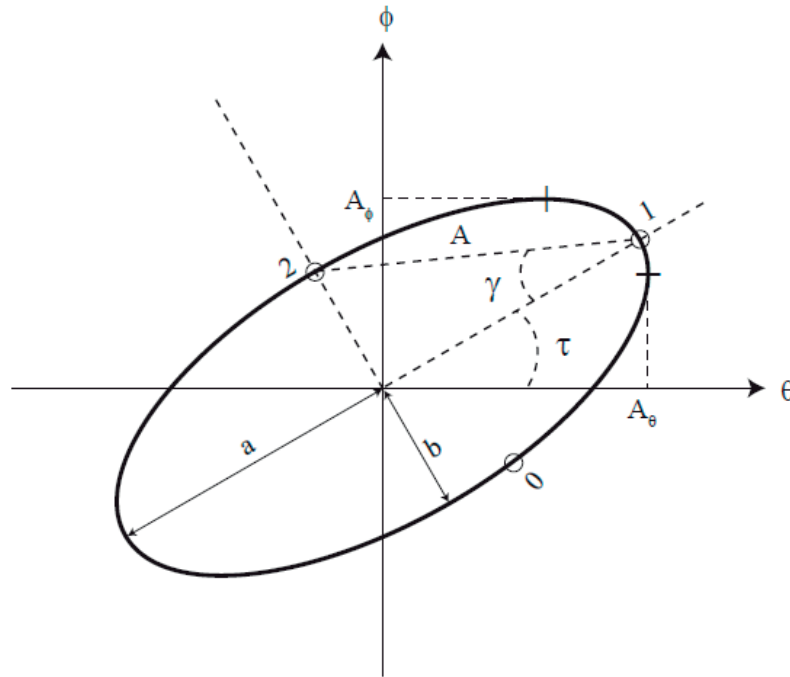
The geometrical parameters of the "polarization ellipse" are described in Fig. 3.1, and a typical Right Hand Circular Polarization (RHCP) is also depicted at three different moments in time. If the electric field vector were turning in the other sense, it would correspond to a Left Hand Circular Polarization (LHCP). If we want to know "to which extent" a wave is elliptically polarized, we will use the AR that is now defined by the ratio of both axes of the ellipse :

$$AR = \tan(\gamma) = \frac{b}{a}$$

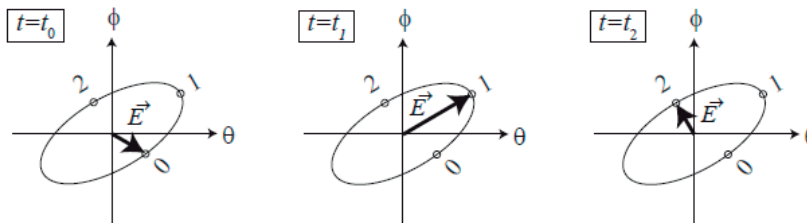
Which provides a value between 1 for a perfect circular polarization and 0 for a perfect linear polarization. If a dB value between 0 and ∞ is preferred, one can compute instead :

$$AR(dB) = |20\log_{10}(AR)|$$

3.1. Generalities about circularly polarized planar antennas



(a) Definition of the different geometrical parameters of the ellipse.



(b) Evolution of the electric field of an incoming wave at three different moments in time (RHCP - the wave is assumed to travel "towards the reader").

Figure 3.1: Illustration of an elliptically polarized electromagnetic wave. Courtesy of [1].

The decomposition of the electric field gives the following set of equations :

$$\begin{cases} \vec{E}(\theta, \phi, t) = E_{\theta}(\theta, \phi, t)\vec{e}_{\theta} + E_{\phi}(\theta, \phi, t)\vec{e}_{\phi} \\ E_{\theta}(\theta, \phi, t) = A_{\theta}(\theta, \phi)\cos(\omega t + \alpha_{\theta}(\theta, \phi, t)) \\ E_{\phi}(\theta, \phi, t)\vec{e}_{\phi} = A_{\phi}(\theta, \phi)\cos(\omega t + \alpha_{\phi}(\theta, \phi, t)) \end{cases} \quad (3.1)$$

Where ω is the angular velocity, A_{θ} and A_{ϕ} are amplitudes, α_{θ} and α_{ϕ} are phases that can all be measured. The main challenge now is to be able to find the "tilt angle" τ as well as a and b ,

Chapter 3. A first Rx-Band Element

and from these values a post-processing software can deduce the AR. There are two different ways : either we consider the fact that the main axis of an ellipse correspond to extremal values of the electric field, and we are reduced to an optimization problem. Or we consider that the axes are such that they are at the same time perpendicular and separated by a quarter of period in time, which is enough to characterize them. In both cases we get :

$$\tau = \frac{1}{2} \arctan\left(\frac{2A_\theta A_\phi \cos(\delta)}{A_\theta^2 - A_\phi^2}\right)$$

With $\delta = \alpha_\theta - \alpha_\phi$ by definition, and the AR is given by :

$$AR = \frac{2A_\theta A_\phi |\sin(\delta)|}{A_\theta^2 + A_\phi^2 + \sqrt{(A_\theta^2 - A_\phi^2)^2 + 4A_\theta^2 A_\phi^2 \cos(\delta)^2}}$$

Yet, it happens sometimes that the electric field is not given (or measured) as the sum of two linear polarizations, but rather as the sum of two circular polarizations of LH and RH type; it is just another algebraic way to represent it, and in that case we admit that the AR is given by the simple and useful formula :

$$AR = \frac{|E_{RH} - E_{LH}|}{|E_{RH} + E_{LH}|}$$

3.1.2 General properties of patch antennas

Planar printed antennas are well-known and widespread solutions for the design of antenna arrays. They are especially appreciated for their low profile, low weight, ease of fabrication and in addition, a careful design allows to achieve a relatively wide bandwidth. The first traces of this technology appeared around 1953-1955 with the works of Deschamps [35], Gutton and Baissinot [36]; these papers are nowadays widely accepted as the very first pioneer publications about the topic. The development of planar printed antennas then continued slowly until the beginning of the 1980s, when Carver and Mink published a state of the art study of this domain [37]. At the same time Mailloux, McIlvenna and Kernweis published a survey paper on printed antenna arrays [38].

From the 1950s to the late 1980s, printed antennas mostly consisted of the following : a single microstrip patch (typically circular or rectangular) was etched on a substrate and excited either by a coaxial cable going through the ground plane, or directly by a microstrip input sharing the same substrate (see Fig. 3.2). In this case the patch alone -without the excitation- could be considered as a cavity with top and bottom PEC boundary conditions, and PMC boundary conditions on the side faces, because the current is ideally zero there. Then analytical models for the modes supported by this cavity could be derived, with closed form expressions for their resonating frequencies. The models were also refined to characterize the radiation occurring through the side faces, the fringing fields present at the edges or the input impedance depending on the feed position. All these results are gathered in the famous reference book of Balanis [39] for the interested reader.

Fortunately or unfortunately -depending on people's point of view- planar antenna engineering drastically changed since the end of the 1980s, due to the combination of two phenomena. Firstly, softwares based on numerical methods -Finite Elements, Finite Differences, Method of Moments- got more and more importance as the access to powerful computers became a standard for engineers. The fact that they implement easy parameter sweep capabilities, and for the most recent commercial ones powerful 3D modelers make it easier for anyone to model complex structure with some (little) mathematical background. Secondly, the planar antenna technology became more and more mature, with hundreds of publications dedicated to them and increasingly sophisticated structure. In that context, it became at the same time hopeless and useless to develop complicated analytical models for each of these antennas.

Nowadays full books are dedicated to planar antennas only, and in this category we really recommend the 2011 reference by Lee and Luk [40]. Unless stated otherwise, all the results that we are going to state in this section will be taken from it.

The most important for an engineer starting such a design is to keep in mind a list of qualitative properties of printed planar antennas. Together with it comes a list of tradeoffs between their different properties, especially impedance bandwidth, directivity, size and mutual coupling with neighbors.

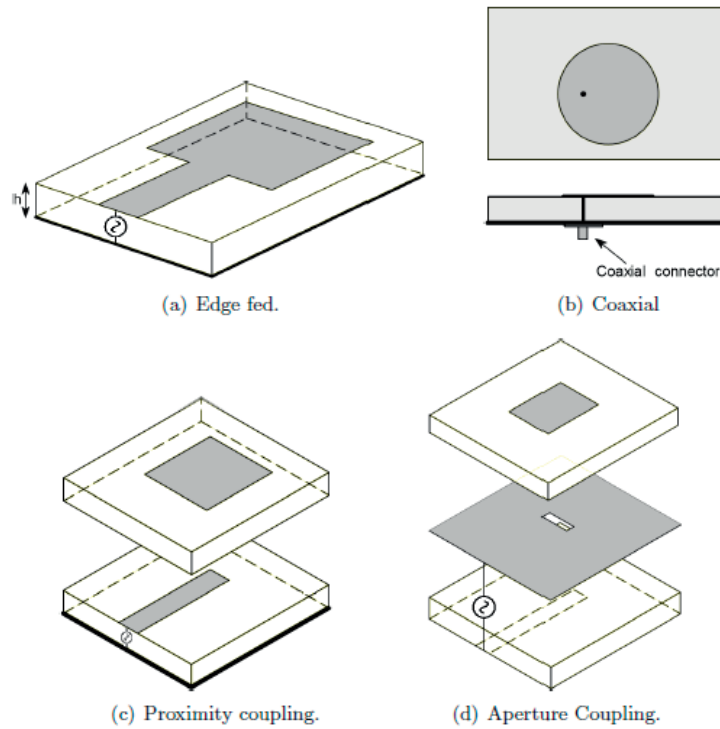


Figure 3.2: Basic printed planar antennas and their most classical feedings. Courtesy of [1].

Rule 1 : When the permittivity of the patch substrate is increased, the electric length of the waves in this substrate decreases proportionally. Thus, the size of a patch corresponding to a given operation frequency decreases almost proportionally; we say "almost" because there are some nonlinear effects in the process due to the fringing fields.

Rule 2 : The main fundamental consequence of this decrease of size is that the directivity of the antenna element will decrease as well, which as we will see below is sometimes required. This engineering "rule of thumb", the fact that antenna size has an impact on its directivity, can unfortunately not be explained without a minimal use of mathematics. In a nutshell, it stems from the fact that the radiated field profile of an antenna is calculated by performing a Fourier transform on the source fields; and the Fourier transform of a sharper "signal" is "wider". This property is also well-known in signal processing, where it is perfectly illustrated by the Dirac δ function.

Rule 3 : When the *electric thickness* of the substrate is increased -by increasing either its physical thickness or its permittivity- *surface waves* are getting more and more excited. They can become the source of a serious loss of energy, but also of a more and more prohibitive mutual coupling with the neighboring elements that are reached by these waves. A good treatment of the theory of surface waves is provided in [41] Ch. 3. An important result that can be proved is that if the inequality $h < \frac{c}{4f_{max}\sqrt{\epsilon_r-1}}$ is respected, the TM_0 mode is the only one

3.1. Generalities about circularly polarized planar antennas

that will propagate and the phenomenon will be limited. Here, \mathbf{h} is the height of the substrate, \mathbf{c} the speed of light in vacuum, f_{max} the maximal frequency and ϵ_r the relative permittivity of the substrate.

Rule 4 : There are two ways to improve the impedance bandwidth of a printed antenna element : either the height of the substrate has to be increased, or its permittivity has to be decreased; both can of course be done at the same time, but each of these approaches can enter in conflict the two previous rules. The underlying physical explanation of this rule can be stated as follows : patch antennas are resonant structures, and it is known that the bandwidth of resonators in general increases if their losses increase. Here the main source of "losses" is the radiation itself, though is not strictly speaking a loss. And in order to ensure a better radiation, one should in general ensure that the fields around the antenna element are less "confined", which is the case with both aforementioned tricks.

We shall come back to the counter-intuitive idea raised in rule 2, that the directivity of a single element should be decreased to some extent. Indeed, if the final goal is to achieve a high-directivity at array level, it could be a good point to have already a high directivity at element level. Yet, an elementary physical reasoning invalidates this claim : if an antenna element is too directive, it radiates mostly in the broadside direction, but very few for larger angles. Then, it simply becomes impossible to steer the beam correctly towards these angles (or, the *scan loss* is too important). In general we can say that the ideal radiation pattern of an antenna element for an array has to be monotonous, to exhibit a good azimuthal symmetry and to have a "low" directivity. The *radiation pattern* here in fact refers to the so-called *embedded radiation pattern*, corresponding to an element surrounded by neighbors (matched but not fed); this one is opposed to the *isolated* radiation pattern.

These concepts were discussed already back in the 1960s in a more rigorous and mathematically involved way [42] [43]. The main idea is that the directivity for a large array is the product of the number of elements by the directivity of an element. Then, because for a large antenna the directivity is fixed by the relation :

$$D = 4\pi \frac{A_e}{\lambda^2}$$

a theoretical upper bound can be derived for the directivity of each element. If it is not respected, mutual coupling with neighbors will raise to decrease the gain automatically. All these phenomena depend on the array lattice and the distance between elements; in our case we will consider during the rest of the thesis a square lattice with an inter-element spacing around a half-wavelength, and we will target a directivity of 6dBi if possible.

3.1.3 Design of a stacked patch antennas

Now that the basics are clearly set, the family of antennas that we will be more interested in is the *Strip Slot Foam Inverted Planar (SSFIP)* antenna, already mentioned in the introduction of the thesis. This concept was developed around 1988 at LEMA by J.F. Zurcher and F. Gardiol and a full book was dedicated to it a few years later [14]. Its main particularities can be summarized as follows :

- The patch is excited through a slot in the ground plane; the feeding circuit is kept entirely below this ground plane, which protects the design from spurious radiations.
- The manufacturing only involves etching and sticking operations, which makes it easier to realize than the coaxial excitation (especially if a large array is being considered).
- With this excitation scheme, it is possible to replace the antenna substrate by a *thick* layer of foam. Its permittivity is very close to the one of air ($\epsilon_r = 1.06$) and it has various implications as we saw previously : surface waves become completely negligible, the directivity is quite high for a single patch structure (one should expect to achieve a bit more than 10dBi) and the impedance bandwidth can reach 20% (for $S_{11} < -15\text{dBi}$). This improvement is of uttermost importance : the most basic patch antennas using thin microstrip substrates ($\epsilon_r > 2$ and an electric thickness of around $\frac{\lambda}{10}$) reach barely a few percents.
- Depending on its size, the slot can start to resonate and to contribute to the enlargement of the bandwidth by adding an additional resonance in the system. It unfortunately results in a back radiation of a fraction of the energy by the slot, but there is a remedy to this situation that will be presented later.

Since we are targeting a bandwidth of around 17% with $S_{11} < -20\text{dBi}$ if possible, getting an even more wideband operation would be a good point. Unfortunately, we also need to decrease the directivity, which implies a change of substrate and thus as we saw before a decrease of the bandwidth. In this situation, antenna engineers typically resort to the *stacked patches* structures [44]. It consists in adding a second patch on top of the main one, which acts as a second resonator; if both resonating frequencies are close to each other, both bandwidths merge into a single larger one.

We are already dealing with a quite complex structure, involving many parameters to optimize. Since no analytical model is directly available for this kind of design, modeling and simulations in commercial softwares have been used to lead the development. We are now going to describe the different steps that were performed to get a first working antenna element, before reporting on the results.

3.1. Generalities about circularly polarized planar antennas

Step 1 : Modeling and choosing the most obvious starting values for the different parameters.

The process starts by modeling a stacked patch antenna in Ansoft Designer, excited by a microstrip line through a central rectangular slot. Ansoft Designer is a general modeler and simulator for solving multilayer 2D problems, using Green's functions and the Method of Moments. This numerical method runs much faster than, for instance, the FDTD or FEM methods implemented in other commercial softwares. The drawback is that it cannot handle complex 3D structures, and in particular it is not possible to model a finite ground plane with the diffraction occurring at its edges. Hence the goal of this first model is to be able to simulate quickly and roughly the matching of the antenna when many parameters are changed at the same time.

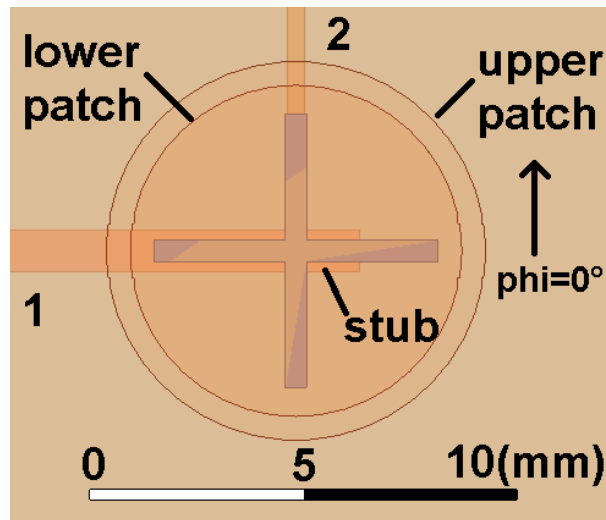


Figure 3.3: Top view of a stacked patch antenna excited through a cross-shaped aperture by two orthogonal microstrip lines.

There are two families of parameters :

- Substrate parameters, namely their type (in particular their permittivity) and thicknesses. There are three substrates in total : two for the patches and one for the feeding line.
- All the other geometrical parameters (see Fig. 3.3) : the size of both patches, the length and width of the slot, the width of the microstrip feeding, the length of the matching stub.

Chapter 3. A first Rx-Band Element

We can take intuitive decisions about some of them, using a pragmatic approach :

- The feeding substrate has to be "thin" and to exhibit a quite "high" permittivity. It will ensure that the energy of the field will remain well confined below the line, resulting in a better coupling with the patch. Additionally a higher permittivity can imply a smaller size for some parts of the feeding system. The 0.203mm thick RO4003C substrate was chosen for its ease of manufacturing, availability at LEMA and popularity in the world of antenna design.
- The width of the feeding line is chosen to correspond to the characteristic impedance of 50Ω for this substrate.
- The length of the slot was fixed to be a half-wavelength at central frequency, in order to start the simulations around its resonance. It was empirically found that the width of the slot has very little influence on the bandwidth compared to the other parameters, so it was chosen fixed to 0.5mm.
- The length of the stub was chosen to be 1mm in a somewhat arbitrary way. If the simulation port is de-embedded towards the slot, the stub acts as a pure reactance in parallel to the rest of the impedance. Its effect in the admittance Smith chart is to move the locus of points (impedance vs frequency) on circles of constant real part. This effect can be to a large extent decoupled from the effects of the rest of the parameters, that's why the stub fine-tuning is in fact kept for the second phase of the optimization.
- The substrates for the patches have to take into account the aforementioned constraints in terms of thickness and permittivity, regarding the surface waves or bandwidth issues. We decided to model the top substrate as foam (like in SSFIP) of variable thickness, as foam can be manufactured in our workshop to control it. The bottom substrate must have a larger permittivity to decrease the size of the element; all the substrates available at LEMA, verifying $2 < \epsilon_r < 3$ and having a thickness between 1mm and 2mm (reasonable fractions of wavelengths in Ku-Band) were considered as parameters in the model.
- The patches have been chosen to be circular; this shape is at the same time very symmetrical and very simple by essence, and it may be seen as the most popular and classical choice by default. The diameters of both patches were fixed to be a half-wavelength at central frequency, considering the relative permittivity to be the average of the one of foam and of the Rogers RT5870 substrate. In this way, one can expect their resonant frequencies to be close to each other and close to the targeted frequency range.

3.1. Generalities about circularly polarized planar antennas

Step 2 : Massive simulations on a set of parameters in two substeps.

Once the values (or at least the starting values) of the parameters have been chosen, a parameter sweep can be configured. The exploration took a night and nearly 300 different simulations were being performed. The effect of the slot length, the patch diameters and the substrates were considered *at the same time*. It is indeed difficult to separate clearly the effect of those parameters, as can be summarized as follows :

- The dimensions of the patches have a direct influence on the resonating frequencies.
- Their relative sizes have an impact on their mutual coupling.
- The substrates used also influence both of these effects.
- At the same time, the length of the excitation slot is a function of all these parameters since they all have an influence on the input impedance.
- But the length of the slot is linked to its resonant frequency, which is a potential factor of improvement for the bandwidth.

At the end of the process, the best solution was retained after a manual filtering. This "best solution" was defined with three criteria :

- The substrates used were as simple as possible; just a layer of Rogers RT5870 ($\epsilon_r = 2.33$) of thickness 1.57mm, and a layer of 2mm of foam. For non-integer values of foam thickness, it would be necessary to add up a manufacturing step, as they are not directly available for purchase.
- The loops in the Smith chart, corresponding to the different resonant frequencies, were of similar sizes and as close as possible to each other.
- They were close to the center of the Smith chart, or at least to the circle of real part 1, so that the stub can be used to achieve the matching.

A second simulation step included the stub as a new parameter, while the substrates were set to the found solutions. The parameter sweep was refined around the previously found values for each of them, and a complete solution was then ready for the last step.

Step 3 : Using a new HFSS model and introducing dual polarization.

In the last step, a new version of the previous model was drawn in Ansoft HFSS for the third set of (FEM) simulations. Since HFSS is a 3D software, antenna elements of any complexity can be simulated in principle, and it was thus a good practice to give up the more "limited" Ansoft Designer at this point. Additionally, these simulations were helpful as a validation of the results obtained previously in Ansoft Designer.

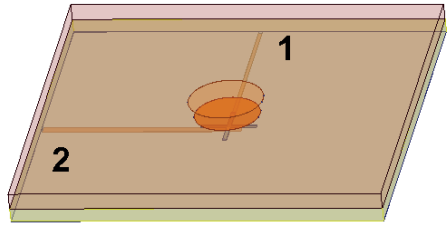
A second orthogonal slot was also added together with a second feeding line, in order to implement dual-linear polarization or equivalently dual-circular polarization if the proper phase shifts are applied between antenna accesses. Simulation results are reported in Fig. 3.4, and we can conclude this paragraph with a set of comments about them.

First of all, the S parameters are kept comfortably below -10dB from 10GHz to almost 16GHz, which is much more than required to handle both Rx and Tx channels. Though, the value of -10dB (in fact, -12dB) is still high for a single element, and it is difficult to ensure that it would operate correctly with its complete feeding system and the perturbation of neighboring elements.

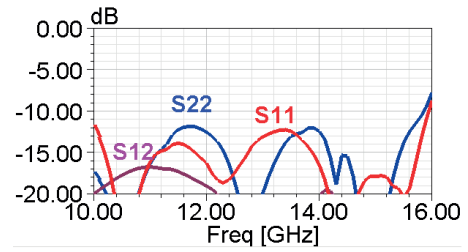
The radiation pattern (LHCP plot for a fixed azimuthal angle given as an example) is quite stable in frequency and monotonous. The directivity is kept between 6dBi and 7dBi, which is close enough to the ideal value of 5dBi. This is a strong point of the element.

The AR is also stable in frequency and keeps a value below 6dB for angles ranging from $\phi = 0^\circ$ to $\phi = 60^\circ$. This 6dB value is much compared to the 3dB value that is required in our project; yet, it is not surprising to obtain such a result for a very first antenna element, because no particular precaution has been taken to improve it. The next chapter of this thesis will be entirely devoted to this topic.

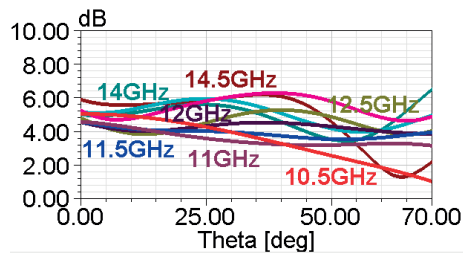
3.1. Generalities about circularly polarized planar antennas



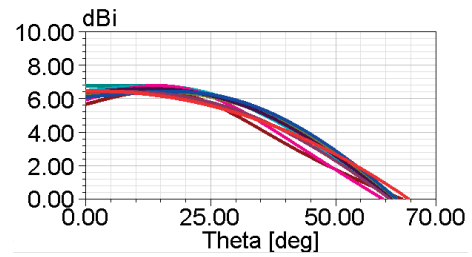
(a) Perspective view of a stacked patch antennas excited by two orthogonal microstrip lines through a cross-shaped aperture (HFSS).



(b) S parameters of the stacked patch antennas.



(c) AR of the stacked patch antennas (LHCP $\phi = 0^\circ$).



(d) Directivity of the stacked patch antennas (LHCP $\phi = 0^\circ$).

Figure 3.4: HFSS model of the stacked patch antennas.

3.2 Choice and modification of a directional coupler

Directional couplers are key microwave elements used to produce dual-circular polarization. These circuits are highly symmetrical and they always involve four inputs/outputs. The theoretical operation of directional couplers is done in the general framework of the study of four-ports lossless, linear and reciprocal microwave circuits; see for example [45] Ch. 7.

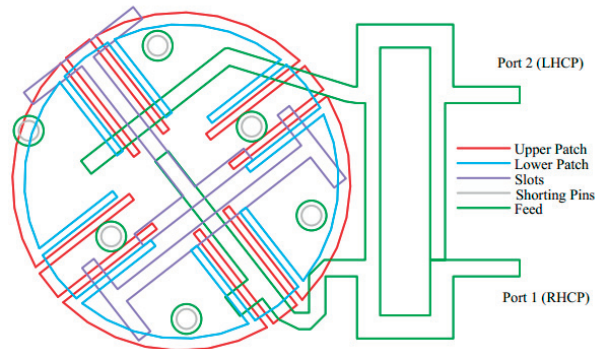
The most popular directional coupler is the microstrip branchline coupler, which can be used as an example to recall the operation of directional couplers in general. In Fig. 3.5a for example, a schematic top view of the patch element that was developed at LEMA for the NATALIA project is reported. It consists of a stack of two patches (in blue and red) excited by two excentered H-shaped slots (in purple) and by a branchline coupler in green.

A branchline coupler is basically a square made up of a couple of 50Ω lines and a couple of $50\sqrt{2} = 71\Omega$ lines, whose length is a quarter wavelength at central frequency. In that case, the surface occupied by the circuit was reduced by meandering two of the lines, but it doesn't change anything to our discussion.

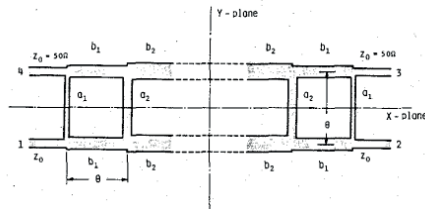
The operation of the branchline coupler that we are going to describe can be explained using the even and odd mode decomposition technique (see [45] Ch. 7. still). Our couple of inputs are called port1 and port2 here and they are isolated from each other around the central frequency. If one of them is excited, the incoming power is equally split between both outputs (on the left) in phase quadrature, thus generating a circular polarization. The phase distributions at outputs are such that port1 would correspond to RHCP in this example, while port2 would correspond to LHCP.

Branchline couplers in general exhibit bandwidths ranging from 10% to 20% at most; in order to cover the Rx-Band (17%) this performance is just enough. In order to increase the quality of the polarization or the S parameters of the overall antenna, one could think of using a more advanced directional coupler topology. Moreover at the beginning of the thesis, we had in mind the possibility of merging the Rx-Band and Tx-Band operations into a single array, which would require a more wideband coupler (around 30%). We gave up this idea later for practical reasons, but it motivated the survey of existing solutions that we are going to present now.

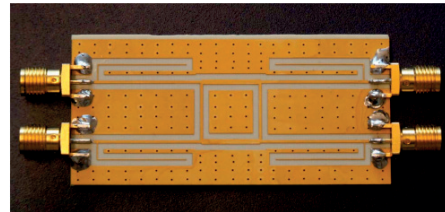
3.2. Choice and modification of a directional coupler



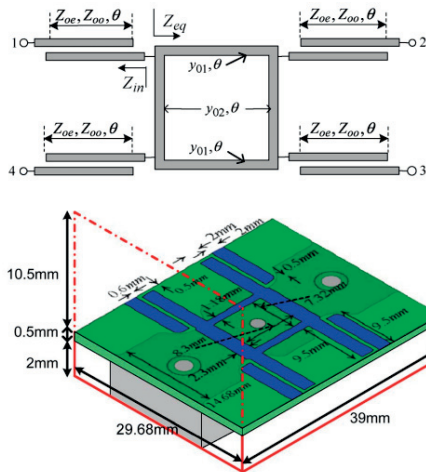
(a) Complete NATALIA antenna element developed previously at LEMA. Courtesy of [1].



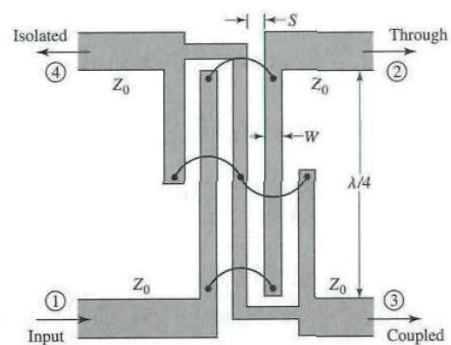
(b) Cascaded directional couplers for increased bandwidth operation. Courtesy of [46].



(c) Wideband coupler using stub matching at its inputs. Courtesy of [47].



(d) Directional coupler using coupled-lines impedance matching. Courtesy of [48].



(e) The Lange coupler. Courtesy of [49].

Figure 3.5: A survey of various existing directional couplers.

Chapter 3. A first Rx-Band Element

A first well-known solution is to cascade and to merge several branchline couplers (Fig. 3.5b). This presents two drawbacks : firstly, the compactness suffers a lot from this approach; secondly, it turns out that the different microstrip lines have to handle quite extreme values of impedance (hundreds of Ohms sometimes) which make the manufacturing particularly delicate. A discussion on the way to mitigate it is provided in [46].

Another whole family of wideband directional couplers comes from a result of Riblet [50]. He proved that, because of the high symmetry of branchline couplers (their behaviour is the same seen from any of the inputs/outputs) it is enough to add four identical matching networks at each access in order to increase not only the impedance matching bandwidth, but also immediately the amplitude imbalance bandwidth between outputs. A variety of topologies can then be derived depending on the matching circuit chosen : simple stubs [47] or coupled lines [48] have been suggested for example (See Fig. 3.5c and 3.5d). Unfortunately the same issues are always observed : the compactness of these solutions is not optimal, and the accuracy required to manufacture the proper matching stubs or coupled lines can be a source of troubles.

A last classical solution is given by the Lange coupler [51], depicted in Fig. 3.5e. This structure unfortunately involves tightly coupled lines and delicate bonding wires, which make it impracticable at our frequencies and for our facilities.

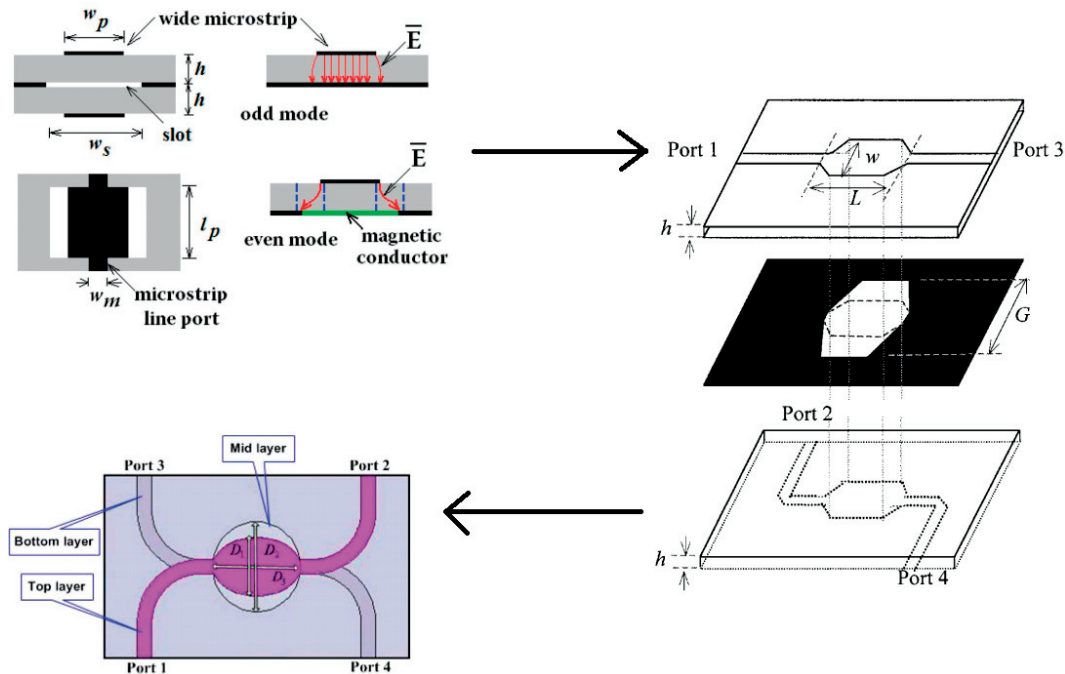


Figure 3.6: The recent evolution of aperture-coupled directional couplers. Courtesy of [5], [6] and [7]

3.2. Choice and modification of a directional coupler

The structures that proved to be the most suited in our case are the aperture-coupled directional couplers, depicted in Fig. 3.6. The most basic form of these couplers consists of two rectangular patches etched on either side of a common ground plane, and coupled through another rectangular aperture. Their length is fixed to a quarter wavelength at central frequency, and each of them is fed by two microstrip lines [5]. Closed form expressions based on elliptic integrals can then be used to determine the best width for the patches and the aperture, or a numerical optimization can be considered instead.

It was observed a few years later that the rectangular aperture resonates and radiates a relatively large part of the energy, which is a serious limitation of this first attempt. It was then suggested to mitigate this effect by cutting the angles of both the aperture and the patches in order to obtain a hexagonal shape instead [6]. The main merit of this idea was to bring a more general question : what is the best shape for an aperture-coupled directional coupler ?

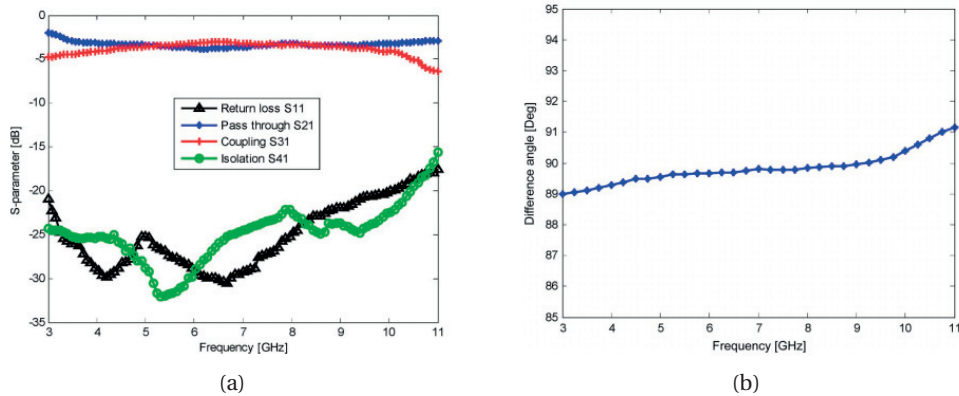
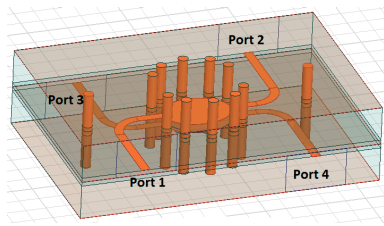


Figure 3.7: S parameters and phase shift for an UWB elliptically-shaped directional coupler. Courtesy of [7].

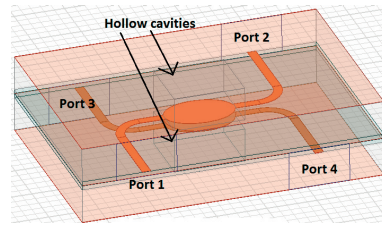
The use of a hexagonal shape is a step towards the solution. In 2007, Abbosh and Bialkowski [7] concluded after trying several solutions that elliptically shaped patches and aperture were giving excellent results, while being very easy to model in nowadays softwares. They also provided closed form expressions to find starting geometrical dimensions for software-based numerical optimization. Finally, an UWB directional coupler working on the 3.1GHz-10.6GHz band was demonstrated 3.7.

In order to adapt this coupler to an operation in our Rx band, two steps were required. First, we had to rescale it and to adapt it to our context -especially, to the substrates we are using-. Our preferred substrate for signal lines is the Rogers RO4003C of thickness 0.203mm, a choice that was justified in the previous section. The modeling and scaling of the coupler was then performed with HFSS.

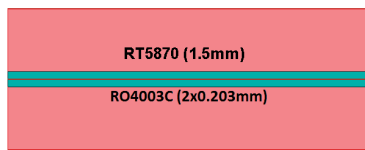
Chapter 3. A first Rx-Band Element



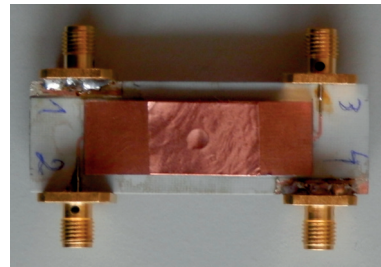
(a) Coupler surrounded by a belt of vias (HFSS model).



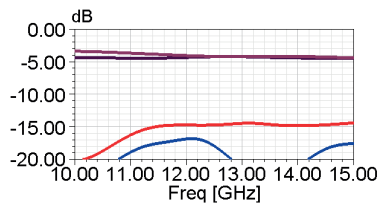
(b) Coupler surrounded by a drilled cavity (HFSS model).



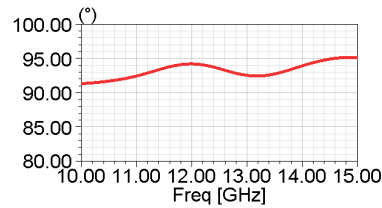
(c) Layer stackup of the stripline coupler.



(d) Photo of the prototype.



(e) Best S parameters obtained for the cavity version (HFSS simulation).



(f) Best phase shift obtained for the cavity version (HFSS simulation).

Figure 3.8: Model, simulations and prototyping of the proposed stripline version of the coupler.

Up to now, this coupler was designed in microstrip technology, but in the end it has to be embedded *inside* the feeding circuits of an antenna array. It means that we had to move from a microstrip to a stripline structure by adding substrates to close the structure, as described in Fig. 3.8c. At this point, an unexpected difficulty appeared; the aperture started to excite the so-called parallel plate waveguide modes (PPWM) which were the source of an important leak of energy inside the substrate. It was also observed that this phenomenon created an amplitude imbalance between the outputs of the coupler, and trying to mitigate this issue by changing the dimensions was not solving the problem at all.

As a solution, increasing the asymmetry of the structure indeed decreases the excitation of PPWM, because the upper and bottom ground planes are put further away from the aperture. But increasing excessively the thickness of the layers is not an ideal solution, because in an antenna feeding system and as will be seen in the next section, the signals have to cross vertically the substrate layers in order to reach the radiating element at some point. A tradeoff

3.2. Choice and modification of a directional coupler

was then found by choosing RT5870 substrates with a thickness of 1.57mm.

The excitation of PPWM was still partially unsolved, and we came with two ideas, depicted respectively in Fig. 3.8a and 3.8b. The first is to surround the aperture with shorting pins that would prevent the energy from leaking. Unfortunately, it turns out in this case that the energy is just reflected back to the coupler, in such a way that the amplitude imbalance and return loss are degraded. The second solution is to drill a cavity around the aperture, which has the same effect as increasing the height of the substrate since it is equivalent to decreasing the permittivity around the aperture.

A prototype was produced to verify the proper operation of the directional coupler. The results were presented in a conference [52], and this coupler is now, in principle, ready to be used with an antenna element as will be done in the next section. As can be seen in Fig. 3.9, the amplitude imbalance between outputs is below 1dB on the Rx and Tx Bands, while the phase shift is maintained around 86° . The other S parameters are below -16dB. The reader may also notice the fact that the purple S parameter curves are closer to -5dB than to the ideally expected value of -3dB. This artifact is due to losses, and we could identify that most of them were located in the connectors that we were using for this prototype.

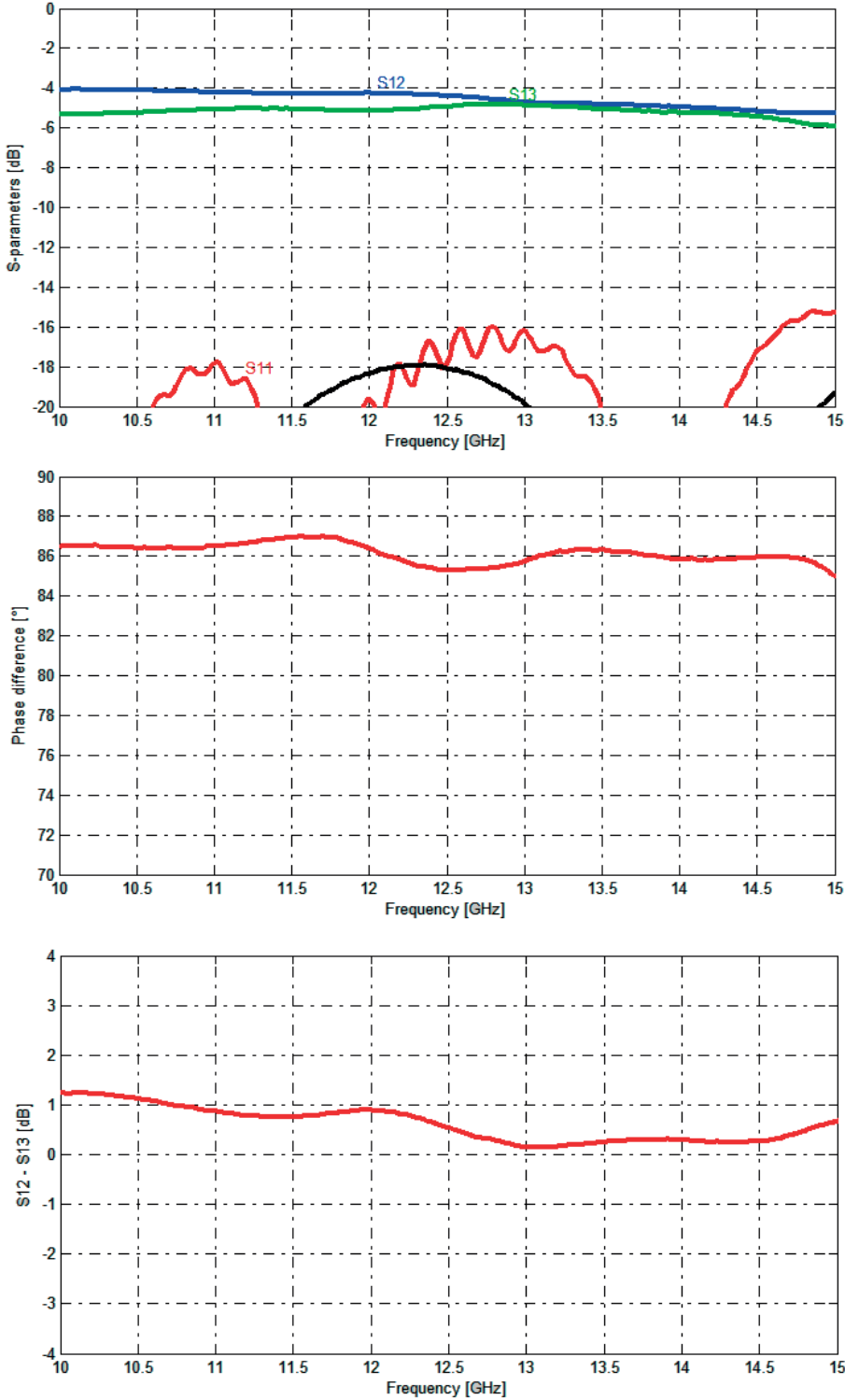


Figure 3.9: Measurements of the coupler prototype (post-processed in Matlab).

3.3 A first complete antenna element

We are now going to merge the results of the previous section and to present a complete antenna element involving stacked patches fed by a wideband directional coupler. The (stripline) coupler is embedded below the patches, and the overall structures already requires many layers that are described in Fig. 3.10 and that make the modeling and manufacturing slightly challenging. Here is a description of the layer stackup and the circuit topology from top to bottom :

- A top patch is etched on a FR4 substrate of 0.1mm and glued to a layer of 2mm of foam. The bottom patch is etched on a RT5870 substrate of 1.57mm of thickness.
- A cross shaped aperture in the ground plane is used to excite the patches. The two orthogonal excitation lines are etched on two layers of RO4003C of 0.203mm of thickness stacked below the ground plane.
- Another layer of RT5870 is placed below to separate the feeding lines from the next ground plane. A belt of shorting pins is placed around the cross shaped aperture in order to prevent PPWM from spreading. The two orthogonal signals are brought down through this layer thanks to a set of vias arranged like a vertical coaxial cable.
- The signals are distributed in two RO4003C signal layers and reach the coupler described in the previous section, before reaching the inputs of the antenna element. A last RT5870 layer is placed below the coupler for the sake of symmetry.

Our second serious attempt to produce a prototype -after the directional coupler of the previous section- was dedicated to this complete antenna element. Unfortunately it was unsuccessful, for at least three reasons. The main one is that the RT5870 substrate is difficult to drill and to metallize, as many Rogers substrates containing PTFE. A specific chemical treatment -that is not available at EPFL- is required unless the metallization may fail randomly for some holes. It happened in our case and we did not know about it before trying.

The second reason, which may have less impact, is that we were not yet using the proper connectors at the moment; we also did not take any precaution to prepare a proper footprint for them. The last reason is a bit more philosophical : we tried to prototype immediately a full element instead of validating each part separately. In general, there are only little chances that such an approach would provide immediately satisfying results.

Finally, this dead end motivated a change of strategy in the development of the thesis. Because the simulated AR quality was much below our requirements anyway, it sounded necessary to start a brand new design that would improve much more this aspect. Also it was a good opportunity to give up the idea of merging the Rx-Band and Tx-Band into a single element, and to consider separate antennas with smaller respective bandwidths. This is particularly

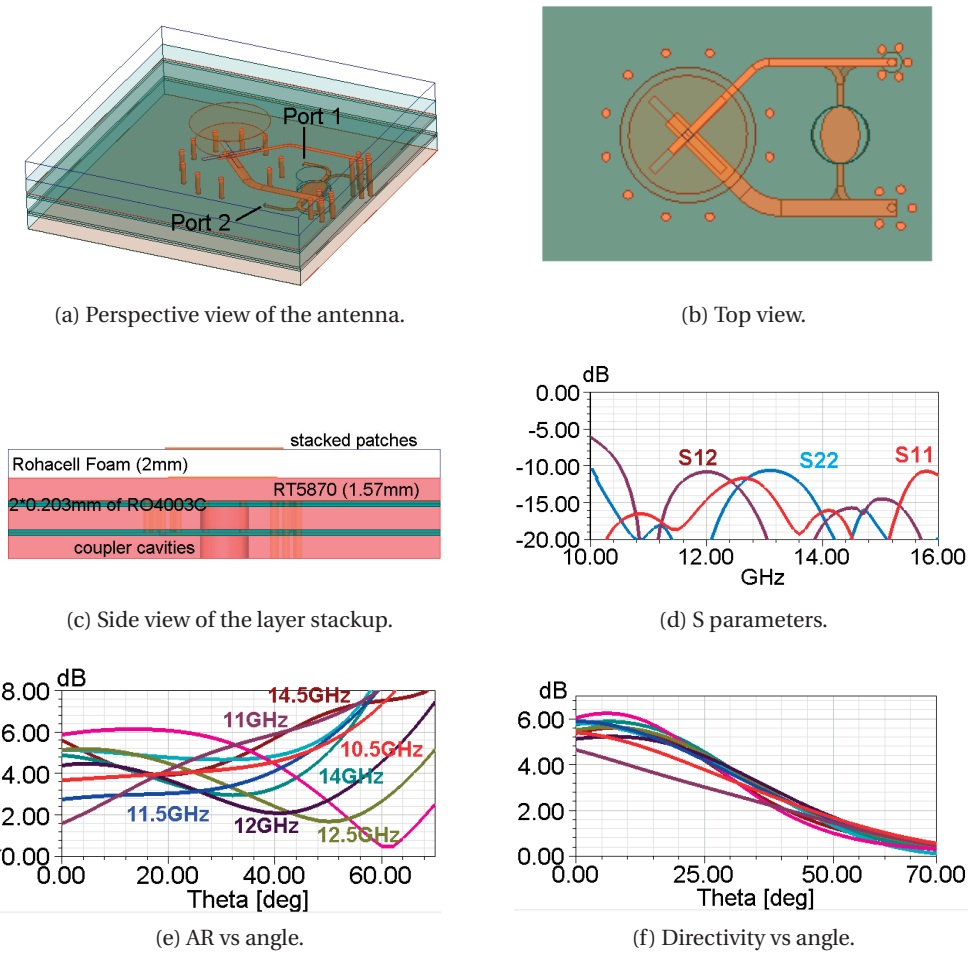


Figure 3.10: HFSS model and simulation results for a complete antenna element.

helpful to ensure much better S parameter results -namely below -15dB or even -20dB- at the expense of the bandwidth itself.

Regarding the prototyping issues, we knew at this point the mistakes that we should not reproduce : the RT5870 had to be removed from the feeding circuits; the connectors had to be changed and improved, and finally the feeding topology of the prototypes had to be simplified by removing both the coupler and the vertical transitions. The next chapter will take into account all these points.

4 Improving the Axial Ratio of a planar array

As far as I see, all a priori statements in Physics have their origin in symmetry.

Hermann Weyl

A top priority for our antenna elements is to be able to handle high-quality dual-circular polarization. By "high-quality" it is not only meant that the Axial Ratio (AR - defined in the previous chapter) should remain below 3dB for both polarizations in the main radiation direction, which is often implicitly assumed in the literature on the topic. It is rather required that the AR remains below 3dB for angles ranging from 0° to 60° and in all azimuthal directions, in order to be able to steer the beam in those directions while keeping an AR as low as possible. In fact, the latter point is less important because the final array is supposed to perform the azimuthal beam steering with a mechanical rotation; in that case optimizing the radiation in a single plane would be enough.

Perfect circular polarization is achieved as soon as the electric field of the radiated wave can be decomposed in the sum of two perpendicular linear polarizations of same amplitude and in phase quadrature. Intuitively, this profile can be described as "highly symmetric". Whenever discrepancies appear in this phase shift or in these amplitudes, the polarization becomes more and more elliptic, or less and less symmetric, as was explained in the previous chapter. And the fundamental point to understand is that these discrepancies stem from the various kinds of asymmetries that exist in antenna elements, or at array level.

The sources of asymmetries are manifold : imperfections in the feeding system -especially the directional coupler-, any geometrical or topological asymmetry in the radiating element itself, or in lesser extent fabrication tolerances. Also, the AR tends to degrade as the radiation direction increases from 0° to higher angles, although it is not systematically true.

In order to mitigate this problem, there is essentially a single existing method available for engineers, that looks natural when it is stated : the asymmetries have to be compensated,

Chapter 4. Improving the Axial Ratio of a planar array

or equivalently the antenna elements or the overall antenna array have to be designed in such a way that is "as symmetric as possible". This principle then divides in two different but non-mutually-exclusive approaches, namely the *sequential feeding* at element level and the *sequential rotations* at array or subarray level. In the first case, the antenna elements are excited with more inputs than usually required to get the desired polarization; the position of the inputs and their phases are chosen in such a way that the elements exhibit an increased overall symmetry. In the second case instead, the same radiating elements are used, but rotated with respect to their neighbors. A phase shift is applied in order to compensate this geometrical rotation.

In the previous chapter, we saw that our first attempts to build an element for the Rx Ku-Band resulted -among other issues- in excessively large AR values. In order to tackle this problem, we suggest here to take the sequential feeding approach as a starting point and to design a new element almost from scratch from this constraint. This chapter is thus divided in five parts. The two first ones are dedicated respectively to the description of the sequential rotations and sequential feeding methods. In the third part, a novel element is proposed and simulated, indeed using the sequential feeding approach but without any feeding system yet. The fourth part explores existing solutions for the phase shifters that could be used to build a proper feeding system, while the last part presents a complete element that is fully simulated, built and measured.

4.1 Sequential rotations in principles

Since their introduction in 1989 [53], sequential rotations in planar antenna arrays have become a classical and almost mandatory improvement technique for polarization quality. A full chapter will be dedicated to this aspect of antenna array design : one indeed cannot think of approaching Dassault Aviations's tight requirements in terms of axial ratio for a wide range of angles with resorting to it.

The rough principle of this method, applied to a very simple linearly polarized element, lies in the following remark, based for instance on situation (b) in Fig. 4.1. The "horizontal" (H) radiation of the upper left element in some direction of interest can be seen as the sum of a Co-polar component and of a (parasitic) Cross-polar component :

$$\vec{E} = \vec{E}_{copol} + \vec{E}_{Xpol} \quad (4.1)$$

It is reasonable to think that the latter is to a large extent caused by the V access (necessary for the "vertical" polarization). If now the upper right element is mirrored such that the V access remains in its position, then the Co-polar component would change its sign while the the Cross-polar one would remain the same. This mirroring can be compensated by a proper phase shift in the excitation, and it yields the following field :

$$\vec{E} = \vec{E}_{copol} - \vec{E}_{Xpol} \quad (4.2)$$

Which, added to the previous field, would tend to cancel out the parasitic component in the far field. Unfortunately and as is often the case in sciences, an elegant method comes with some drawback : because sequential rotations somehow modify the radiation pattern and the position of elements, some unexpected grating lobes appear. This phenomenon was first mentioned in [54] and subsequently discussed in [55].

Numerical methods such as genetic algorithms have been used extensively over the last years to optimize arbitrary positions and phase shifts of radiating elements in antenna arrays; complex constraints and tradeoffs between radiation pattern and polarization quality can be handled in this way. A good example is situation (e) in Fig. 4.1 taken from the NATALIA project [1], in which an array of circular shape had to be optimized for a uniform radiation in all azimuthal directions.

Yet, numerically optimized arrays require complex feeding systems, and most of the time the configurations (a-d) presented in a now classical paper by Woelder and Granholm are enough [8]. They made a complete study of interesting rotations that can be applied to a dual-linearly

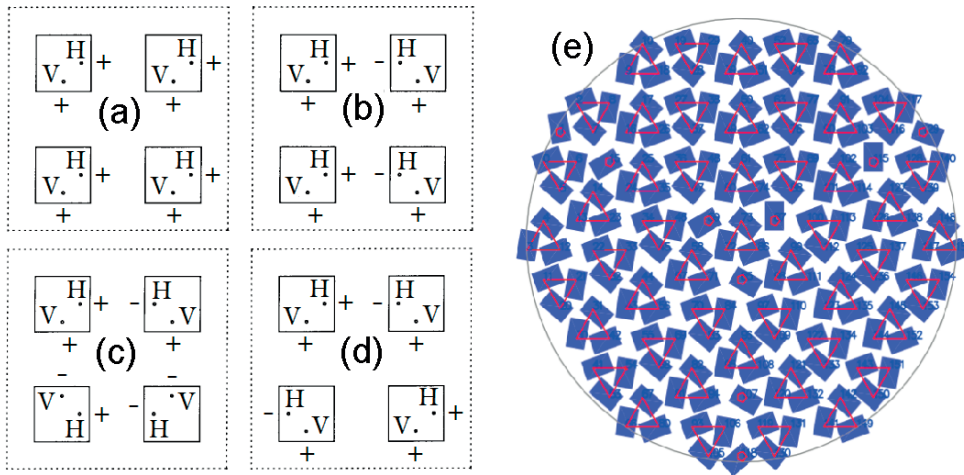


Figure 4.1: Two illustrations of the sequential rotation principle (courtesy of [8] and [1]).

polarized 2x2 array and based only on mirroring operations. These rotation schemes can be applied not only to 2x2 subarrays, but also recursively in various combinations to cover rectangular arrays in general.

This kind of topologies would fit perfectly our requirements, since we are working with a square-shaped array. But all these ideas can be pushed even further, as will be seen in the next section.

4.2 Sequential feeding at element scale

Instead of playing on symmetries at array level to improve the polarization quality, one may think of considering exactly the same idea rather implemented at element level. This approach is referred to as *sequential feeding* and consists in feeding a (dual) circularly polarized element with more access points than necessary together with adequate phase shifted signals. A summary of existing topologies with their advantages and drawbacks is provided in [40]; the easiest and most symmetric is made up of four accesses in phase quadrature (0° , 90° , 180° , 270°).

An early publication around 45 years ago [9] used this method to excite a square-shaped metallic cavity through four pins; the radiation (from 250MHz to 400MHz) occurred through a cross-shaped tapered slot, and ridges were added to extend the bandwidth (see Fig. 4.2). An important point with this pioneer publication is that it deals with dual-circular polarization, and not only with a single circular or a dual-linear one. This is exactly what is required in our context, and it is not obvious at first sight that sequentially-fed structures could handle it. The corresponding excitation topology involves two 180° phase shifters and a directional coupler (see Fig. 4.2); it is further discussed in the next section.

In the last decade there has been an increased interest in sequential feeding when it was applied to the excitation of patch antennas, as witnessed by a series of papers and conferences [10] [56] [57]; thanks to the use of four L-shaped probes, a wideband broadside operation (between 1GHz and 2GHz) was obtained for a single patch [58]. This structure can be seen in Fig. 4.3, together with a first example of phase shifter, the so-called *Schiffman phase shifter* [59]. A series of general remarks can be made now :

- If sequential feeding is applied at element level rather than at array level, the parasitic grating lobes -which are a typical array effect- do not appear.
- The overall array circuitry is simplified when we deal with a set of identical unrotated elements without any rotation, even if each of these elements taken individually is more complex than the original one.
- Theoretically, if the excitations are ideal, all the elements become invariant by rotations of a multiple of 90° ; Applying a subsequent rotation scheme at array level seems then meaningless. Yet there are for sure some asymmetries in practice, and combining element sequential feeding with array sequential rotations remains a possibility for an even better polarization quality. In this case, the previous point is not valid anymore.
- The main drawback of this method is that each radiating element, and not only each subarray, must include a complex circuit made up of power splitters and 180° phase shifters. Fitting all the circuitry in the limited available space becomes a challenge by itself.

Chapter 4. Improving the Axial Ratio of a planar array

Considering the aforementioned points, the next researches are going to focus on the application of the sequential feeding method to planar antenna elements. The latter point is to be taken seriously, and will be covered in the remainder of this chapter.

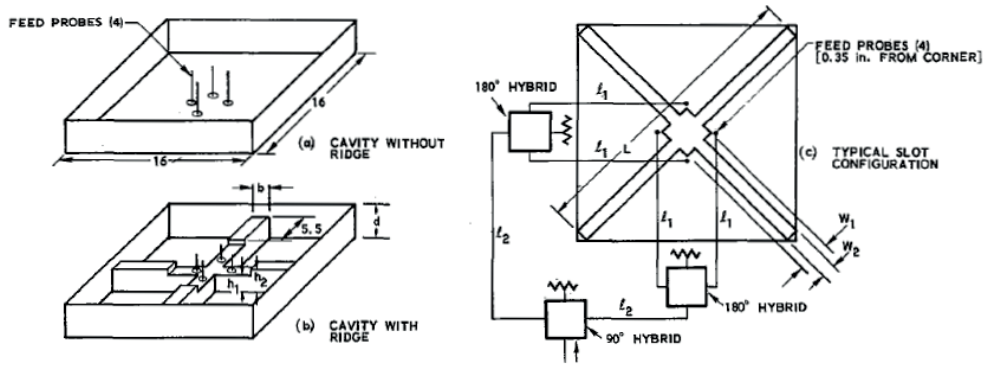


Figure 4.2: Sequentially-fed cavity around 300MHz (early 1970s). Courtesy of [9].

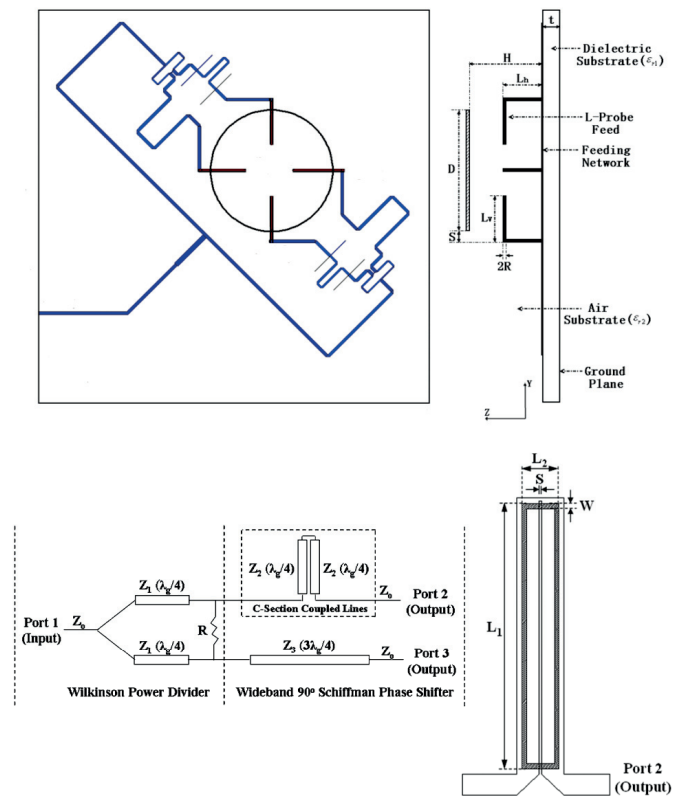
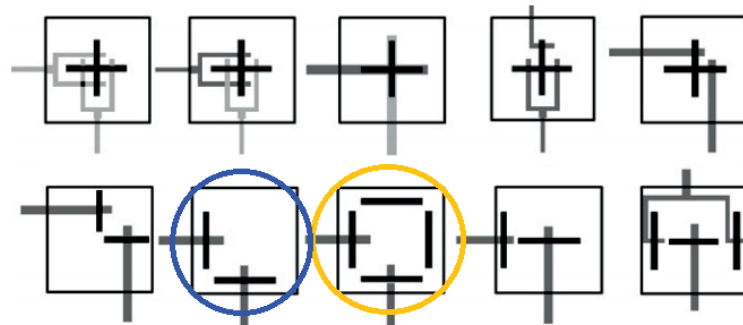


Figure 4.3: Example of a sequentially-fed patch using Schiffman phase shifters (2000s). Courtesy of [10].

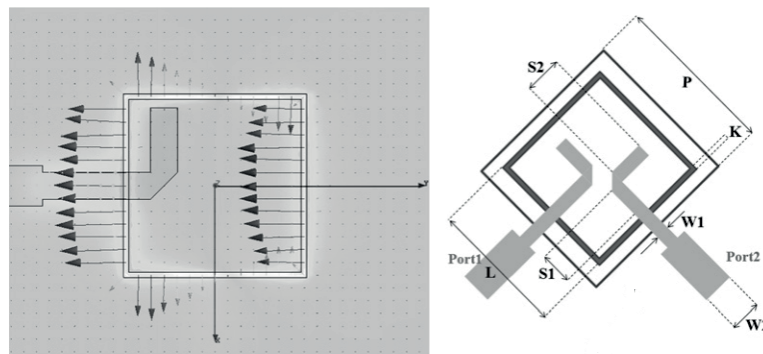
4.3 A novel patch antenna sequentially-fed through a circular slot

We saw in the previous section that sequential feeding is a generic and efficient method to improve circular polarization quality. A question that stems naturally from this remark is whether this excitation scheme can be adapted to aperture-fed antennas, namely the ones that we are the most interested in. Two recent publications by Buffi et al. [11] [12] provide an interesting contribution; they start by making an almost exhaustive list of aperture feeding geometries for dual-linearly microstrip antennas -and thus for circularly polarized ones-.

As a starting point, let's consider the situation marked in blue in Fig. 4.4a. The two linear polarizations are excited through rectangular slots along two edges of a simple square-shaped patch. A rudimentary improvement results in the situation marked in yellow : two dummy slots are added along the remaining edges in order to improve the symmetry of the patch a little bit.



(a) A non-exhaustive list of existing feeding topologies.



(b) A dual-linearly polarized antenna fed through a shared slot.

Figure 4.4: Recent works that inspired the new antenna (courtesy of [11] [12]).

Chapter 4. Improving the Axial Ratio of a planar array

The next natural step brought by Buffy et al. is to merge all the slots in a single one that is shared by the excitations; the patch is then excited along all its edges, as the field profile shows (Fig. 4.4b) and a higher degree of symmetry is reached with a positive impact on the polarization quality. This concept was tested in the WiMAX band -3.3GHz-3.8GHz band, 14% of fractional bandwidth- where the authors developed a small 2x2 array and demonstrated successful results.

Our contribution is now to follow this logical pattern, and to improve the structure even more by exciting it with 4 accesses having the adequate phases. To be more accurate, we are going to consider the structure presented in Fig. 4.5a (side view) :

- Two patches are stacked in a classical way; the bottom substrate was still chosen to be a Rogers RT5870 ($\epsilon_r = 2.33$, thickness 1.57mm) while the upper one is foam. The thickness of 3mm is the result of the later parametric optimization, and was not chosen due to any other particular constraint.
- The uppermost layer (FR4, 0.1mm) is used as a radome on which the upper patch is being etched.
- Two feeding layers (RO4003C, 0.203mm) are reserved for the signal lines. They share a common ground plane in which the aperture is etched. From now, only the bottom layer is required because the full feeding system is not yet added.
- An optional bottom layer can be placed in order to model the feeding layers that would be added below in the context of a complete array. A back ground plane would prevent any backlobe in the radiation pattern; from now, this layer is not necessary in the study.

Seen from the top, the antenna is made up of two *circular* stacked patches, excited through a central annular slot (Fig. 4.5b). Choosing circular shapes rather than square shapes does not change, in principle, the overall operation; but it turned out to give a slightly better impedance bandwidth after both were tried and compared. Moreover, it is believed that a circular shape could involve less mutual coupling with neighboring elements in an array, because the surface occupied by a circular patch of diameter d -corresponding to some operation frequency- is obviously less than the surface of a square of same side.

The four orthogonal accesses have to be fed, as can be seen on the left half of the drawing, with respectively 0° , 90° , 180° and 270° signals of same amplitude in order to produce the first circular polarization; in this case it is the left-handed one (LHCP). On the right part, a second configuration produces the right-handed circular polarization (RHCP). In order to switch from one configuration to the other, the excitations marked **1** and **3** have to remain invariant, while **2** and **4** have to be swapped. It is equivalent to adding 180° to this pair of excitations, and that's why they are marked as outputs of a directionnal coupler. At this point, the reader may have a look at Fig. 4.2 in the previous section to see another view of this kind of topology.

4.3. A novel patch antenna sequentially-fed through a circular slot

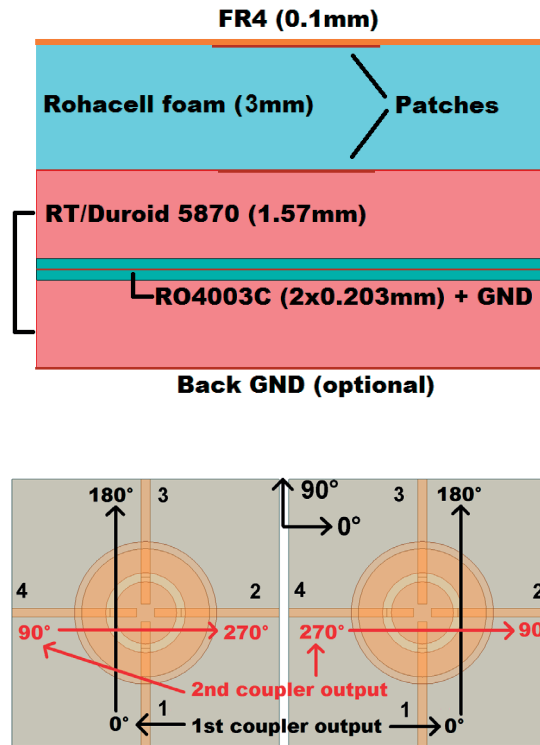


Figure 4.5: Layer view and Top view of the proposed structure.

Now a few words about the practical consequences of this structure. A first obvious property of this structure is that both circular polarizations must give exactly the same radiation pattern if all excitations are ideal, which is always a good point. A second fundamental property, valid for any kind of sequentially-fed radiating element, is that their S parameters are not really meaningful by themselves. Since all the ports are excited at the time in order to produce a circular polarization altogether, the important question is neither *"How much energy is reflected from this port when I feed it while the other are matched?"* nor *"How much energy is coupled from this port to its neighbors?"* but rather a superposition of those questions : *"How much energy is flowing back in port -say- 1 when all ports are excited with the proper signals?"*.

The resulting function of frequency, called the *active S parameter*, is defined with a simple linear combination :

$$S_{Active} = S_{11} \pm j * S_{12} \mp j * S_{14} - S_{13}$$

Chapter 4. Improving the Axial Ratio of a planar array

Table 4.1: Best values found for the ideal sequentially-fed antenna.

parameter	value	unit
50Ω input line width	0.45	mm
Aperture radius	2	mm
Stub lengths	1.3	mm
Aperture width	0.5	mm
Top patch radius	4.2	mm
Bottom patch radius	3.6	mm
Foam thickness	3	mm

The alternate signs corresponding to both circular polarizations. When accesses **2** and **4** are fed out-of-phase, $S_{12} = -S_{14}$ and the expression simply reduces to :

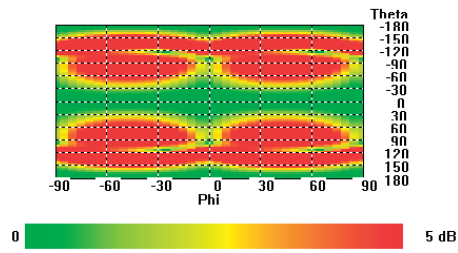
$$S_{Active} = S_{11} - S_{13}$$

Which depends neither on the polarization, nor on the port considered. There is thus a single Active S parameter to minimise in order to guarantee a proper matching. Taking all these facts into account, a careful parametric numerical optimization has been performed on the geometrical values of the proposed antenna element (Fig. 4.5b), using CST Microwave Studio and resulting in table 4.1. In Fig. 4.6 the radiation pattern, the active S parameter and the axial ratio at extremal frequencies are reported, and they lead to the following comments :

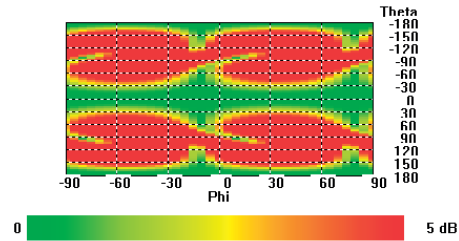
- A broadside radiation pattern is obtained, with a monotonic behaviour, a good azimuthal symmetry and a strong stability in frequency. The maximal value of 8dBi is higher than the ideal 5-6dBi, but there are few chances to achieve a better value.
- The axial ratio in the cut plane $\phi=0^\circ$ is kept for almost all angles and frequencies below 3dB. The 2D plot reveals that there is not an ideal azimuthal symmetry in the AR profile; but things will change in the context of an array due to the presence of neighbors, so no conclusion can be made from now.
- The active S parameter is maintained below -20dB on the 10.7GHz-12.7GHz band, and below -15dB if frequencies up to the Tx band (14GHz-14.5GHz) are being considered.

With the aforementioned points fulfilled, this element is a serious candidate for our purposes, provided that a proper feeding circuit can be designed; and this, as will be discussed over the next sections, is not a trivial part at all.

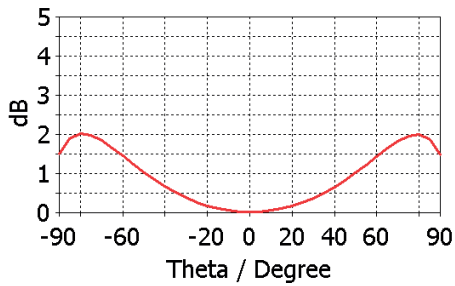
4.3. A novel patch antenna sequentially-fed through a circular slot



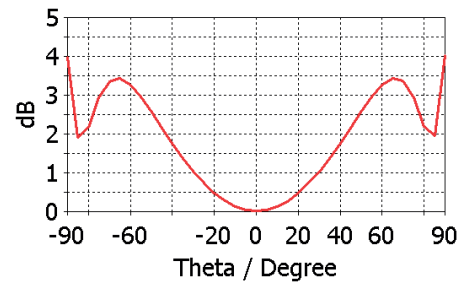
(a) 2D Axial Ratio at 10.7GHz.



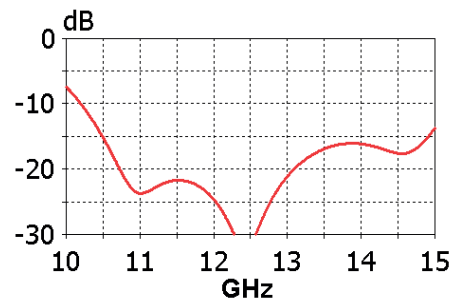
(b) 2D Axial Ratio at 12.7GHz.



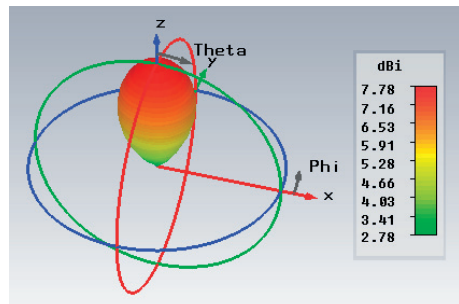
(c) Axial Ratio cut - $\phi=0^\circ$ 10.7GHz-.



(d) Axial Ratio cut - $\phi=0^\circ$ 12.7GHz-.



(e) Active S parameter.



(f) 3D Radiation pattern (for any frequency).

Figure 4.6: Results for the sequentially-fed stacked patches.

4.4 Design of a feeding system for the antenna

4.4.1 A survey of existing phase shifter topologies

In order to apply sequential feeding to a dual-circularly polarized element, one needs to be able to split both input signals and to apply a 180° phase shift between the resulting excitations. This results in a list of tight constraints for the phase shifters to be used :

- They should consist of single-layer microstrip structure for an easy integration in the overall array.
- The bandwidth (in terms of impedance matching as well as phase shift) has to reach 20% in order to cover the Rx band.
- The fabrication tolerances should not be excessively sensitive (this requirement is quite generic through this thesis).
- Compactness is an important factor; if two phase shifters are required for each element, in addition to the place taken by the excitation slot and the rest of the lines, space clearly becomes an issue. Each element must fit a square which side is a little bit more than a half wavelength in vacuum.

The latter constraint may be addressed in a different way : if the power splitters and phase shifters are shared among a subarray of elements -namely a full line- then their size should not be a problem anymore. But it turns out that the distribution system for a line has to carry four different signals (0° - 90° - 180° - 270°) to all the elements instead of only two (0° - 90°); such an increased complexity mitigates the advantages of this approach.

A lot of time has been spent looking through the literature for a suitable phase shifter. Various solutions are presented in Fig. 4.7 and the following comments can be made on them :

Solution 1 : The *radial stub* structure [60] is at first sight a quite eldritch but easy-to-manufacture structure that can create a 90° phase shift. Its original operation is UWB (3.1GHz-10.6GHz), which would be much more than enough. Unfortunately, two of them should be cascaded in order to achieve a 180° phase shift, and since the dimensions are of the order of a quarter wavelength, the size would immediately become prohibitive.

4.4. Design of a feeding system for the antenna

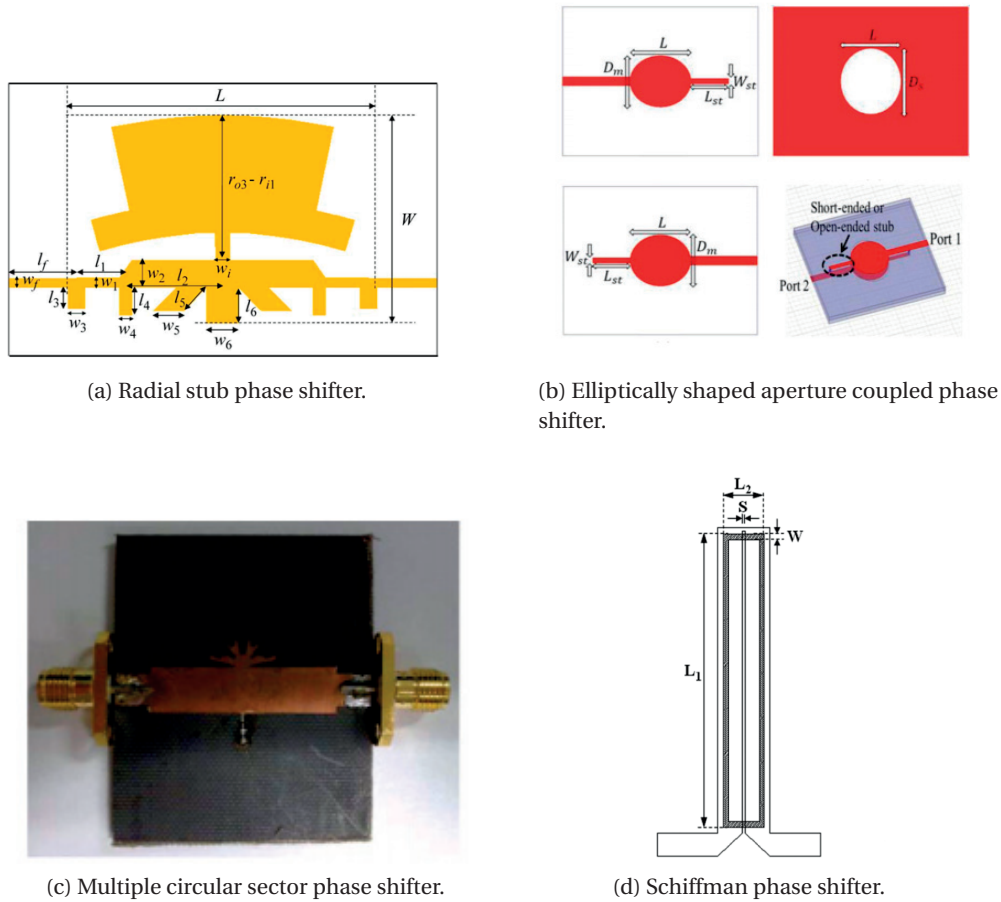


Figure 4.7: A non-exhaustive list of existing phase shifters.

Solution 2 : The *elliptically shaped aperture-coupled* phase shifter [61] [62] is based exactly on the same idea as the coupler that was studied in a previous chapter : two patches are being coupled through an elliptical aperture and fed with four symmetrical inputs/outputs. But in the case of a phase shifter, two accesses are necessary and sufficient in order to apply a phase shift (with respect to some *reference line* carrying a *reference signal*, not represented on the drawing). The other accesses are finished with two identical matching stubs. Their dimensions, together with the dimensions of the ellipses, provide many degrees of freedom for an optimization. The main drawback is that this coupler is not a single layer one, and thus placing it below a radiating element doesn't seem possible at all.

Solution 3 : The *multiple circular sector* phase shifter [63] is made up of a collection of tiny parasitic stubs that are placed along a microstrip line. Their sizes and positions have to be carefully optimized with a genetic algorithm. This solution was rejected because of the very small size that these stubs should have once rescaled in Ku-band, but also because of the time that would be needed to study such a structure and the related algorithms by themselves.

Chapter 4. Improving the Axial Ratio of a planar array

Solution 4 : The *Schiffman* phase shifter [59] introduced in 1958 remains a classical solution for achieving 90° phase shifts. It mainly consists in a bended quarter-wavelength line with a very sharp gap to couple energy along the signal path. Here again, the sensitivity of this gap and the overall size of two cascaded structures led us to reject this solution without much hesitation.

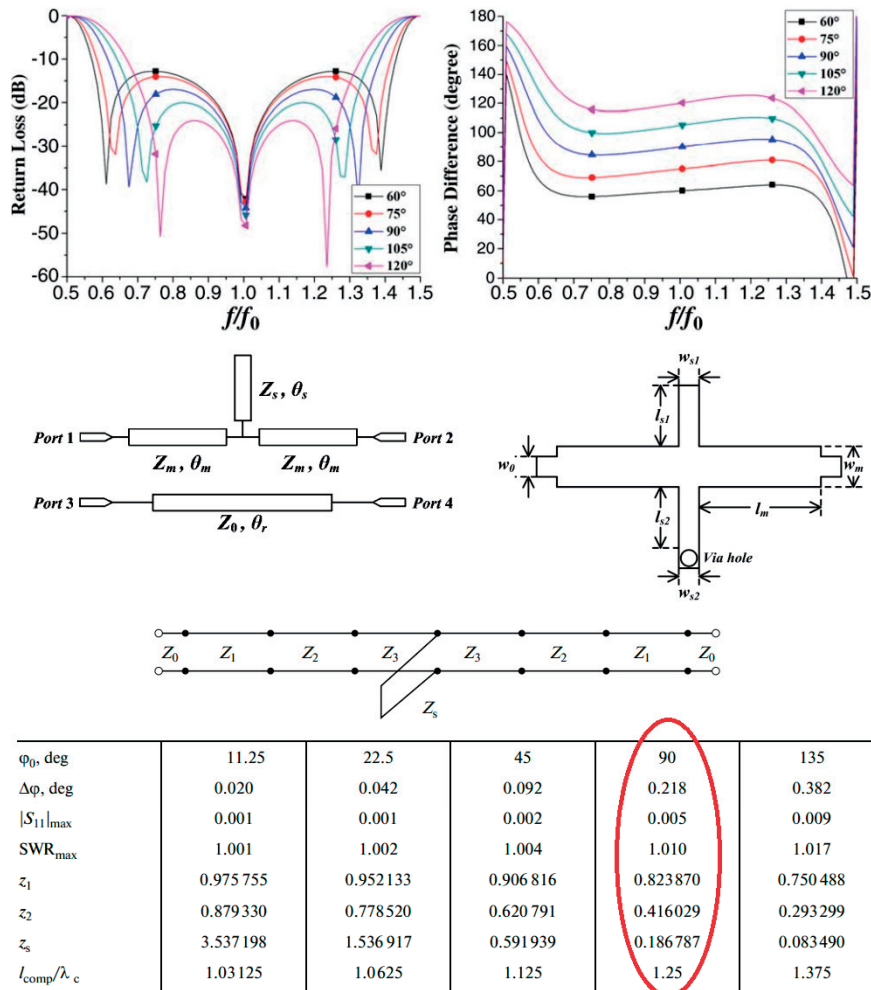


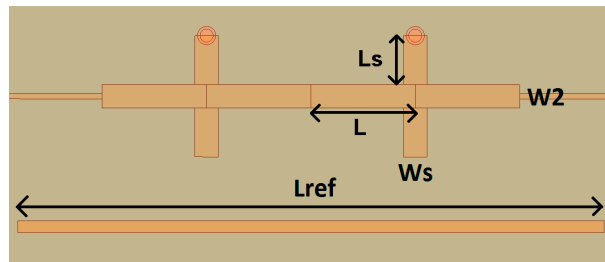
Figure 4.8: Description of a microstrip phase shifter made up of only elementary matching sections and stubs (courtesy of [13]).

4.4. Design of a feeding system for the antenna

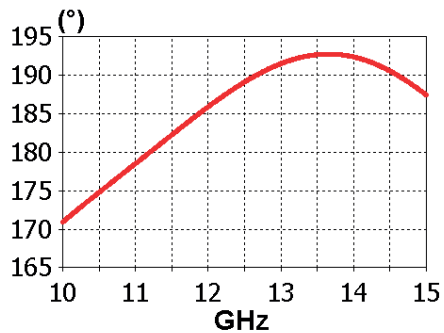
A promising solution depicted in Fig. 4.8 consists in a couple of $\frac{\lambda}{8}$ stubs surrounded by stepped impedance quarter-wavelength matching sections. It is described in [13], [64] and [65], and it can provide an increasingly wide bandwidth (beyond 40%) as the number of matching sections is increased.

This structure was studied essentially from a numerical point of view, in order to provide tables for various phase shifts. A limit to the use of this structure is that the bandwidth decreases as the phase shift increases. Our proposal to obtain a 180° phase shift while keeping reasonable size and bandwidth is to stick together two 90° phase shifters, as was done in Fig. 4.9; each of them is chosen to have a single couple of quarter-wavelength matching sections.

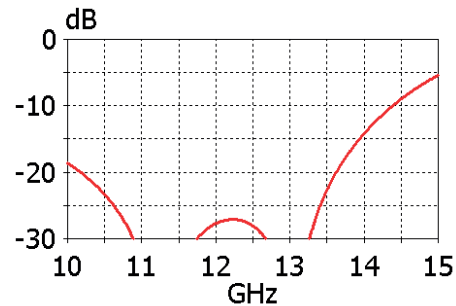
Starting from the values provided in [13], a first rescale could be done, followed by a global parametric optimization of the structure. The values provided in table 4.2 correspond to the results in Fig. 4.9 : a matching much below -20dB is obtained on the Rx band (10.7GHz-12.7GHz) together with a phase shift ranging from 175° to 190° . The plots were extended to include the Tx band in case it could be included in the same element, but the impedance matching seriously degrades as the frequency increases.



(a) Top view of the 180° phase shifter (CST).



(b) Phase shift vs Frequency.



(c) Impedance matching.

Figure 4.9: Simulation of the retained 180° phase shifter.

A complete feeding system has been designed with this phase shifter in order to demonstrate the excitation of the sequentially-fed antenna presented previously. This complete antenna has been simulated and presented in a conference paper (LAPC 2014) available for the interested reader [66], but we will only comment briefly on the results here. First, the overall feeding

Chapter 4. Improving the Axial Ratio of a planar array

Table 4.2: Phase shifter dimension values.

parameter	value	unit
100 Ω input line width	0.2	mm
Reference line length	20	mm
Stub lengths L_s	2	mm
Stub width W_s	0.7	mm
Matching line width W_2	0.7	mm
Matching line length L	4	mm

structure remained much too large to fit in an elementary array cell, and there was no obvious way to mitigate this issue. Then, the AR and radiation pattern qualities were at the same time quite unstable in frequency and degraded compared to our expectations.

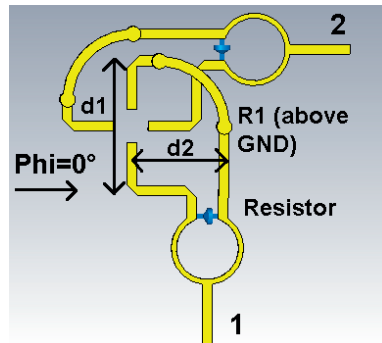
It turned out that the reason for these troubles was the lack of isolation between the four antenna accesses; we indeed simply used T-junctions -appreciated for their compactness- to split the signals between the different excitations, which did not ensure any isolation at all. Moreover, the presence of several bends in the circuit induced small reflections and contributed to the degradation of the AR. Here again, there was no direct and obvious way to mitigate this phenomenon.

In the end, it was not rewarding to spend too much time trying to achieve the best phase shift possible, because it is in fact not a priority. Both the compactness of the circuit and the isolation between antenna excitations shall be considered instead of uttermost importance. In the next section, we will thus adopt a much more classical and robust solution to ensure that these constraints are fulfilled correctly.

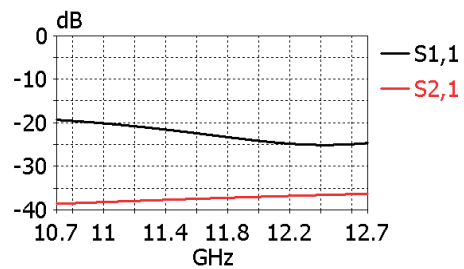
4.4.2 A simpler and more compact solution using Wilkinson splitters

It appeared in the last sections that any feeding system solution based on T junctions and complex phase shifter topologies would systematically fail due to two phenomena. First, fitting two phase shifters per element is impossible due to their relatively large size. Secondly, the use of simple T junctions as power splitters doesn't isolate the outputs from each other and doesn't optimize the return loss in any way. Due to all the small reflections that occur on the way to the element (especially around bends), the overall operation of the circuit then turns out to degrade quickly.

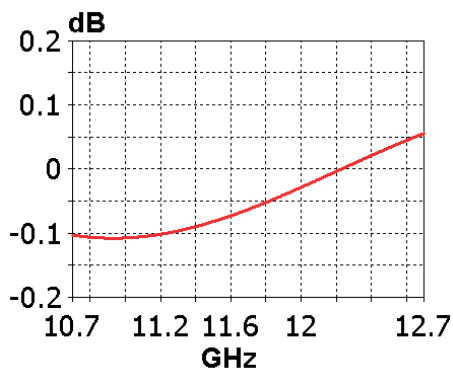
The solution proposed here is rather simple and classical; it consists in replacing phase shifters with simple microstrip delay lines, and T junctions with complete Wilkinson structures, which remain nowadays the best solution for splitting power equally between two outputs in a clean way.



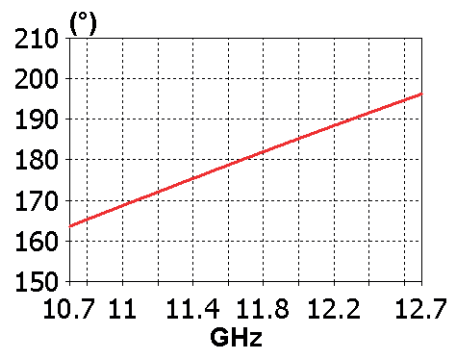
(a) Feeding system topology.



(b) S parameters.



(c) amplitude imbalance between two outputs.



(d) Phase shift between two outputs.

Figure 4.10: Feeding system using Wilkinson splitters.

Chapter 4. Improving the Axial Ratio of a planar array

The new simplified feeding system can be seen in Fig. 4.10 in top view, the ground plane being transparent. Two orthogonal input signals are split through circular wilkinson structures (their 100Ω resistors are depicted in blue) and their pairs of 50Ω outputs excite opposite sides of the central slot (not depicted here).

A complete study of Wilkinson structures is provided in the classical book of Pozar [45]; we just recall briefly a few facts about them. They are made up of two quarter wavelength lines of impedance being approximately 71Ω - 72Ω ; this value ensures a correct matching from the input point of view, on bandwidths up to 20% or even a little bit more. Then, regarding the reflections that may occur beyond both outputs, their decomposition in the sum of an odd mode and an even mode is more suitable for the study. The former will be coupled back to the input and would unfortunately contribute to degrading the overall return loss; but the latter will be absorbed by the resistor, and in any case the outputs will be isolated from each other. This was the main pursued purpose : a lack of isolation was the main cause of amplitude and/or phase imbalances that spoiled the radiation quality in the previous sections, and even though Wilkinsons take a little bit of space and require lumped elements, this effort is really necessary.

Coming back to the circuit at a more global scale, it is impossible from a topological point of view to prevent at least one crossover to appear. In order to circumvent it, the signal is brought up to the upper layer -above the ground plane- through a signal via and follows a quarter of circular arc (of radius R_1 marked on the picture) before being brought back to the bottom layer for the excitation. This pattern is applied to both circuits for the sake of maintaining a high level of symmetry, although only one crossover has to be avoided.

One could be concerned about the fact that bringing the signal to the upper side of the ground plane, close to the patches, could create some parasitic effects. In practice, when the antenna was added to the simulation, this proximity turned out to be harmless from any point of view. Several other solutions have been considered, but eliminated after intensive trials. For the sake of simplicity we will describe from now on only the final retained solution even though a considerable effort was spent in the study of other apparently promising topologies that unfortunately resulted in dead ends.

An additionnal and classical trick has been used in order to mitigate small reflections at bends: mitered bends (or cut bends) also mentioned in [45] have been designed; it remains a second order optimization, but still worth implementing.

4.4. Design of a feeding system for the antenna

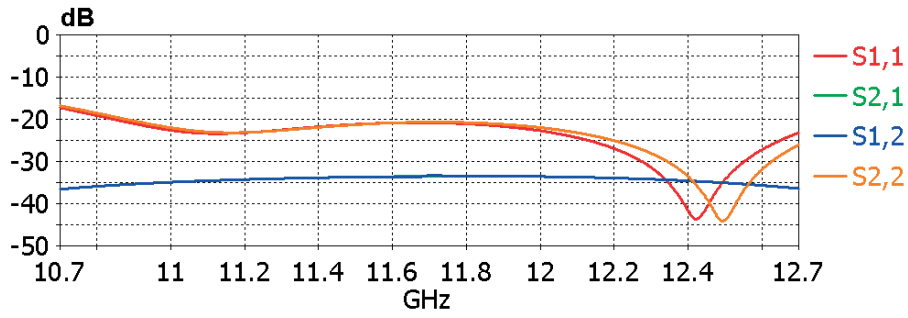
Finally, an overall parametric study led to the fully satisfactory results showed in Fig. 4.10 (see table 4.3 for the corresponding geometrical values) :

- A return loss of -20dB is expected on the whole Rx band (equal for both inputs).
- The amplitude imbalance is maintained at a negligible value (0.1dB at most).
- The isolation between both ports is very high at this point, but not yet so meaningful because no antenna element is excited.
- The phase shift profile is linear around 180° with a maximal discrepancy of 15° at both extremities of the Rx band. It is not much compared to the 10° obtained earlier with a much more complex structure, while the benefits of simplifying the circuit are obvious.

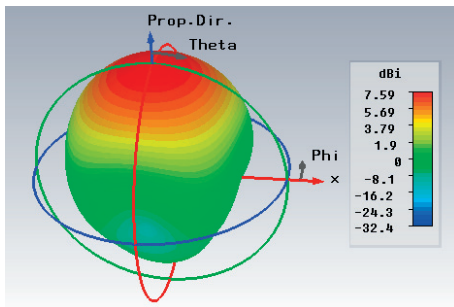
The next step is to go towards the complete element. The aperture, the matching stub and both patches were added, and a parametric optimization was launched on the remaining geometrical parameters (still in table 4.3). The results are depicted in Fig. 4.11 and 4.12 :

- A return loss of -20dB is obtained on the whole Rx band, with very similar profiles for both ports.
- The broadside radiation pattern (reported at central frequency) is very symmetrical, and the directivity is around 7.5dB. Its profile is very stable in frequency.
- The axial ratio (reported for $\phi = 0^\circ$, as defined in Fig. 4.10) is kept below 3dB up to 60° , except for extreme values of angles and frequencies.
- The isolation between both inputs is kept below -30dB on the whole band, which is a strong point of this element. There are two reasons for it; first, as was mentioned in section 4.3, the coupling between a pair of opposite excitations and their two neighbors theoretically vanishes in the active S parameter, because their "contributions" are out-of-phase and of same amplitude. But in case a small coupling exists anyway -due to imperfections in phase and/or amplitude distribution- a phase shift of 180° is applied in one of the branches before reaching the Wilkinson : this results in an odd mode which is absorbed by the resistor instead of contributing to S12.

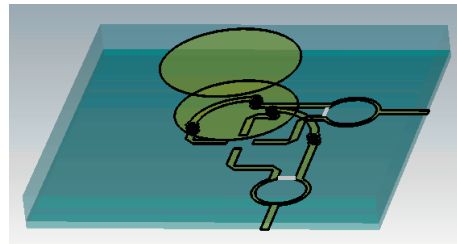
All the aforementioned properties fulfill the expectations of Dassault Aviation for a single isolated element.



(a) S parameters for the complete antenna.



(b) 3D radiation pattern (typical).



(c) Overview of the element.

Figure 4.11: Simulation of the proposed antenna element (CST).

Table 4.3: Dimensions for the antenna element and its feeding system.

parameter	value	unit
Length of the matching stub	1.25	mm
Aperture radius	2	mm
Aperture width	0.5	mm
Upper patch radius	3.95	mm
Bottom patch radius	3.45	mm
Thickness of RT5870 substrate	1.57	mm
Thickness of foam	3	mm
Length d1	5.5	mm
Length d2	3.5	mm
Circular line radius R1	3	mm
Wilkinson radius	1.55	mm
Wilkinson line width	0.23	mm
Resistor gap	1	mm
50Ω lines width	0.45	mm
Mitered bends length	0.55	mm
Metallized holes diameter	0.4	mm
Metallized holes pads	150	um
GND radius around vias	0.5	um

4.4. Design of a feeding system for the antenna

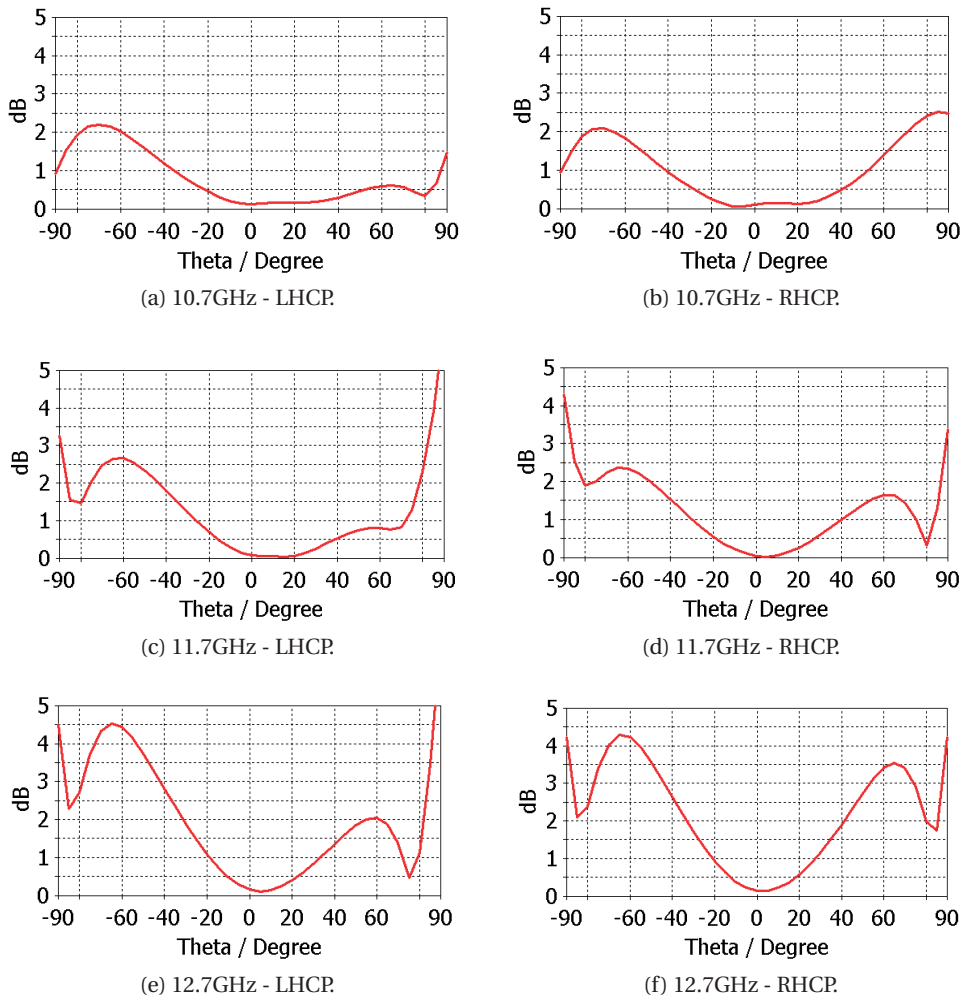


Figure 4.12: Simulated Axial Ratio results for $\phi = 0$ (CST).

Chapter 4. Improving the Axial Ratio of a planar array

The last step to get a conclusive validation of this novel topology is the manufacturing and characterization of a prototype. The different PCB layers produced in our workshop are visible in Fig. 4.13. The largest layer on the left corresponds to the "bottom part" of the feeding system, involving the feeding lines, the connector footprints and the Wilkinson circuits; the ground plane with the central slot are on the other side of the layer, not visible here. The two patches on the right are respectively the bottom one, etched on the "dark" RT/Duroid 5870 substrate, and the top one etched on a thin layer of FR4 (0.1mm). The foam layer that goes glued between them is not shown here. The last layer is the "upper part" of the signal made up of the two circular crossover microstrip lines.

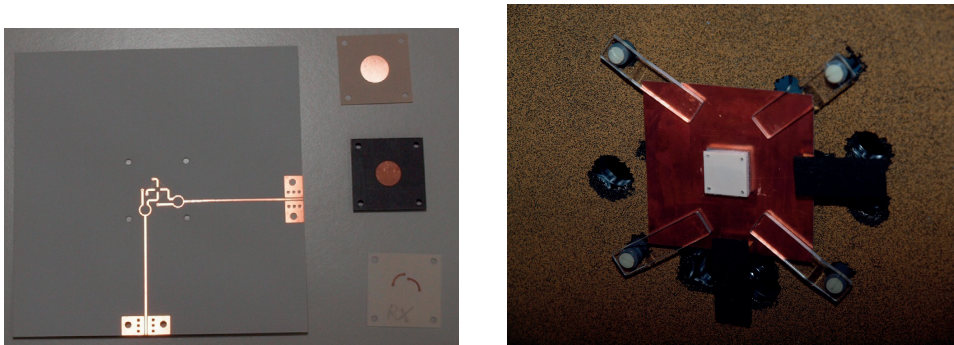


Figure 4.13: Photo of the PCB layers for the prototype and measurement setup in anechoic chamber.

The size of the first layer was chosen to be 8x8mm, while the others were kept as 2x2mm squares just as they are in simulations. This extension of the ground plane was not only motivated by practical reasons (it is more practical to handle and to fit a larger antenna on the measurement setup) but also by the fact that it is safer to keep connectors more than a wavelength away from the center of the element. In a previous prototype, the connectors were indeed much closer to the antenna, and both the AR and the Radiation Pattern qualities turned out to be at the same time lower than expected and quite asymmetric. This perturbation was attributed to the influence of the connectors, and as can be seen in Fig. 4.13 we covered them with two pieces of absorber for the measurement. These precautions had a very positive impact on the measurements of the final prototype.

The measured S parameters are reported in Fig. 4.14a. The return loss is below -15dB for most frequencies and for both ports. This is slightly above the simulated results, though still quite good and fully acceptable; moreover, the isolation between both ports is kept below -30dB as expected.

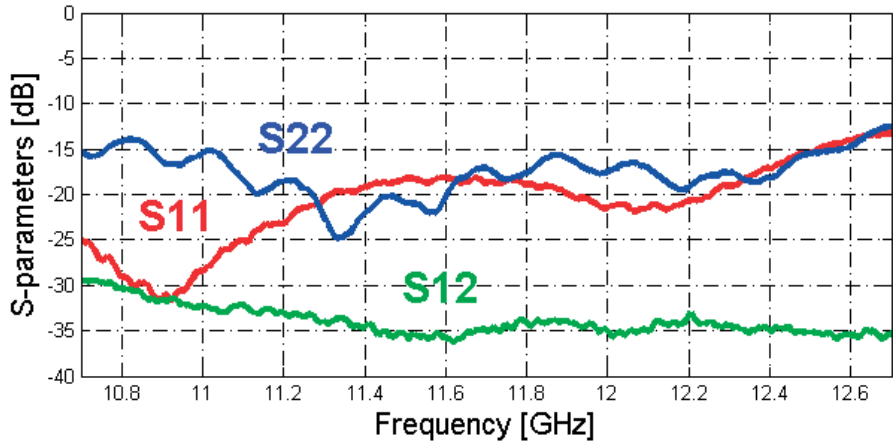
Regarding the measurement of the radiated fields, a linearly polarized horn antenna was used to characterize the linear polarization obtained by exciting each port. Then a simple post-processing in Matlab allows to retrieve the circular polarization characteristics of the antenna. The measurements were performed for the radiation plane $\phi = 0^\circ$ (following the

4.4. Design of a feeding system for the antenna

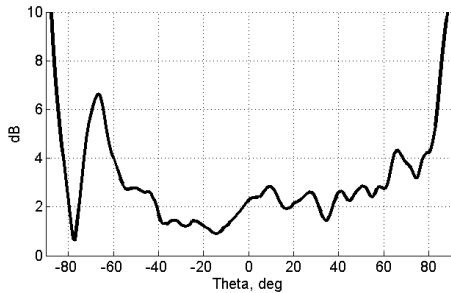
definition given in Fig. 4.10a) but also for its orthogonal plane $\phi = 90^\circ$. As expected the results are very similar and only the ones for the first plane will be commented here, and compared with the AR simulations (Fig. 4.12).

The LHCP/RHCP AR plots are provided in Fig. 4.14 at both central and extremal frequencies. It is apparent that for angles up to $\pm 40^\circ$, AR values are kept below 3dB, and below 6dB up to $\pm 60^\circ$ with seldomly any exception. The radiation patterns are reported in Fig. 4.15 still for central and extremal frequencies. They exhibit quite symmetric and monotonous profiles; the gain versus frequency plots also show its stability, with values between 5dBi and 6dBi most of the time.

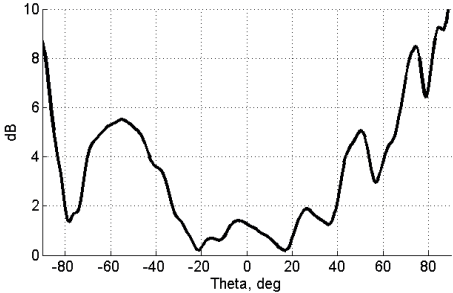
The results of this measurement campaign are overall fully satisfactory, and the design and manufacturing of an isolated Rx-Band element respecting our requirements can be considered a success. Yet the level of sophistication in the in-house manufacturing was quite low. One should keep in mind that this prototype was assembled manually with a general purpose glue and alignment pins; the soldering of the resistors with the help of a microscope was also particularly delicate, and it is still unclear whether the etching precision provided by our workshop was enough for the branches of the Wilkinson circuits. Indeed, the width of these branches was theoretically of 0.2mm, and it is a sensitive parameter. All these unknowns can explain any discrepancies observed between the simulated and measured values, and definite improvements in the quality and repeatability of the results should be obtained with a more professional manufacturing.



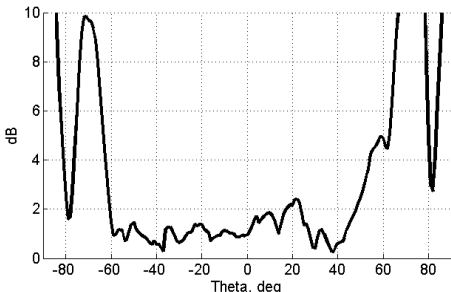
(a) Measured S parameters.



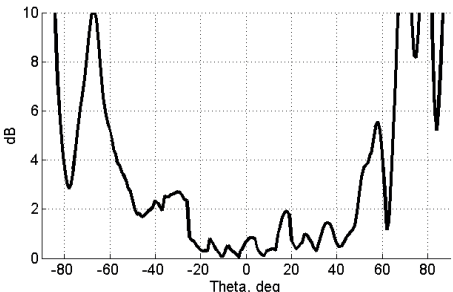
(b) 10.7GHz - LHCP.



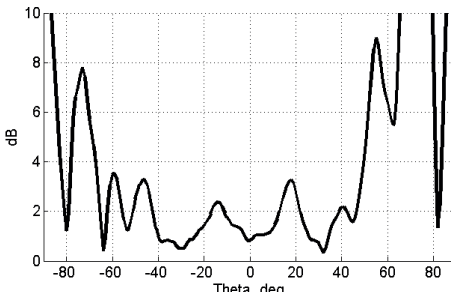
(c) 10.7GHz - RHCP.



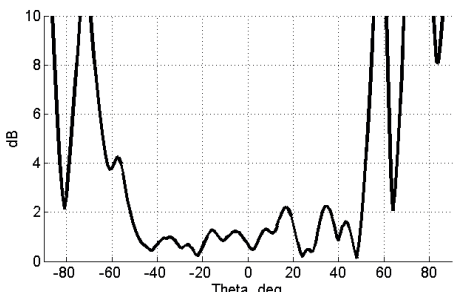
(d) 11.7GHz - LHCP.



(e) 11.7GHz - RHCP.



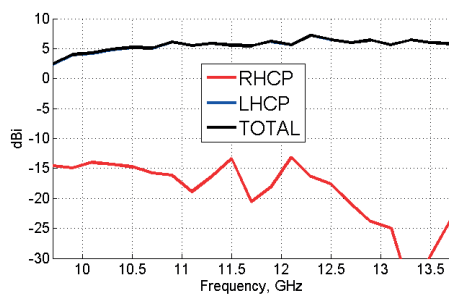
(f) 12.7GHz - LHCP.



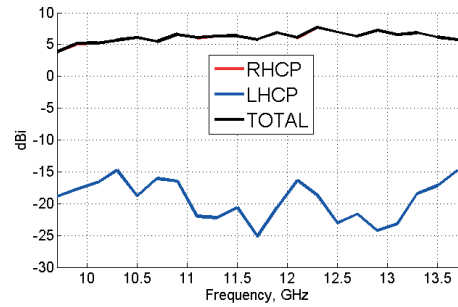
(g) 12.7GHz - RHCP.

Figure 4.14: Measured S parameters and Axial Ratio results for $\phi = 0^\circ$.

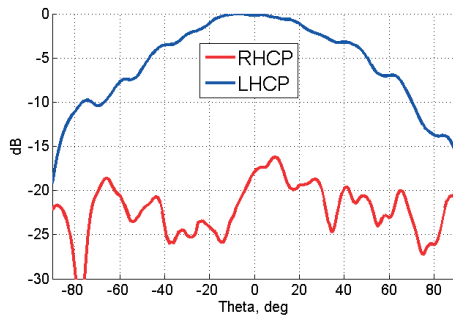
4.4. Design of a feeding system for the antenna



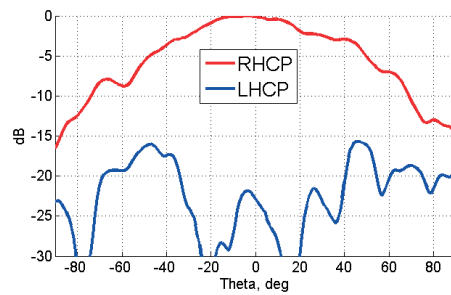
(a) LHCP antenna gain vs frequency.



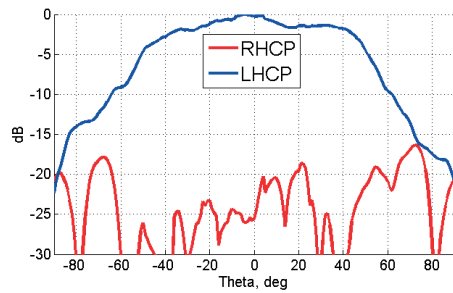
(b) RHCP antenna gain vs frequency.



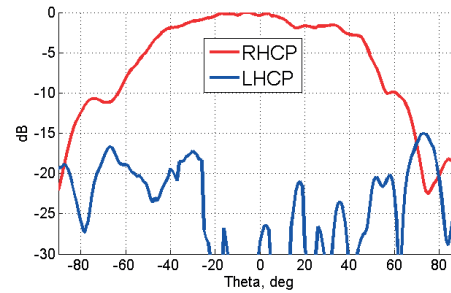
(c) 10.7GHz - LHCP.



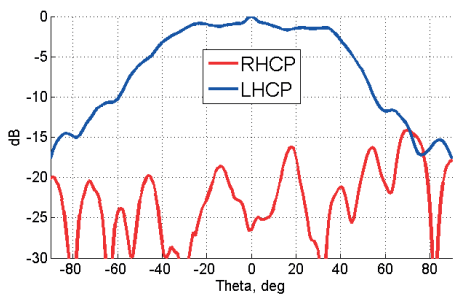
(d) 10.7GHz - RHCP.



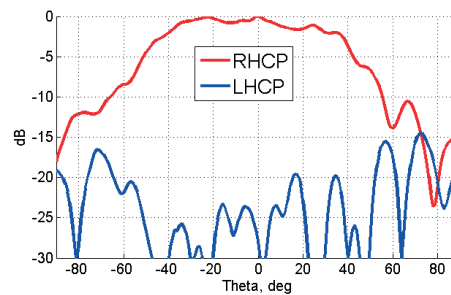
(e) 11.7GHz - LHCP.



(f) 11.7GHz - RHCP.



(g) 12.7GHz - LHCP.



(h) 12.7GHz - RHCP.

Figure 4.15: Prototype photos and measured Radiation Pattern for $\phi = 0^\circ$.

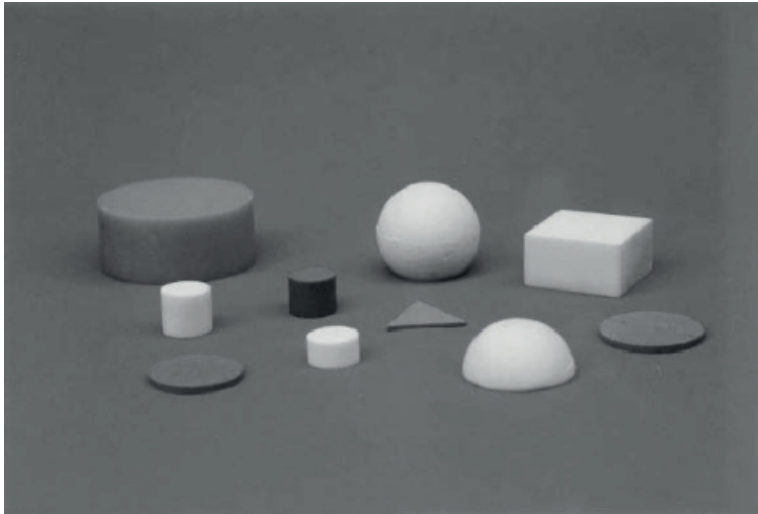
5 Dielectric Resonator Antennas (DRA)

5.1 Generalities on DRAs

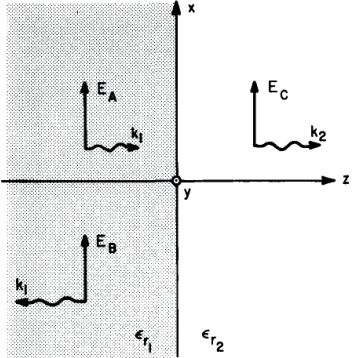
The term *Dielectric Resonator* refers in general to a piece of high permittivity substrate, manufactured with a specific shape and included into a microwave system. Their history dates back to the 1970s, when Van Bladel published an analytical study of a dielectric hemisphere on an infinite ground plane [67]. Because of the high permittivity of the dielectric considered (which ranges typically from $\epsilon_r = 8$ to $\epsilon_r = 100$ in the literature), electromagnetic modes can be excited and confined inside them, hence the name "Resonator". An overview of existing shapes is visible in Fig. 5.1a.

Originally, this technology was used for high selectivity filtering purposes, and the first and only book published until now was covering a lot of theoretical models and practical applications as early as 1986 [68]. It especially provides a classification of the modes for the two most common shapes -rectangular and cylindrical dielectric resonator- which look like their counterparts for classical metallic cavities; the mathematical models used to derive their expressions are due to Marcatili and Cohn.

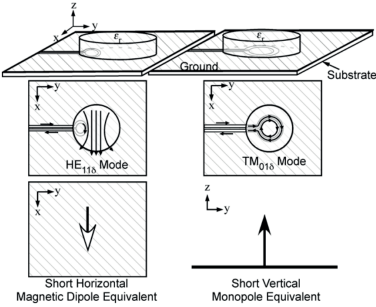
A couple of papers by Long et al. in 1983-1984 bridged the gap between Dielectric Resonators and the world of antennas [69] [70]. The idea conveyed is simple : because the substrate permittivities involved are high, modes can indeed be confined inside the resonators; but because it is of finite value, a fraction of the energy can escape at the interface (see Fig. 5.1b) and thus lead to radiation. Over the last decades, this concept gave birth to tremendous developments with hundreds of papers published. Recommended bibliography sources on this topic are mainly the two most recent reference books [71] [72]; we can also mention a long and rich state of the art paper [73] and a PhD thesis dedicated to the fabrication and excitation of complex DRA shapes [74].



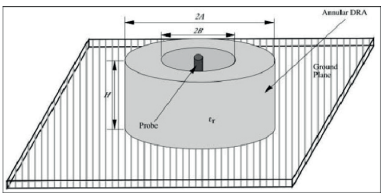
(a) Photos of the most common DRA shapes



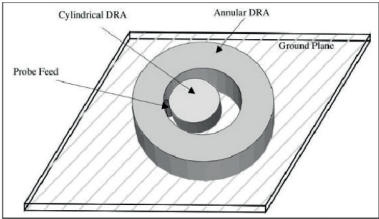
(b) Interface air-DRA and standing waves



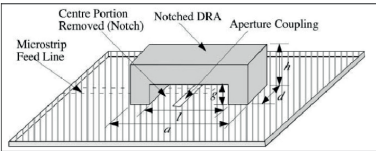
(c) Couplings schemes for excitation



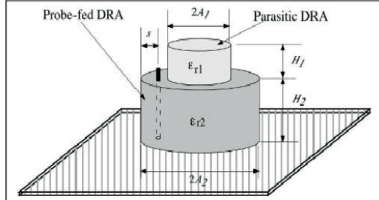
(d) Annular DRA fed by vertical probe



(e) Embedded annular DRA



(f) Notched DRA "upside-down"



(g) Stacked DRA

Figure 5.1: Generalities about DRAs - Some exotic shapes.

A particularly interesting fact is that DRAs share *at first sight* a lot of common points with microstrip patch antennas, or even promise to overcome them to some extent. Here is a list of DRA properties to keep in mind :

- Simple shapes such as rectangles can offer broadside radiation patterns with a low directivity (5-6dBi), which is well suited for phased array designs as explained in the first chapters.
- Excitation of DRAs can be performed in ways that are close to the ones used for patches (See Fig. 5.1c), in particular for producing (dual) circular polarization. In general, there are lots of analogies between both technologies; for example, structures such as stacked DRAs exist.
- There exist a particularly large amount of shapes and/or hybrid structures, involving multipile DRAs (embedded, stacked...), patches, dipoles with multiple resonances that can achieve impressive impedance bandwidths of sometimes more than 100%.
- The low amount of copper used in these topologies can result in an improved efficiency due to reduced ohmic losses.
- A DRA element operating at a given frequency is smaller than his microstrip patch counterpart, still because of the higher permittivities involved. And in the context of an array, smaller elements means more distance between the edges of neighboring elements, which can result in lower mutual couplings [75] [76].
- The lower the permittivity, the higher the radiated energy; but since this radiated energy is seen as a loss from the resonator point of view, the impedance bandwidth tends to increase with lower permittivities. On the other hand, the overall operation will stop if the permittivity is too low. A practical tradeoff was found with the choice of $8 < \epsilon_r < 12$ in the huge majority of publications.

All these properties caught our attention and brought the idea that a proper DRA could become a good candidate for a dual-circularly polarized array element. Yet the main challenge that appears is about the practical manufacturing issues in this technology. Usually, DRAs are made up of specific moulded materials, and excited with vertical probes, as was done most of the time in [74] and as can be seen in Fig. 5.1. Murata provides a collection of Ceramic-type materials [77] that can be used for this purpose.

Unfortunately, moulding, sticking, and manufacturing hundreds of probes (which turn out to be extremely sensitive to airgaps) is not adapted to the design of hundreds of elements in the context of an array. That's why in 2002, a method of "perforation" was suggested [78]; as illustrated in Fig. 5.2a and 5.2b, it consists in taking a more classical commercial substrate -the Rogers TMM series typically offers relative permittivities close to 10- and drilling the substrate until we leave only the matter that would correspond to the targetted shapes. With this method,

Chapter 5. Dielectric Resonator Antennas (DRA)

rectangles, cylinders, or embedded shapes can be produced and stacked if necessary. Large arrays [79] as well as Ka-Band reflectarrays [80] [81] have been produced and successfully measured in this way (Fig. 5.2c, 5.2d and 5.2e). It is not very elegant, but thanks to this method there was at some point a hope that an array of DRAs could be of some interest for Dassault Aviation. This attempt is described in the next section.

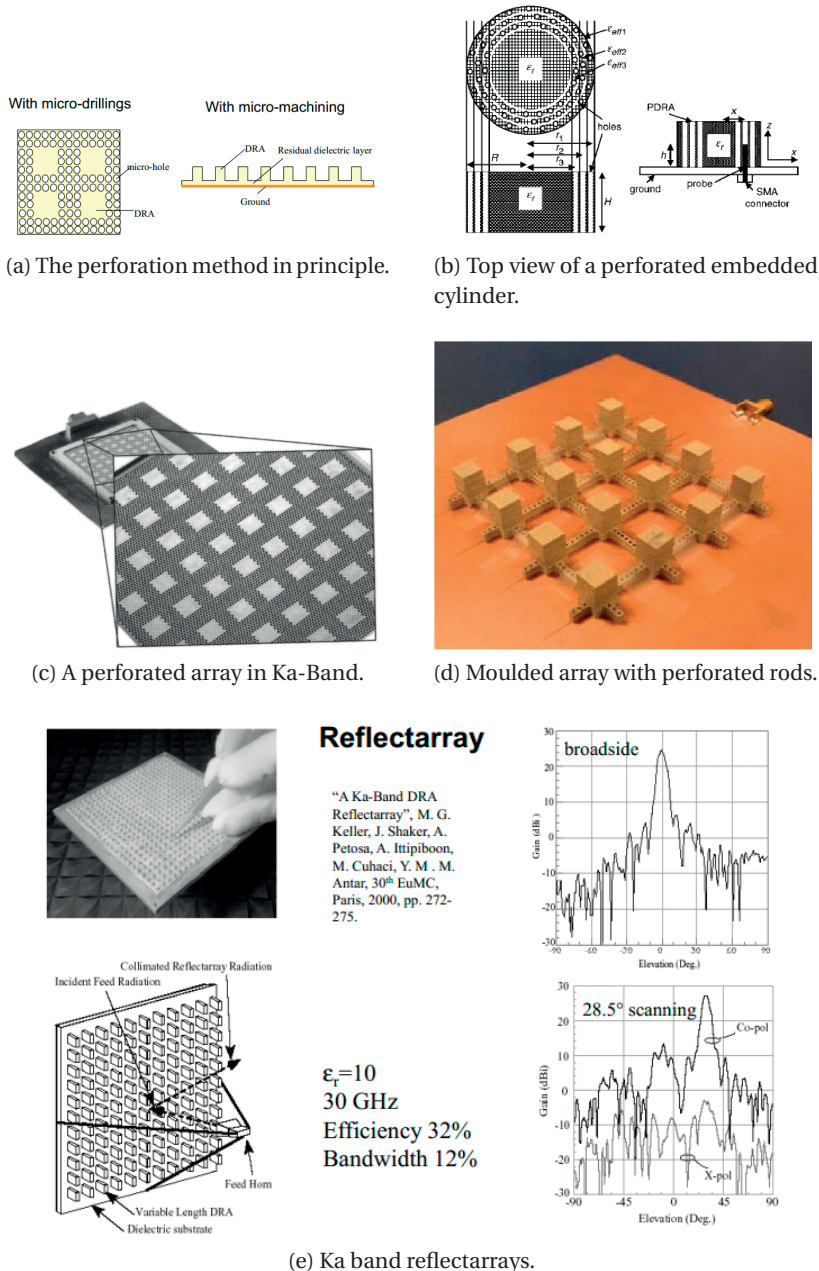


Figure 5.2: Building DRA arrays with the perforation method - Array examples.

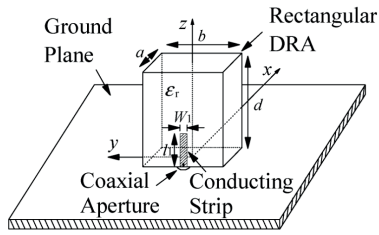
5.2 Hydra Element

The main question that will lead our research from now is : Can the sequential feeding method be applied to DRAs for improved dual-circularly polarization quality ? A second constraint is also associated to the problem : any solution suggested must be compatible with PCB mass production -namely the perforation method- and one should find a way to excite it with etched lines, apertures and/or metallized holes. The shape chosen in the end must exhibit a high degree of symmetry, unless the sequential feeding approach would be meaningless; these considerations are highly limiting the amount of possibilities.

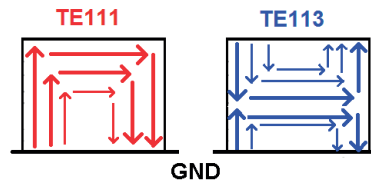
The so-called High profile Rectangular Dielectric Resonator Antenna (**RDRA**), renamed to **Hydra** for our purposes, brought somehow a solution. First proposed in 2005 [82], it is visible in Fig. 5.3a. A high profile block of dielectric is excited thanks to a strip that is printed on one of its edges. In this way, the two main modes - TE_{111} and TE_{113} , see Fig. 5.3b- are excited at the same time, and if the three dimensions of the RDRA are chosen properly, their respective resonating frequencies are close. A key point there is the fact that the radiation patterns for both of these modes (broadside) are very close to each other : a wideband operation is thus obtained.

The authors originally suggested to generate a simple circular polarization by adding a parasitic patch on an edge of the DRA, which is a quite narrow-band solution because it relies on a "perturbation trick". In principle, nothing would prevent us from exciting two modes in quadrature with two different strips in order to have dual circular polarization on a wider band. This is what was somehow done recently in a different context, when it was suggested to feed the DRA with two out of phase signals on opposite lateral sides [83] [84]; it resulted in a high purity linear polarization. We suggest to build on all these results with the three following contributions :

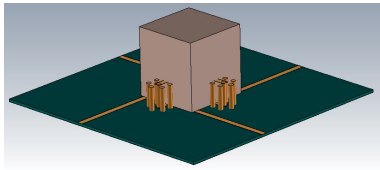
- The base of the Hydra is set to a square for obvious symmetry reasons, which unfortunately results in the loss of a degree of freedom for the design.
- The antenna is made up of a stack of three Rogers TMM10 layers of thickness 1.91mm, drilled as illustrated in Fig. 5.3f. The excitation strips -impracticable in PCB technology- are replaced by metallized holes through the first layer that brings the signal to a third of the total height (Fig. 5.3d). There, a horizontal etched line enters inside the DRA and excites both TE_{111} and TE_{113} modes.
- Four accesses of this type are used for the sequential feeding. The associated feeding circuit is made up of two rat-races couplers -which allow a signal to be split in two other out-of-phase signals- and of a directional coupler (Fig. 5.3e and 5.3g); a dual-circular polarization can thus be produced.



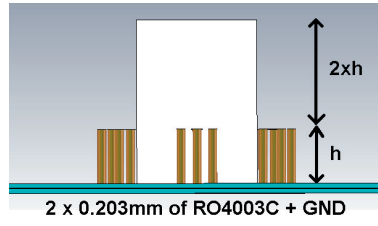
(a) The original RDRA.



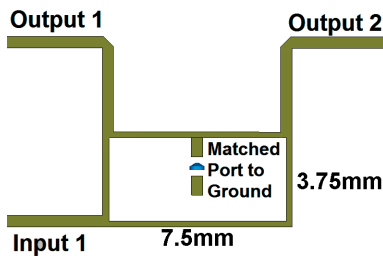
(b) Illustration of the two modes excited.



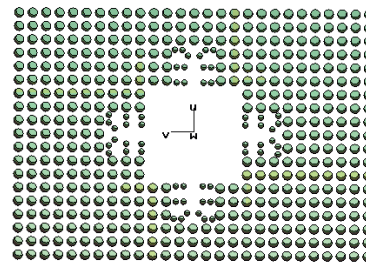
(c) HiDRA perspective view.



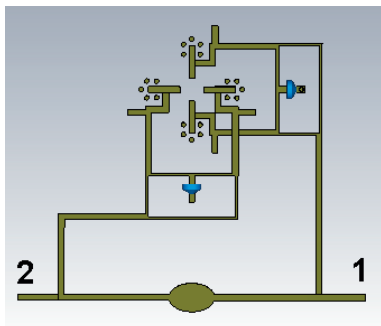
(d) HiDRA side view.



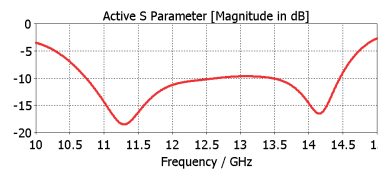
(e) Rat-race for the feeding system.



(f) Top view of a drilled layer of TMM substrate.



(g) Overall feeding system seen from above (GND invisible).



(h) Active S parameter for the DRA alone.

Figure 5.3: Sequentially-fed DRA.

An optimization was then performed on the dimensions of the DRA alone, which resulted in the optimal active S parameter shown in Fig. 5.3h. Once the rest of the feeding circuit was added, the overall S parameters (Fig. 5.4a) were all kept below -10dB on the Rx band (10.7GHz-12.7GHz). The axial ratio is more ambiguous; the best values for the radiation are located in the diagonal planes of the DRA, and they stay roughly below 3dB up to angles of 30° for most frequencies et for both polarizations. If the Rx band alone is considered, the axial ratio remains below 5dB up to angles of 50°.

In light of the very positive results obtained in section 4.4.2 with wilkinson based feeding circuits, there is no doubt that changing the circuit would yield much better results in terms of both axial ratio and S parameters. Yet the manufacturing issues would remain open anyway, while the more classical patches still provide a good practical solutions for the industry; that's why we decided to leave this exotic research as it is, hoping that it would find some use in the future. A paper was issued at Eucap Conference to describe this proof of concept [85].

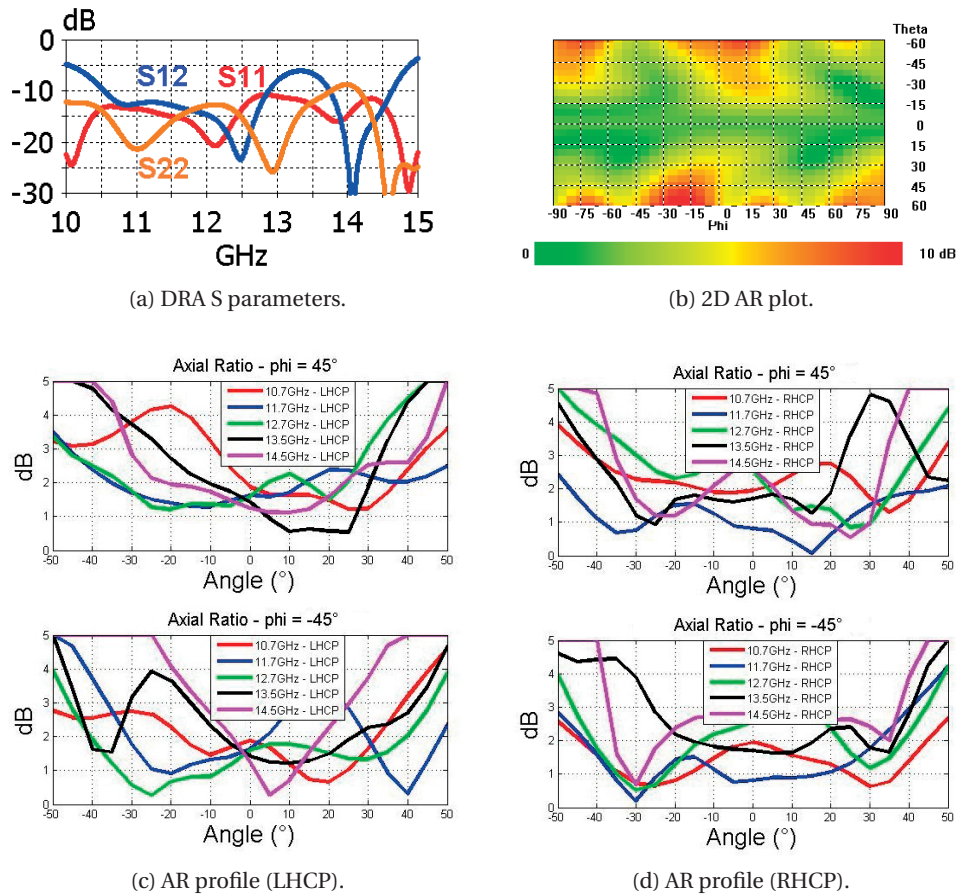


Figure 5.4: DRA simulation results.

6 Antenna arrays and the Dassault Aviation's SPECTRE software

Divide each difficulty into as many parts as is feasible and necessary to resolve it.

René Descartes

This chapter deals with the simulations of antenna arrays, involving the sequentially-fed planar antenna element as well as the DRA previously presented. The behaviour of an isolated antenna element is quite different from its behaviour when surrounded by identical neighbors. Indeed an element in the context of an array is directly perturbed by the presence of close neighbors in different ways : its radiation pattern can be degraded -both in terms of monotony of AR- by their influence (scattering effect). The S parameters are also modified, and usually a new set of simulations is necessary to compensate this perturbation. Finally, the problem of the mutual coupling between neighboring elements rises with its own impact on impedance matching and scan loss.

Simulations for an antenna array can be done in our case in three different ways. The first solution is to model an infinite array by surrounding an element with *periodic boundary conditions*, a classical approach supported by most commercial softwares. Simulations could be very fast in this way, but it was not the preferred way to do it for different reasons. Firstly, it is necessary to launch a new simulation for each steering angle and to store its results (at least in CST); moreover, the mutual coupling between an element and its neighbors cannot be extracted, because the neighbors are not defined in the model. Secondly, a real array -and especially, a small subarray intended for prototyping- has elements on its edges, which do not behave like elements inside a theoretically infinite array.

The only way to take into account these problems is to model complete subarrays in CST and to simulate them. S parameters and mutual couplings can be exported and post-processed in Matlab if required, and also models can be extracted in Gerber format in order to prepare prototypes. Yet there is a strong limitation to this approach : simulation times increase in a polynomial law ($O(N^3)$) as the number of elements increases. For four elements, running a

Chapter 6. Antenna arrays and the Dassault Aviation's SPECTRE software

single simulation can already take two hours and optimizing it may take days. If more than 10 elements are being considered, simulation times can become prohibitive.

Thus the third alternative way for us is to use a specific proprietary software of Dassault Aviation named SPECTRE. It allows in particular splitting a complex structure in several parts, that can be simulated separately and assembled in a numerical process called factorization. With additional help of some symmetries, square-shaped arrays of 64 elements could be simulated in 24h on Dassault Aviation's calculators. This work was performed directly in Dassault Aviation headquarters at St-Cloud France, during the months of February and March 2015.

In this chapter we provide in priority the results obtained with SPECTRE, and a few words will be said in the conclusion about some other ones obtained at LEMA with CST. Due to the fact that these SPECTRE results were plotted in March 2015 -and could not be reproduced at LEMA a few months later- it turns out that the graphical quality of the picture is sometimes low; we would like to apologize in advance for the inconvenience.

6.1 Simulation of large arrays in SPECTRE

SPECTRE is a proprietary electromagnetic simulation software developed by Dassault Aviation for its own purposes, and used in the framework of researches on the furtivity of military aircrafts. Among its important features, we already mentioned its ability to use both symmetries and factorizations to simulate complex structures by assembling smaller pieces. The drawback of this software compared to its commercial counterparts is the absence of an integrated graphical environment that would handle at the same time 3D modeling, easy parameterization of simulations and post-processing of the results.

Using command lines is not an issue for an engineer, but the absence of an integrated toolchain usually extends the time that is required to set up a simulation and to recover its results. We would like first to give a brief description of the different steps involved in a SPECTRE simulation process.

Step 1 : Design of a Catia model.

Catia is a well-known Dassault Aviation software for 3D modeling of complex structures, which is nowadays widely deployed in the industry. The models for SPECTRE have to be drawn in Catia, before generating a mesh and exporting it towards SPECTRE. Importing CST or HFSS models directly into Catia is in principle possible, but there are so many details to correct manually that in practice it is preferred to start again from the beginning. At this point, one must already have a clear idea of all the electromagnetic boundaries present in the system corresponding to the Catia model; an integer number has to be assigned to each of these interfaces, called a "KODE" in Catia vocabulary, and which will be used later in the meshing process as a tag to keep track of all of them.

Step 2 : Preparing a mesh in Catia/Amadeus.

Once the model is finished, the Amadeus mesh generator of Catia can be used to generate automatically a mesh that will be used by SPECTRE. Depending on the materials corresponding to each interface, it is necessary to define a proper mesh size for the different KODES defined earlier. Moreover, it is necessary to add up manually the excitation "ports" or "deltagaps" where the excitation should occur, together with their respective KODE. Finally, the orientation of the normal vectors for each mesh cell have to be checked to ensure that they will point in the same direction for every physical boundary between two media.

Step 3 : Processing the mesh in SPMB.

At this stage, the exported mesh is just a geometry containing no electromagnetic property. It is imported in a Dassault Aviation software written in Matlab and called SPMB (see Fig. 6.1).

Chapter 6. Antenna arrays and the Dassault Aviation's SPECTRE software

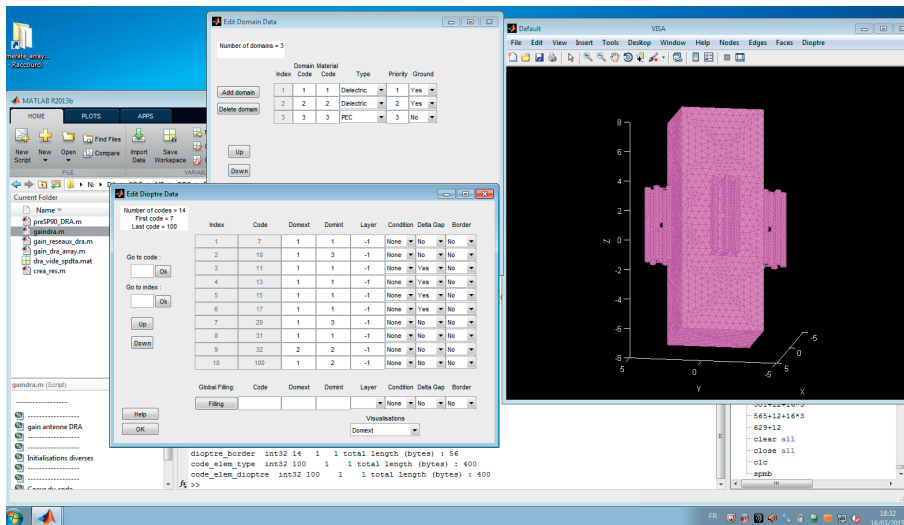


Figure 6.1: Illustration of the Dassault Aviation toolchain : parameterization of an ideal DRA in SPMB before the SPECTRE simulation.

Several important informations are provided through this interface :

- The list of (dielectric) materials used in the simulation, associated with codes.
- The nature of each interface, associated with a KODE (dielectric-dielectric, PEC, delta-gap...).
- The materials present on both sides of each interface.
- The symmetries used in the simulation (rotations or planar symmetries, at most two in total).

Step 4 : Configuring and launching the simulation itself.

SPECTRE is launched as a UNIX job by specific shell scripts, but before running a simulation some configurations have to be set :

- Folders must be ready for the inputs and outputs of SPECTRE.
- Script templates have to be modified to declare these UNIX paths, as well as the server on which the simulation will run.
- Some .xml files (called "cards") have to be prepared to declare which material indeed corresponds to the codes declared in SPMB. It may necessary to add new materials in the database with a dedicated script.

Step 5 : Post-processing the results with Matlab.

The results produced by SPECTRE are stored on the hard drive in files whose locations have been defined previously during the configuration step. They contain field values as well as S parameters. Their format named "lattice" is defined in Dassault Aviation's internal documents, and importation of the results in Matlab is done with specific Dassault Aviation libraries. It is then up to the user to extract interesting datas and to treat them in order to plot the desired quantity. For instance, plotting the AR of a sequentially-fed antenna element in some plane implies : extracting the fields corresponding to each excitation port in that plane, applying the proper phase shifts and linear combinations, deducing the Co-pol and X-pol values and deducing the AR itself.

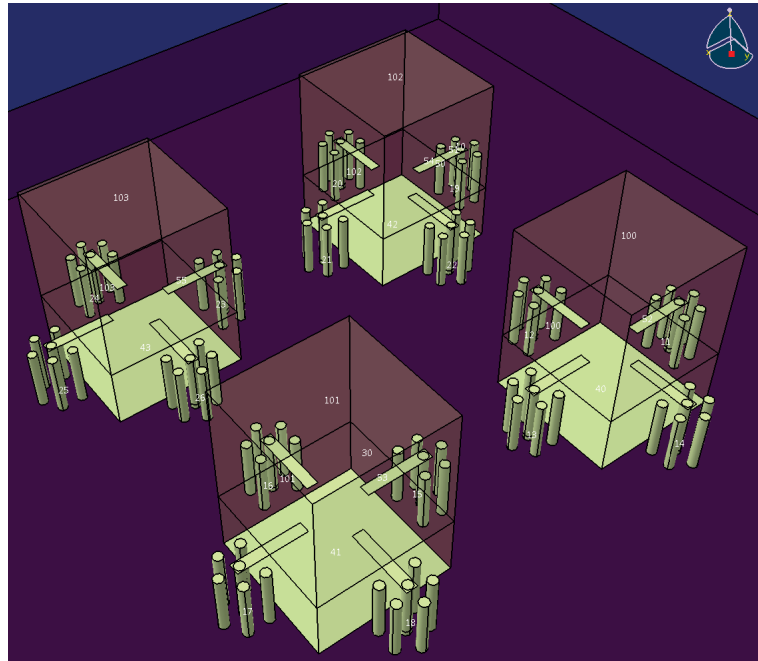
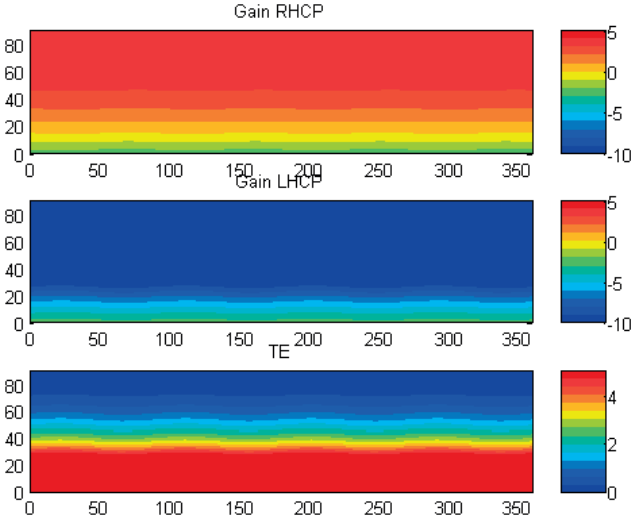
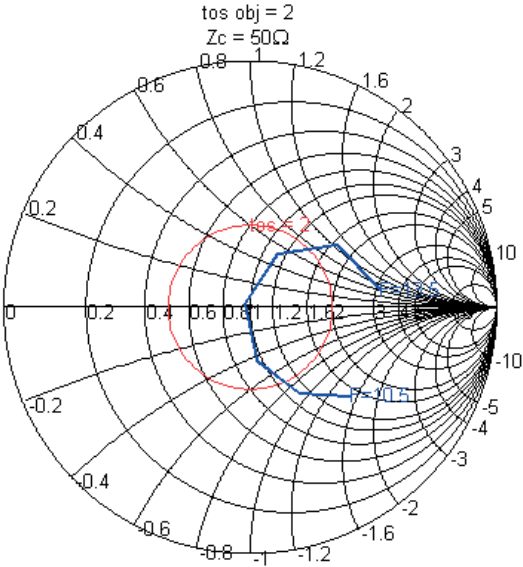


Figure 6.2: Perspective view of a 2x2 array of DRA in Catia.



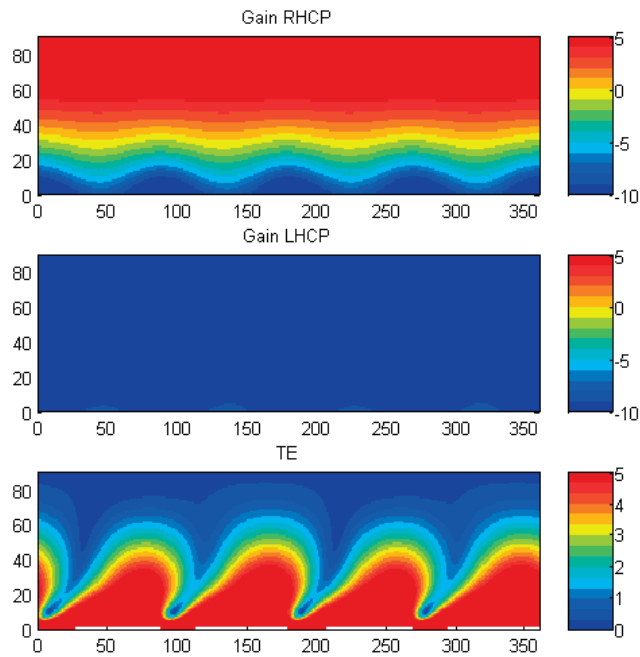
(a) RHCP/LHCP gains and AR for an isolated DRA (TE = Taux d'Ellipticité).



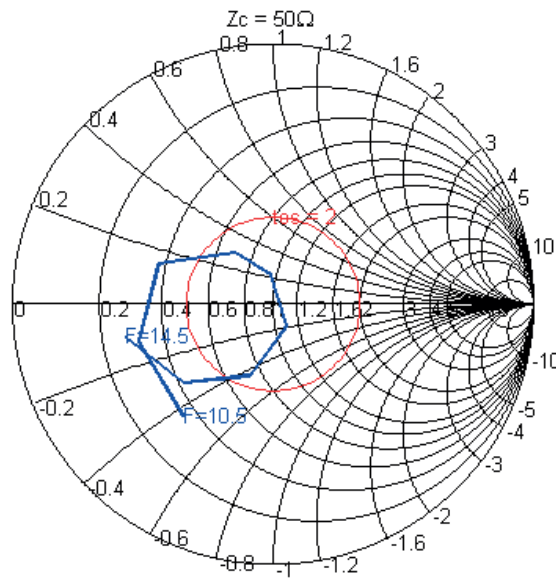
(b) Smith chart for an isolated DRA (Active S parameter).

Figure 6.3: Spectre simulation of an isolated DRA with ideal excitations.

6.1. Simulation of large arrays in SPECTRE



(a) RHCP/LHCP gains and AR for an isolated planar antenna.



(b) Smith chart for an isolated planar antenna (Active S parameter).

Figure 6.4: Spectre simulation of an isolated sequentially-fed stacked patches antenna with ideal excitations.

Chapter 6. Antenna arrays and the Dassault Aviation's SPECTRE software

Several antennas have been simulated during the two-months period spent in St-Cloud, and four of them are reported in this chapter due to their relevance in the discussion :

- A single sequentially-fed DRA on an infinite ground plane, excited by four ideal delta-gaps. DRAs were appreciated as benchmarks because they were easier to model and to simulate than planar structures involving more layers and apertures.
- A single sequentially-fed stacked patches antenna also excited by four ideal deltagaps.
- A small subarray of 2x2 DRAs on a finite support. No factorization or symmetries have been used for this benchmark.
- An 8x8 array of stacked patches elements, using factorization and symmetries (the most important simulation).

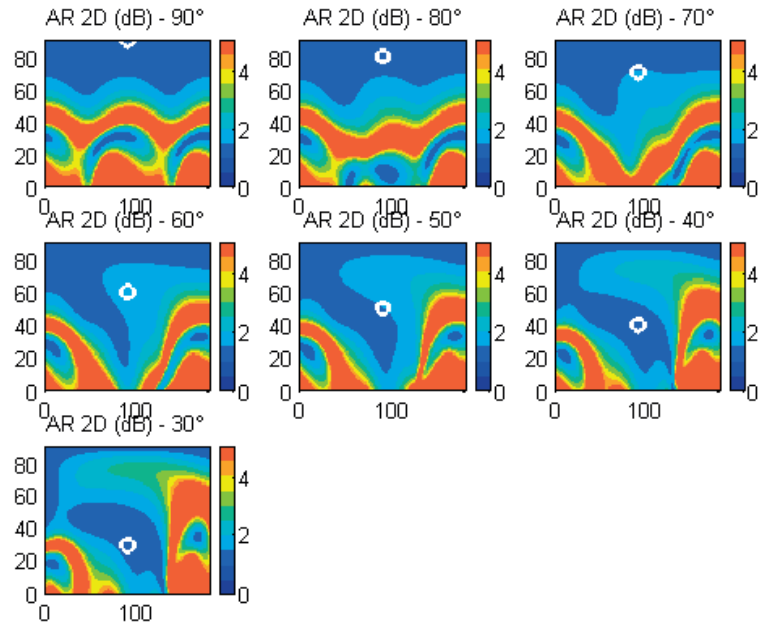
The single DRA is visible for instance in Fig. 6.1, where it is clear that the ground plane is removed and replaced by a symmetry. The corresponding radiation properties and active S Smith charts are visible in Fig. 6.3a and 6.3b. Impedance matching is achieved around 11.5GHz, and proper radiation patterns with an AR below 3dB up to 50° away from broadside have been obtained. Results for the stacked patches (Fig. 6.4a and 6.4b) are similar.

The 2x2 subarray of DRAs whose Catia model is visible in Fig. 6.2 is helpful as a benchmark to start observing a basic steering before implementing advanced simulation methods using factorization and symmetries. This model is obtained by duplicating the DRA and phase shifts are applied to its elements to get the proper steering angle.

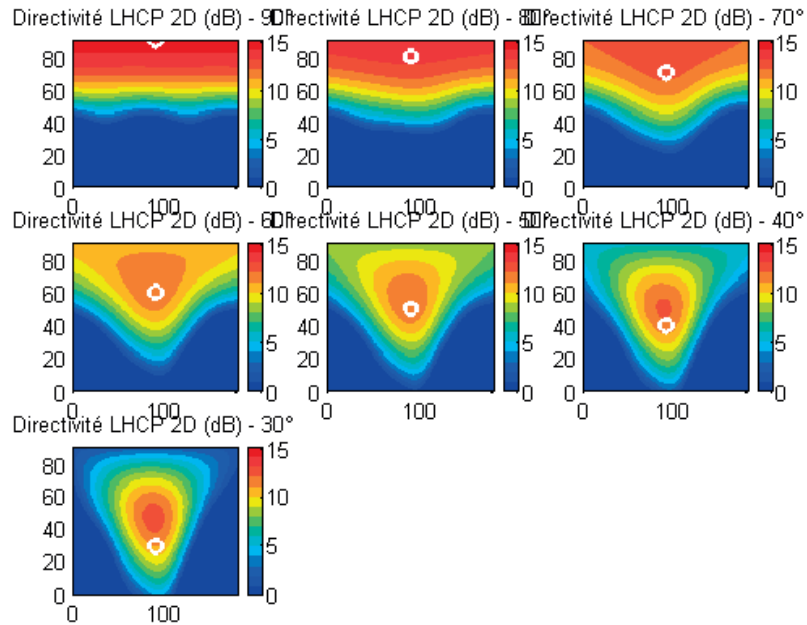
The effect of the steering at central frequency can be seen in Fig. 6.5. The circle in white corresponds to the targeted angle; clearly, the beam maximum is moving from broadside and following the white circle, but it seems that there is an increasingly important discrepancy between the actual maximum and the expected one.

This effect was also observed in similar CST simulation. It is typical of small arrays, where a lot of elements are located at the edges and exhibit distorted embedded radiation patterns. It can become difficult -if not impossible- to reach angles close to the endfire direction.

6.1. Simulation of large arrays in SPECTRE



(a) AR in 2D for various steering angles.



(b) Dir in 2D for various steering angles.

Figure 6.5: Beam steering for a 2x2 Array of DRA : post-processing of the SPECTRE results in Matlab (90° corresponds to the broadside direction).

Chapter 6. Antenna arrays and the Dassault Aviation's SPECTRE software

Fortunately this undesired effect vanishes as the size of the array increases. The last and most important simulation of an 8x8 array of stacked patches is described in Fig. 6.7. The design steps are the following :

- An eighth of antenna element is cut from the entire element and meshed alone.
- Thanks to rotation and planar symmetry operations, a mesh for the complete element "under a covering interface" can be generated.
- Thanks to this method, the mesh obtained is very symmetrical and it can be duplicated without any trouble to generate a 4x4 antenna array.
- The simulations are launched for both the isolated element "inside the covering interface" and the whole arrays (using two symmetry planes to get an 8x8 array).
- The results are assembled and the obtained fields are post-processed in Matlab.

The beam steering 2D profile is reported in Fig. 6.5. Another set of plots is proposed in Fig. 6.6 in order to provide a better view of the radiation in the plane $\phi = 0^\circ$. First, a plot of the maximum of the beam vs the expected steering angle shows that the discrepancy around 60° is around a few degrees only, which can be compensated easily by modifying slightly the excitation phases.

The directivity as a function of the steering angle shows a monotonous decrease and a stable value in frequency (only the highest value in frequency differs from the others with a more directive profile, which is not surprising). Ideally, the profile (in linear scale) should follow a cosine profile, and thus a loss of 3dB is expected at 60° ; it is roughly the case here also. The AR final degrades as the angle increases but doesn't exceed 4dB.

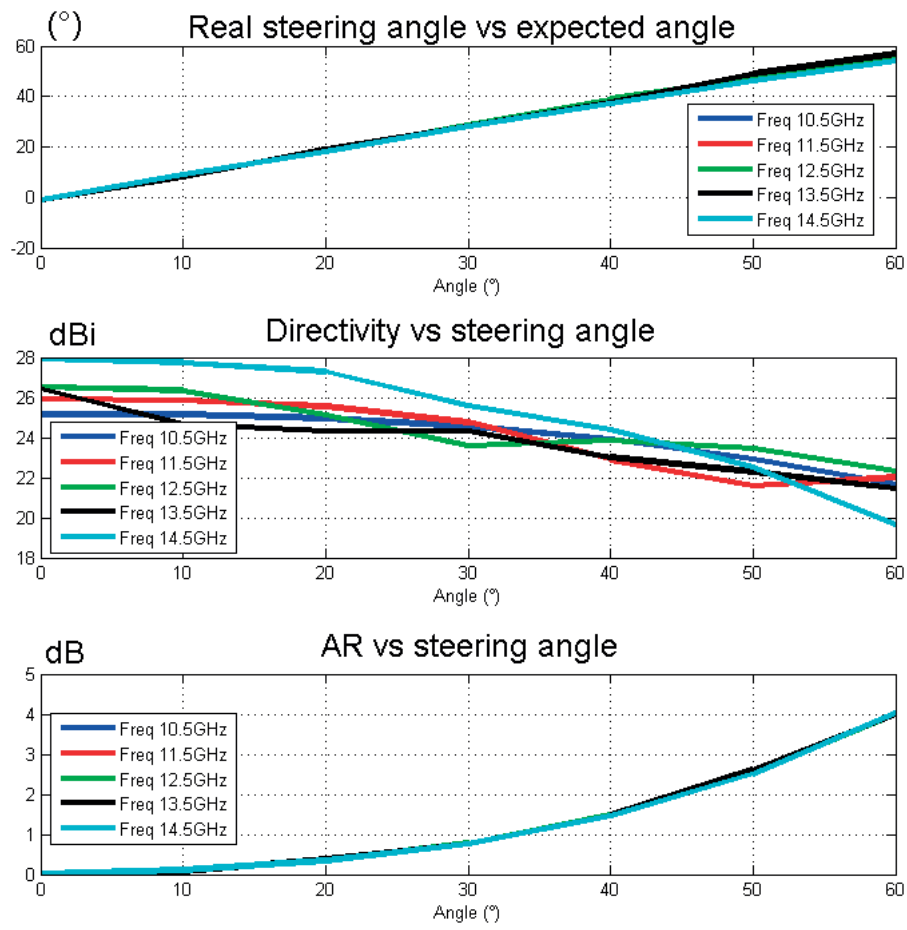
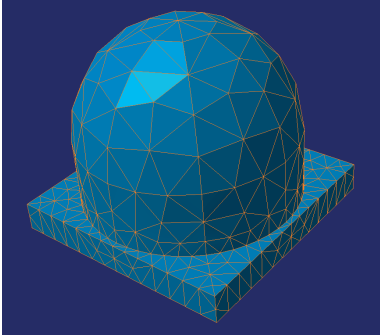
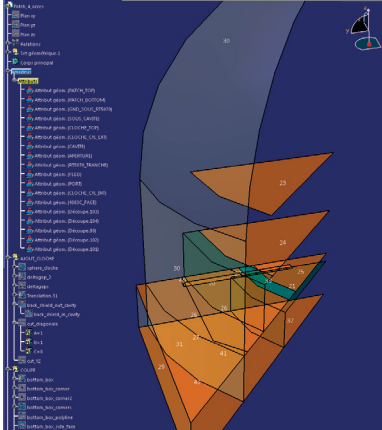


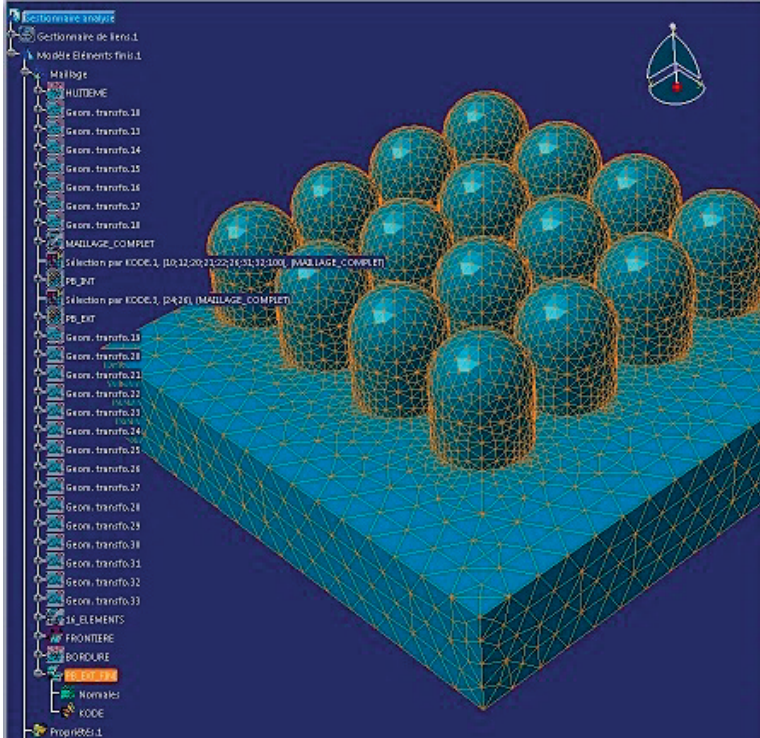
Figure 6.6: Beam steering with an 8x8 array in the $\phi = 0^\circ$ plane.



(a) Outer mesh of a single antenna element.

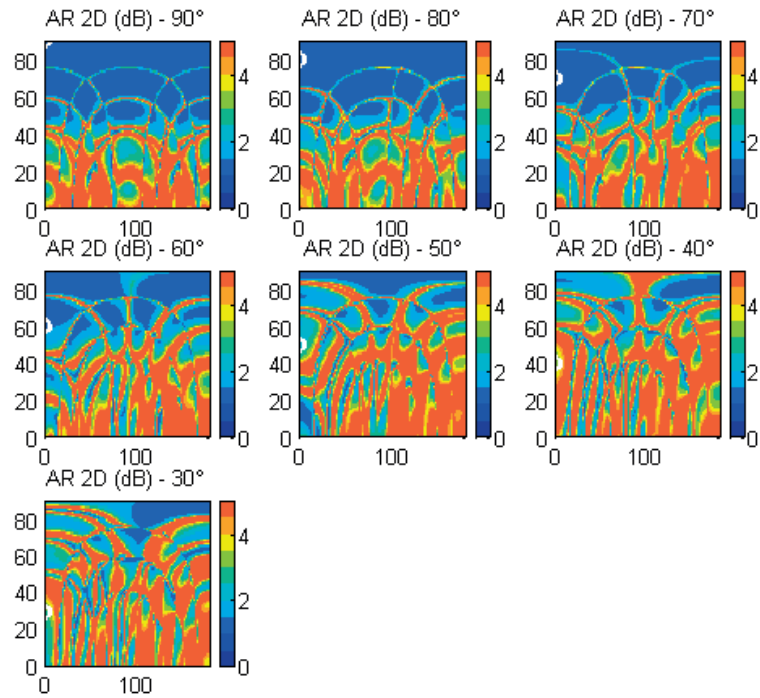


(b) Eighth of the antenna element used to generate a symmetrical mesh with mirroring and rotation operations.

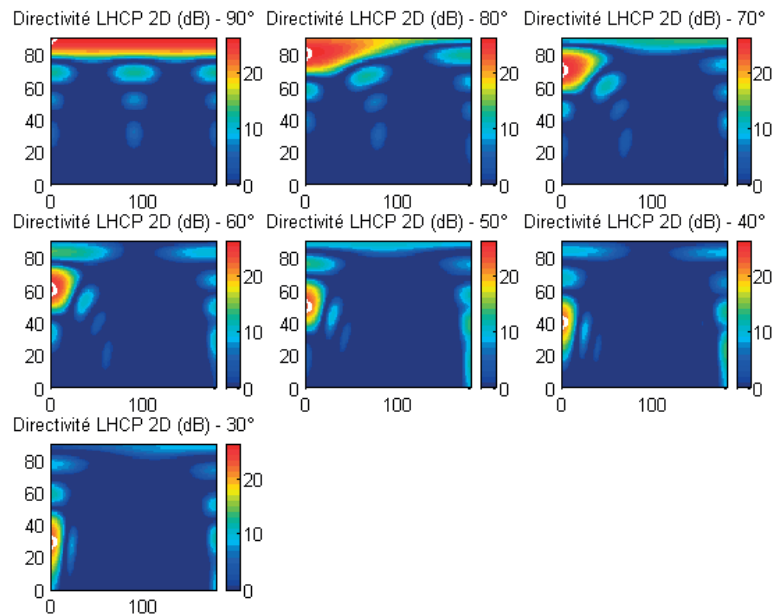


(c) External mesh of a 4x4 subarray in Catia.

Figure 6.7: Simulation of an 8x8 array of planar antenna elements : setting up the factorization method of SPECTRE.



(a) AR in 2D for various steering angles.



(b) Dir in 2D for various steering angles.

Figure 6.8: Beam steering for a 8x8 array of DRA : post-processing of the SPECTRE results in Matlab (90° corresponds to the broadside direction).

6.2 Conclusion and remaining issues

Thanks to the SPECTRE software of Dassault Aviation, a planar antenna arrays of 8x8 elements was simulated in 24 hours, and its beam steering capabilities were characterized. This phased array can cover angles from 0° (broadside) to 60° (close to endfire), while keeping a directivity above 20dBi and an AR much below 6dB in every direction. Excitations were considered ideal for this study. It brought simulation results that could not be obtained at LEMA at the moment with standard softwares like CST. Especially the possibility to simulate an 8x8 array and to observe the quality of the beam steering -compared to its 2x2 counterpart- was appreciated.

A complementary work about subarrays of planar elements was performed at LEMA, but it will not be fully reported here for the sake of brevity. For instance, one can find in the private technical reports for semesters 4, 5 and 6 :

- A 2x8 subarray of elements simulated and built in Rx-Band, with a corporate network on each side of the array to feed each line of eight elements. Although the quality of polarization and matching were not optimal, the merit of this prototype was to allow us to observe a beam steering in practice when a delay was applied between the lines.
- A code (in C) was written to allow the automatic generation of an array with its corporate distribution system in CST. This code was partially adapted for Catia.
- No results in terms of S parameters or mutual couplings could be obtained from SPECTRE in the short internship in St-Cloud, but complementary studies on antenna elements surrounded by neighbors could be performed in CST.

The last point deserves more comments. The S parameters of an *active element* -i.e. an element surrounded by array neighbors which are all excited with their respective amplitudes and phases- include mutual coupling effects. In fact, a subarray of elements can be seen as a multiport system, and in this context the S parameter of a single element is better described by an *active S parameter*. This active S parameter depends on the phases of subarray elements, and thus directly on the steering angle.

In practice, we studied it by simulating small arrays of 3x3 Rx-Band elements and by exporting their S parameter to Matlab, where a post-processing gave us the active S parameter as a function of both the frequency and the steering angle. We tried several techniques to decrease the mutual couplings in our CST models, but they were either inefficient or working at the expense of the impedance bandwidth. This is due to the discussion that was started in chapter 3 about the inherent tradeoffs between directivity, mutual coupling and impedance bandwidth for antenna elements in arrays.

We could never keep the active S parameter below reasonable values for all frequencies and angles, at least for the Rx-Band studied up until now. Fortunately if the required bandwidth is decreased to a much less stringent value, things are getting simplified. It is the case in

6.2. Conclusion and remaining issues

Tx-Band or if we scale up our elements towards K/Ka-Bands, and the next chapter is devoted to modified antenna elements working in these frequency bands.

7 The particular case of a narrow bandwidth

Nature is pleased with simplicity. And nature is no dummy.

Isaac Newton

7.1 A Tx Band element with directionnal coupler

Besides the Rx band (10.7GHz-12.7GHz, 17% fractional bandwidth) that was the main target of the project up until now, some other bands are interesting for Dassault Aviation. The first one is the Tx band (14GHz-14.5GHz) complementary to the Rx one. The most striking fact about it that its fractional bandwidth -namely 3.5%- is very low compared to its Rx counterpart. Indeed, most of our issues over the first chapter consisted in finding a tradeoff between the wide Rx bandwidth and a whole set of other constraints, such as the limited space available, quite high expectations on the polarization quality, or a low coupling with neighboring elements.

A bandwidth of the order of several percents is much easier to handle by modifying the radiating element. Moreover, Dassault Aviation is also increasingly interested in two subsets of the Ka band -respectively around 20GHz and 30GHz- which are available for civil Rx/Tx transmissions. They share this particularity that their fractional bandwidth is around a few percents, so in principle any Tx band solution could be rescaled to operate in Ka band.

The first idea came from a previous work done at LEMA by R. Glogowski and presented in two recent papers [86] [87]. Its goal was to design a single-circularly polarized patch element working around 25GHz, with a fractional bandwidth of 5%. Subarrays made up of lines of six elements were then constituted out of it. Basically, the patch was etched on a very thin substrate and suspended inside a metallic cavity; this cavity was very efficient in preventing coupling with neighboring element, but at the expense of the bandwidth that shrinks a lot whenever the fields are "confined" in this way. The vacuum "environment" of the patch was somehow compensating this negative influence of the cavity by ensuring a bandwidth large

Chapter 7. The particular case of a narrow bandwidth

enough to cover several percents. Finally, the circular polarization was produced thanks to a single feed and to a dissymmetric cross-shaped aperture below the center of the patch.

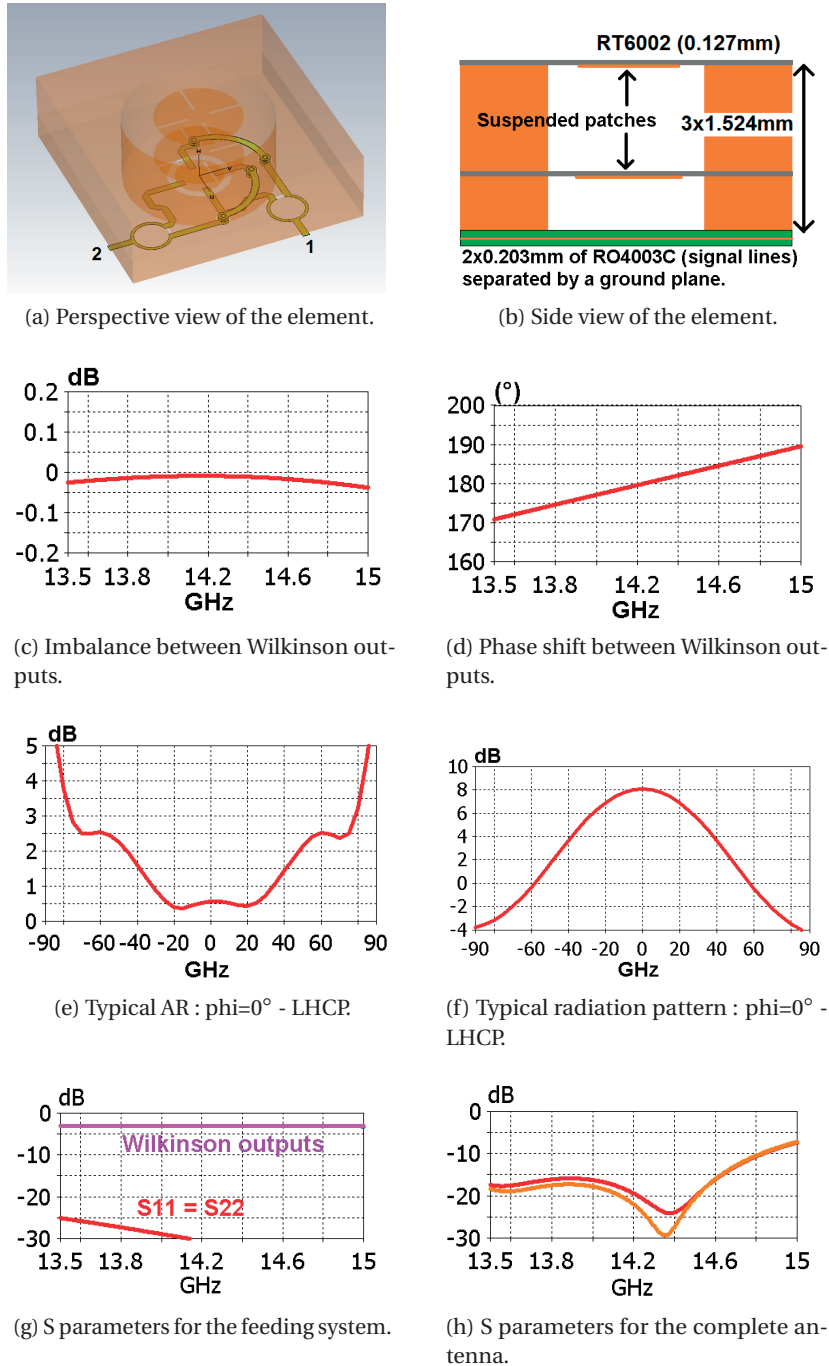


Figure 7.1: Tx-band antenna inside a cavity.

7.1. A Tx Band element with directionnal coupler

Several ideas have been mixed to come up with the solution depicted in Fig. 7.1a and 7.1b. Let's summarize them :

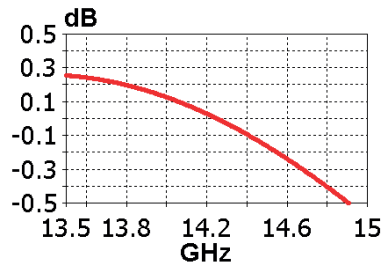
- The single polarization excitation scheme can be replaced with our more evolved sequential feeding, once properly rescaled to the targetted frequency band.
- Instead of manufacturing the cavity with mechanical processes, a stack of 3 layers of Rogers RO4003C substrate is used (the thickness for each of them 1.54mm). A cylindrical cavity is drilled and fully metallized with a very simple PCB process. This substrate was chosen for its availability, ease of manufacturing (especially for metallization) and its important height/thickness necessary to improve the bandwidth as much as possible. The resulting pile of substrates can be sticked with a general purpose glue.
- Two patches are stacked, again in an attempt to get a more confortable bandwidth. The pertinence of this choice will be discussed and criticized.
- Some slits have been done in the patches (clearly visible in Fig. 7.1a). This classical trick is sometimes used to decrease the size of a patch antenna [1]. The reason is the following : observing the simulation results tended to prove that, if the patches are too large, they almost "close" the cavity in which they are embedded, with a high negative impact on the bandwidth. Reducing the size of the patches in this way turned out to be a good empirical solution; it will be criticized further like the previous point.

Chapter 7. The particular case of a narrow bandwidth

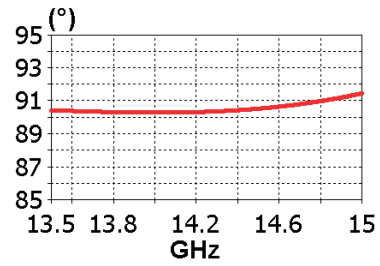
Table 7.1: Best values found for the ideal sequentially-fed Tx-band antenna.

parameter	value	unit
50 Ω input line width	0.45	mm
Aperture radius	1.75	mm
Aperture width	0.5	mm
Via aperture radius	0.5	mm
Wilkinson radius	1.3	mm
Via pad radius	0.35	mm
Metallized holes radius	0.2	mm
Stub lengths	0.95	mm
Radius of Wilkinson adapter	1.35	mm
R1	3	mm
Gap for Wilkinson resistor	1	mm
Patch radius	2.9	mm
Width of patch slits	0.2	mm
Radius of cavity	5	mm
Ratio of slitt / radius	0.75	x
Hybrid branch width W	0.8	mm
Hybrid branch length L	3.5	mm
d1	5.15	mm
d2	3.5	mm
meander size	0.5	mm
miter bend size	0.45	mm

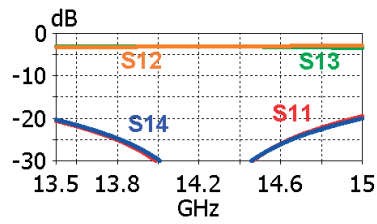
7.1. A Tx Band element with directionnal coupler



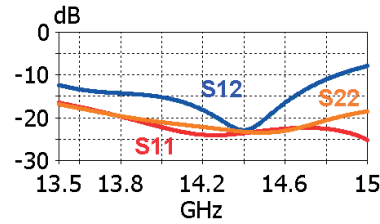
(a) Amplitude imbalance between hybrid coupler outputs.



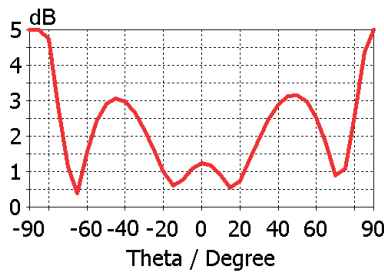
(b) Phase shift between hybrid coupler outputs.



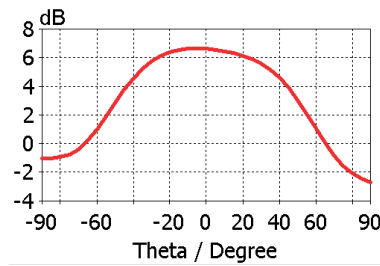
(c) S parameters for the hybrid coupler.



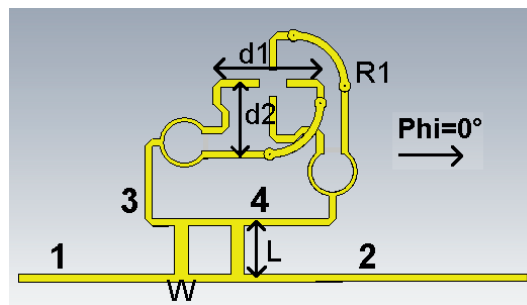
(d) S parameters for the complete antenna.



(e) Typical AR : $\phi=0^\circ$ - LHCP.



(f) Typical directivity : $\phi=0^\circ$ - LHCP.



(g) Top view of the complete antenna.

Figure 7.2: Tx-band antenna with hybrid coupler.

Chapter 7. The particular case of a narrow bandwidth

Once all the basis have been clearly defined, the design procedure is divided in several straightforward steps. First, the Rx-band feeding system is rescaled in order to operate in Tx band, and optimized alone thanks to a parametric sweep on the different dimensions involved. A slight modification had to be applied to obtain a proper phase shift while respecting some topological constraints : a meander was added, as can be seen in Fig. 7.2g, which besides this doesn't change the overall operation in any way. Finally an excellent matching, a negligible amplitude imbalance in the excitation amplitudes and a phase discrepancy of less than 5% on the band is reported in Fig. 7.1. Table 7.1 record all the dimensions.

The next step consisted in optimizing the patch, aperture and stub dimensions alone, before an overall finetuning when the feeding system was added. The radius of the cavity was fixed at the very beginning, because it depends on the constraints at array level. Recall that if a maximal steering angle of θ_{max} is required, a maximal distance between elements is fixed :

$$d_{max} = \frac{\lambda_{min}}{1 + \sin(\theta_{max})} \quad (7.1)$$

Which yields 11mm in our case. Some margin has to be left for the mechanical consistency of the cavities and for a "reasonable" isolation between neighbors, thus the choice of a radius of 5mm. The results for the element show an AR below 3dB on a wide range of angles for both polarizations, a directivity of 8dBi and a return loss of below -15dB. The isolation between excitations is much below -30dB in simulations and does not even appear on the plots.

The last step is about adding a directional coupler for the dual circular polarization. In the case of the Rx band, a wideband solution was required, which was chosen to be a couple of elliptical patches that presented some difficulties for manufacturing and integration. But here again, the limited bandwidth required allows the use of the very classical branchline hybrid coupler [45]. This single layer microstrip structure is compact and easy to design; it is optimized alone before being plugged to the rest of the antenna, and the results are reported in Fig. 7.2g.

According to the simulations in the Tx band, an amplitude imbalance of less than 0.15dB and a phase discrepancy of less than a degree are obtained between the outputs of the coupler. The return loss is kept below -25dB, while the AR seems to exceed 3dB a little bit only at extremal values of the angle range. Regarding the radiation pattern, the imperfections of the coupler have a limited impact : a slight asymmetry appears and the directivity decreases between 6dBi and 7dBi, which is even a good point. The S parameters remain below -20dB, except the S12 parameter whose maximal value is rather around -15dB.

7.2 Measurement results

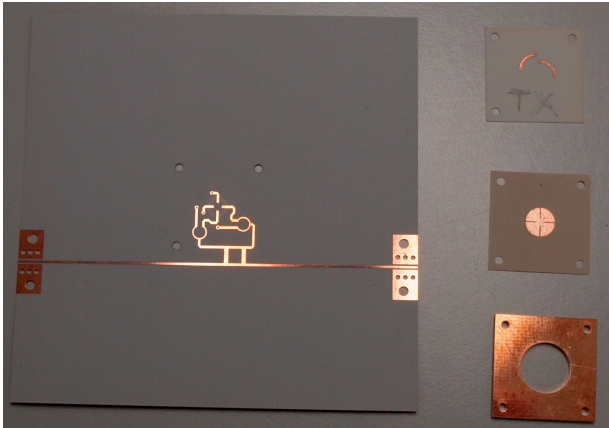
Several prototypes have been produced for cavity-surrounded elements in Tx-Band. One of them was a single element directly fed by two orthogonal accesses, while another more evolved version was surrounded by eight neighbors that could be used to measure mutual couplings. Unfortunately we did not pay attention to the fact that the ground plane was too short, and consequently the connectors were too close to the antenna. The radiation properties suffered from it, and thus the results won't be reported here.

The prototype presented here is a validation of the model presented in the previous section. As can be seen in photo 7.3, a layer implementing a complete feeding system with a hybrid coupler is assembled with the cavities and patches shown on the right. The ground plane is extended as we did in chapter 4 for the Rx-Band prototype.

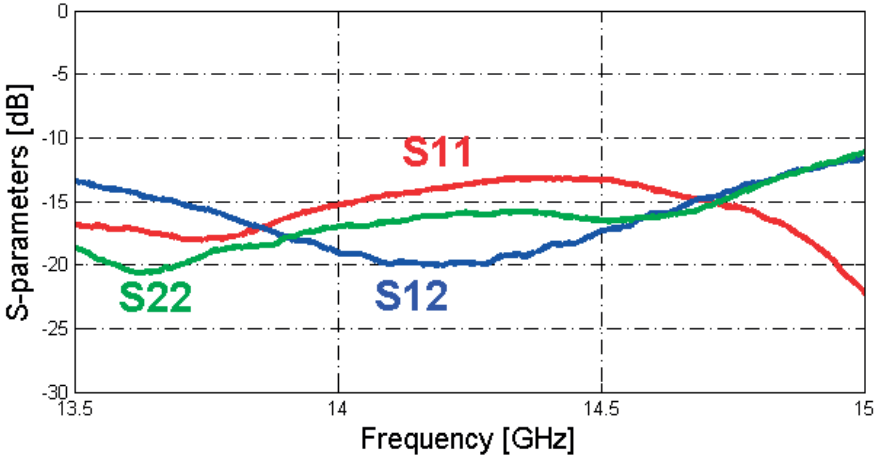
The measured S parameters are most of the time below -15dB (-13dB at most) on the desired band. We expected better results, but they are satisfactory anyway. The sources of discrepancies are various here : tolerances on the (manual and very delicate) soldering of the resistors and metallization of via holes; but also etching tolerances, especially for the hybrid coupler which is very sensitive even to a few tens of micrometers.

Radiation patterns and AR plots are provided for both principal planes in Fig. 7.4. Since the band is narrow, only the central frequency was considered, but both polarizations - corresponding to the excitation of either port- are reported. The radiation pattern is quite symmetrical and monotonous; the AR remains below 6dB most of the time and frequently below 3dB.

Chapter 7. The particular case of a narrow bandwidth



(a)



(b)

Figure 7.3: Photo of the Tx-Band antenna with hybrid coupler - Measured S parameters.

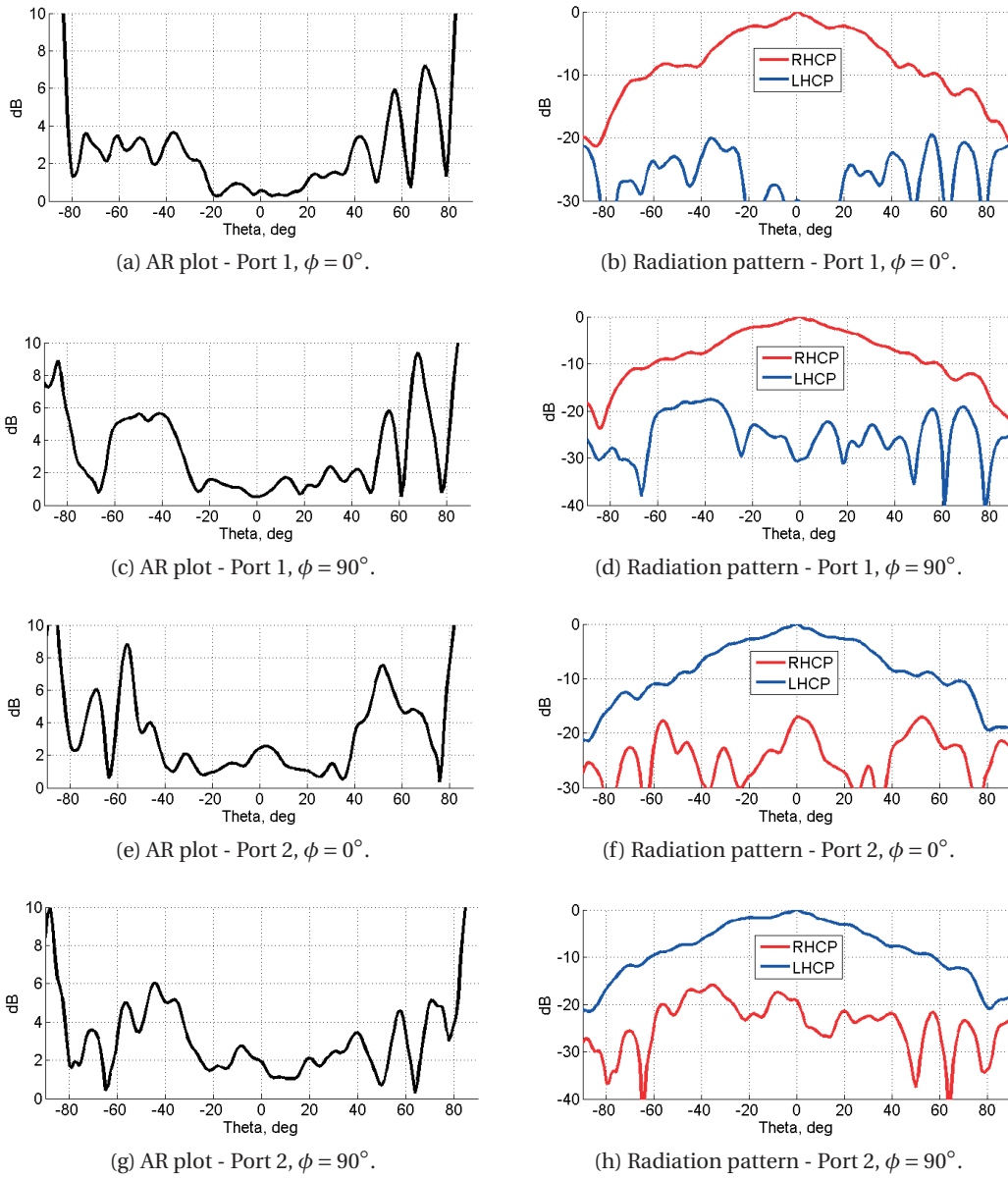


Figure 7.4: Measurement results for the Tx-Band antenna with hybrid coupler (both polarizations and principle planes).

7.3 Simplification of the element - 2x2 subarray

In the preceding section, stacked patches were used to achieve the required bandwidth, as was done previously for the Rx-Band. We also resorted to slitted patches to decrease their size and to ensure their proper inclusion in the metallic cavity. It resulted in a quite complex layer stackup with not less than three layers for the cavity, two for the patches and two for the feeding system.

It was noticed after the development of the stacked patches structure that this complexity was superfluous. Indeed a single patch antenna can in fact achieve the same bandwidth and radiation properties. This leads to an important simplification of the design, with only a single layer for etching the patches and a single one for the cavities. The key point is to increase the distance between the excitation slot and the patch from 1.5mm to around 2.6mm; a Rogers TMM6 substrate is then chosen to drill a cavity of proper thickness, instead of the stack of RO4003C used previously. Also, the use of a slitted patch turns out to be useless, as a normal patch brings the same simulated results as a slitted one.

Once this simplified structure was found to be working well, our attention was moved to the design of a small subarray that would demonstrate the operation of an element in the presence of neighbors. It includes :

- The mutual coupling between elements.
- The variation of the Active S parameters with the steering angle -which highly depends on the mutual coupling-.
- The perturbation of the radiation property induced by the surrounding antenna elements.

A design and optimization process was led in three steps with CST. First, the key geometrical parameters (size of the slot, length of stubs, cavity height and patch radius) were optimized on a single element with ideal excitations to get the best S parameters. Then, the feeding system proposed in the previous section was reused with the same dimensions and a "complete element" was simulated. As expected, it exhibited a symmetrical radiation pattern with an AR below 3dB for all angles of interest.

Finally a 2x2 array was modeled with the geometrical parameters temporarily set to the best values found previously for a single element. The four patches were surrounded by "dummy neighbors" for the sake of maintaining the environment as symmetric and realistic as possible. The situation is depicted in Fig. 7.5 where perspective, side and top views are provided for the overall system. The top views are in fact gerber views of the files that went for prototyping; it explains why the connector pads are visible and why four of the feeding lines are bended in order to ensure that there is enough place for the connectors.

7.3. Simplification of the element - 2x2 subarray

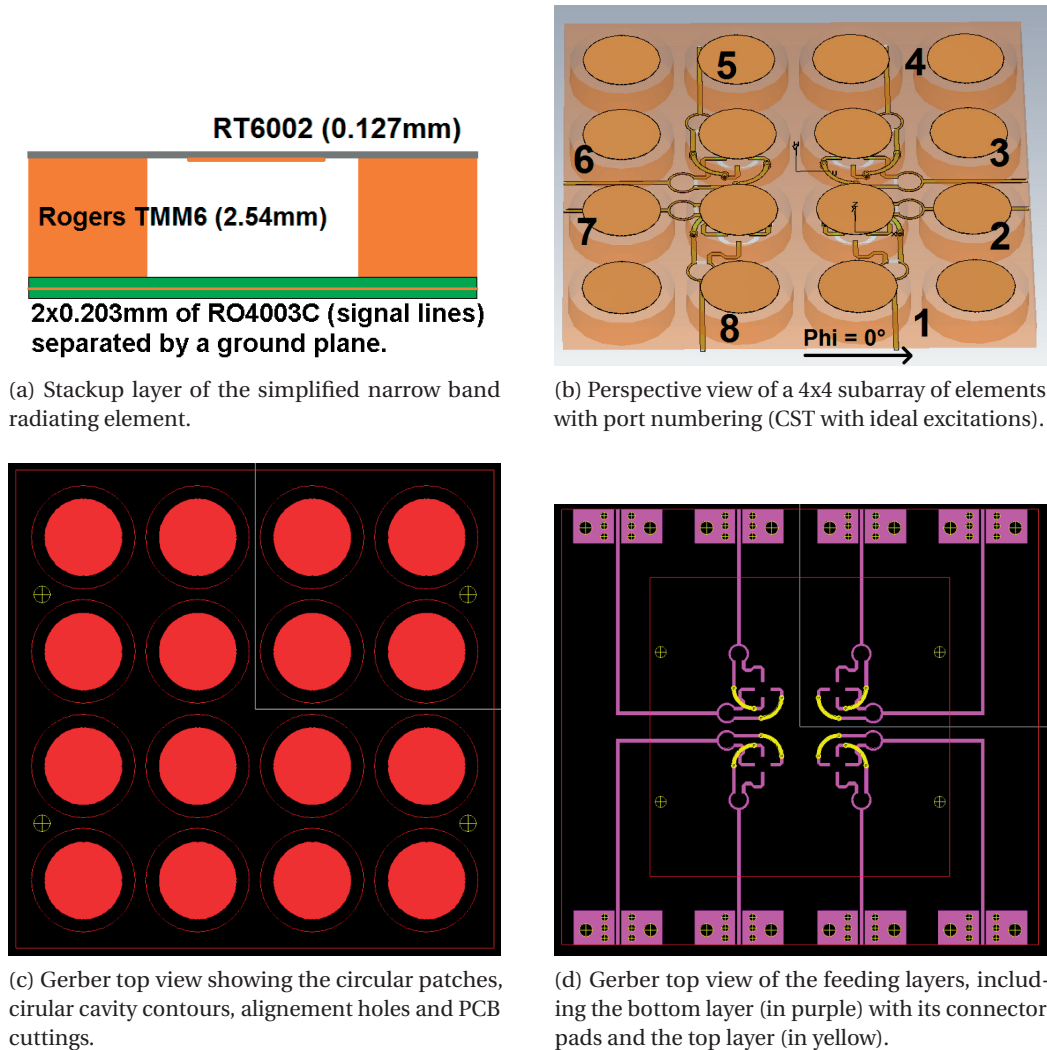
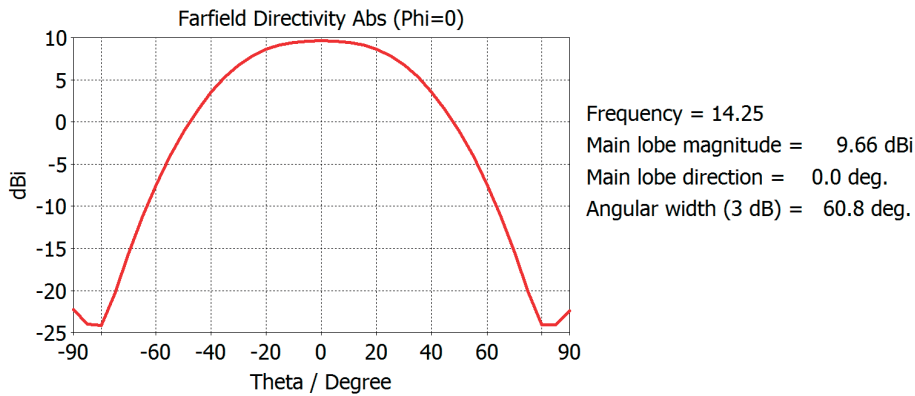


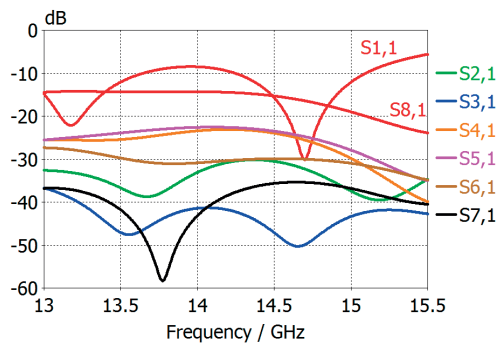
Figure 7.5: Description of the simplified element and of a 2x2 subarray surrounded by dummy patches.

Eight ports are used in total to excite the subarray, and the feeding of each element is physically rotated of 90° with respect to its neighbors. It has to be compensated by a proper phase shift in the feeding signal (during the post-processing step under Matlab in our case). This rotation plays a double role; the first and most obvious is that this rotation allows a very practical feeding scheme, as the connectors are immediately spread around the PCB and no feeding lines accidentally cross in any way. But also this rotation is a sequential rotation at subarray level, which is the source of an additional improvement in the AR. It compensates the fact that the AR is seriously degraded for radiation angles close to endfire whenever neighbors are added around an isolated radiating element.

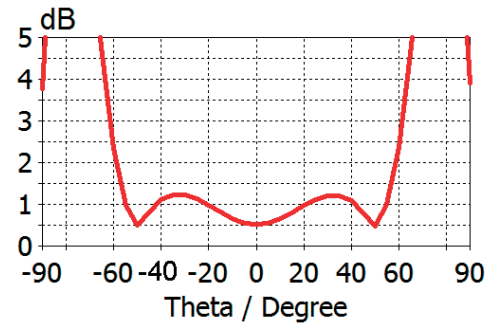
Chapter 7. The particular case of a narrow bandwidth



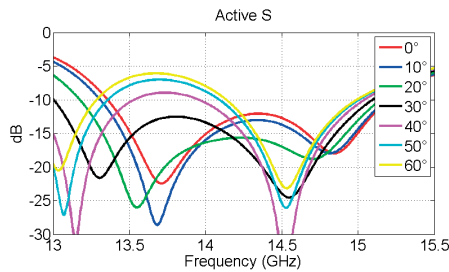
(a) Broadside Radiation Pattern for the 2x2 Tx-Band array (plane $\Phi = 0$).



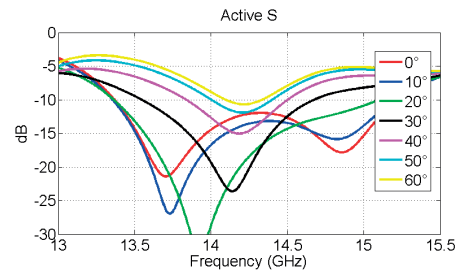
(b) S parameters seen from port 1, taken as a reference.



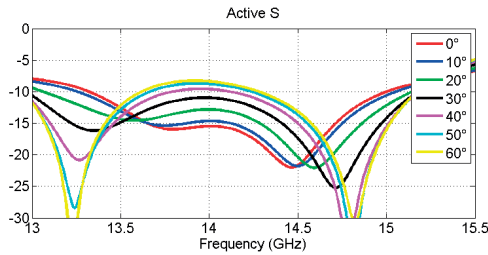
(c) Axial Ratio for the 2x2 Tx-Band array (plane $\Phi = 0$).



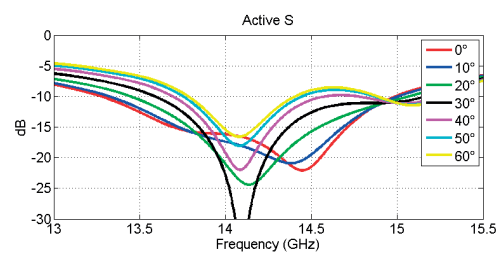
(d) Active S parameter seen from port 1 for various steering angles (RHCP).



(e) Active S parameter seen from port 2 for various steering angles (RHCP).



(f) Active S parameter seen from port 1 for various steering angles (LHCP).



(g) Active S parameter seen from port 2 for various steering angles (LHCP).

Figure 7.6: Simulated results for a 2x2 subarray surrounded by dummy patches (beam steering in the plane $\Phi = 0$).

7.3. Simplification of the element - 2x2 subarray

Table 7.2: Dimensions for the 2x2 subarray in Tx-Band.

parameter	value	unit
50Ω input line width	0.45	mm
Aperture radius	1.9	mm
Aperture width	0.5	mm
Stub lengths	0.85	mm
Radius of Wilkinson adapter	1.35	mm
R1	3	mm
Gap for Wilkinson resistor	1	mm
Patch radius	3.7	mm
Radius of cavity	5	mm
Hybrid branch width W	0.8	mm
Hybrid branch length L	3.5	mm
d1	5.15	mm
d2	3.5	mm
meander size	0.5	mm
miter bend size	0.45	mm
Distance between elements	11	mm

The simulation results visible in Fig. 7.6 -for the plane $\Phi = 0^\circ$, in which the electronic scanning will take place- show a broadside radiation pattern corresponding to our usual expectations (monotonous and symmetrical with a peak value around 9.5-10dBi). The AR is kept much below 3dB for all angles up to 60° , but seems to degrade quickly beyond this value. Yet, this AR profile is only valid for a broadside radiation of a 2x2 isolated subarray, with a radiation that is anyway negligible around 60° and beyond. One can expect the AR to be improved for a much larger array when the beam is indeed steered towards 60° .

Regarding the S and Active S parameters a thorough discussion is now necessary. The geometrical parameters corresponding to the plots in Fig. 7.6 are given in Table 7.2, and they are the result of an optimization on the stub length, aperture size and patch radius in CST. Our goal is to ensure that the Active S parameter seen from an element -which depends in a complex manner on the mutual couplings- would ideally be kept below -10dB for :

- All steering angles from 0° to 60°
- For both circular polarizations
- For both antenna accesses (they do not see the same environment when the beam is being steered as they are rotated of 90°)

Chapter 7. The particular case of a narrow bandwidth

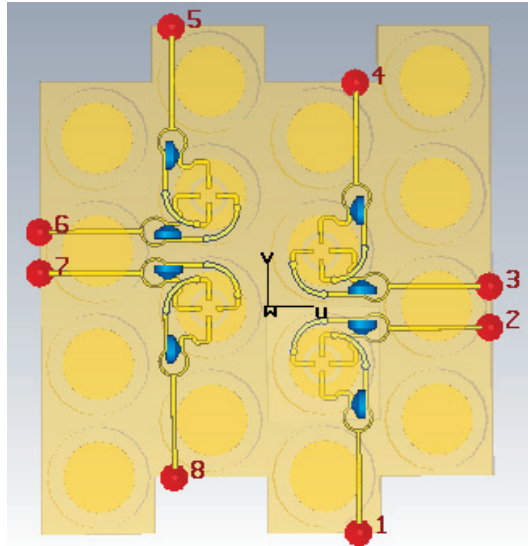
For instance, the broadside RHCP Active S parameter from the point of view of port 1 is given by :

$$Active_S = S_{11} + j * (S_{12} + 2 * S_{13}) - 2 * S_{14} - 4 * S_{15} - 4j * S_{16} - 2j * S_{17} + 2 * S_{18}$$

If the polarization is changed to LHCP, the signs of some of the terms have to be changed. For different steering angles, it is also necessary to multiply some of the terms by a proper complex phase term. Finally, the point of view of port 2 is obtained by a proper permutation of indices. This results in four complicated sums that depend on both frequency and steering angle, and it is unlikely that a perfect solution would be obtained.

After having explored many solutions in CST, we post-processed the variation of the Active S parameter in Matlab and we found the tradeoff presented in Fig. 7.6. The Active S parameters remain below -10dB most of the time; a prototype has been issued for this subarray in order to validate all these simulations (This prototype is not measured at the moment these lines are being written).

The only general way to obtain a low Active S parameter independently of the frequency and the steering angle is obviously to decrease all the S parameters as much as possible. Getting all of them as low as -20dB or even more is a usual target for engineers; it makes sense due to the fact that even relatively low values like -15dB (corresponding to our worst parameter, S_{18}) can cause high variations in a complex sum involving several terms, multiplied by two or four and raised to the square.



(a) Top view of a subarray using a triangular lattice approach.

7.3. Simplification of the element - 2x2 subarray

Unfortunately we did not find an immediate way to decrease, for instance, S_{18} since it depends essentially on the inter-element distance that is fixed by the steering constraints. We already put a lot of efforts in surrounding each element with a metallic cavity at the expense of the bandwidth. Yet there exist a possible solution for future researches which consists in moving half of the lines of a half element length, as can be seen in Fig. 7.7a : it increases the distance between elements of *different lines*.

This so-called *triangular lattice* is known since a long time to be more efficient than its rectangular counterpart in that it suppresses a part of the grating lobes that could appear [16]. But this is not the property we are interested in now; we will rather point out a property that was only mentioned very recently as far as we know [88]. It says that the mutual coupling between elements of different lines will decrease of several decibels (as much as 5-6dB) due to this increase of the distance between them. Our explorations in this direction did not bring from now a better tradeoff than the one obtained for the rectangular lattice.

7.4 Some words about the Ka-Band

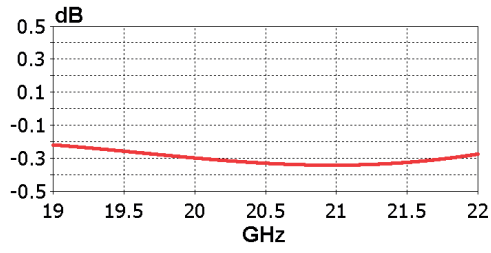
As was already mentioned earlier in this thesis, the narrow-band element developed around 14.25GHz can in principle be rescaled around 20GHz or 30GHz in order to cover both available Ka-band frequency bands. In this very short section, we provide the interested reader with provisional dimensions obtained for a rescale of the narrow-band element around 20GHz. They can be taken as a starting point in future projects to explore the Rx-Band.

Following our classical design pattern in several steps, we optimized in parallel the dimensions of an element with ideal excitation and the Wilkinson based feeding system. Then we plugged them together to create a complete element, and a 2x2 subarray. The dimensions are provided in table 7.3, and some results are reported in Fig. 7.7.

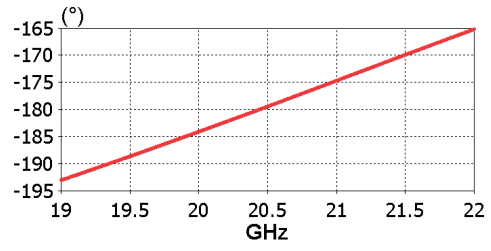
Two main difficulties were noticed, that we will report here for later researches; firstly, the vias used to bring the signal to the upper layer turn out to be very close to the cavity edges, which may have a negative impact. And it is not easy to move them away from each other. Secondly, some geometrical parameters (like the mitered bends or the via aperture radius) seem to be more sensitive to tolerances than they used to be for the 14.5GHz element.

Table 7.3: Dimensions for an element around 20GHz.

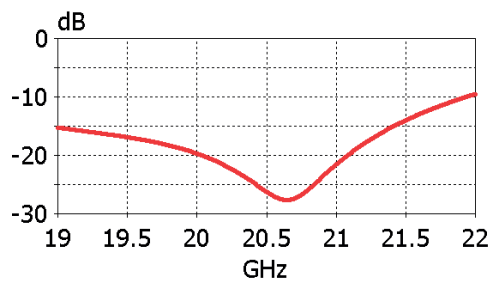
parameter	value	unit
Cavity height	1.5	mm
50Ω input line width	0.45	mm
Aperture radius	1.325	mm
Aperture width	0.5	mm
Via aperture radius	0.55	mm
Wilkinson radius	1.05	mm
Via pad radius	0.35	mm
Metallized holes radius	0.2	mm
Stub lengths	0.675	mm
Radius of Wilkinson adapter	1.35	mm
R1	3	mm
Gap for Wilkinson resistor	1	mm
Patch radius	2.575	mm
Radius of cavity	5	mm
Hybrid branch width W	0.8	mm
Hybrid branch length L	3.5	mm
d1	4	mm
d2	2.5	mm
meander size	1.05	mm
miter bend size	0.55	mm
Distance between elements	11	mm



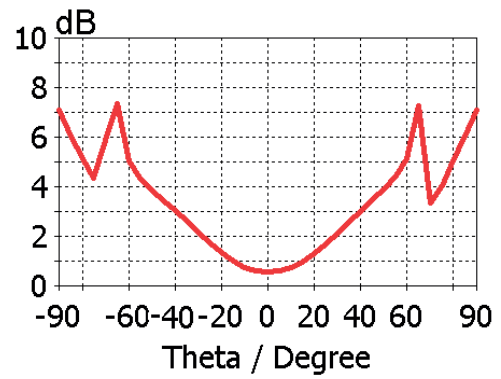
(a) Imbalance between both outputs of the Wilkinson coupler.



(b) Phase shift between both outputs of the Wilkinson coupler.



(c) Ideal Active S parameter.



(d) 2x2 Subarray AR.

Figure 7.7: Simulation results around 20GHz.

8 Numerical study of a graphene-based variable capacitor

Nature laughs at the difficulties of integration.

Pierre-Simon Laplace

As explained in chapter 2.3.2, variable capacitors can be implemented in phased arrays to create variable delay lines, also known as nonlinear delay lines (NDL) [28] [29]. Our obvious interest in these applications drives us in this final chapter to a research on the potentialities of graphene-based variable capacitors, although this is a research more related to theoretical physics and computational electromagnetics. Indeed, it turns out that the famous carbon-based material graphene could be used to produce varicaps at nanoscale, and the first step in their development is to make sure that they can be properly simulated. The LEMA laboratory is deeply involved in graphene research through its participation to the EU/EC *Graphene Flagship*, and is very experienced in Green's functions applied to 2D planar electromagnetic problems. The study of graphene-based capacitors is an interesting opportunity to apply this knowledge.

The presentation will be structured in four parts. First, the global idea will be explained and supported with a brief bibliography. Then, the most mathematical aspects of solving the Laplace equation in a general 2D electrostatics context will be explained. We will continue with a description of the Matlab code implementing the numerical resolution, and finally a full description of the benchmarks used to test its robustness will be given.

The ability to simulate graphene-based varicaps could also result in advances in other useful activities of the Graphene Flagship. This European-founded project is intended to support researches about this versatile and promising material, and the interested reader can find more informations on their official website (<http://graphene-flagship.eu/>).

8.1 A simplified theory of a quantum capacitor

Variable capacitors or varicaps have been used since many years for the design of sensors, which are applied in particular to bio or chemical sensing, either at micro-electronics or nano-electronics levels. They can act as transducers by exploiting the change of a capacitance under the interaction with a given type of molecules. For example in [89], a Nickel capacitor was built on a silicon substrate and a typical "interdigitated" shape was chosen for the design, as can be seen in Fig. 8.1a. With this topology, two sets of fingers that look like two "combs" are interwoven (without touching each other at any point) in such a way that the capacitance between the fingers is optimized.

A recent example of this structure involving this time graphene [90] is shown in Fig. 8.1b. It is described by their authors as "a first step in realizing graphene quantum capacitance varactors for wireless sensing applications". But before trying to simulate this exact type of structure -which is the final goal of the research- one should be able to understand and to solve the case of a simple rectangular shaped capacitor as depicted in Fig. 8.1c. If this type of capacitor could be well understood, then it would just be a matter of time to build and run a simulation on an arbitrarily more complex one.

The description thus starts with a sheet of graphene and a metallic plate of area \mathbf{A} , separated by a (thin) dielectric of thickness \mathbf{d} and permittivity ϵ . A fundamental question while solving a theoretical problem linked to capacitances is "What is the energy required to extract a carrier -say, here, an electron- from a conductor?". For all conductors there exist a certain amount of energy (called "work function" χ) that is needed to extract an electron from the conductor. For most materials χ has a constant value, but for graphene this value depends on the charge density already present on the material, and this phenomenon is the origin of an additional capacitive term not present in classical electrostatics. Let's assume that we move a small amount of charge dq from the PEC to graphene. We need to spend some energy $d\xi$, which is associated with a difference of potential :

$$d\xi = (\chi_g - \chi_m + E \cdot d)dq \quad \rightarrow \quad V = (\chi_g - \chi_m + E \cdot d)$$

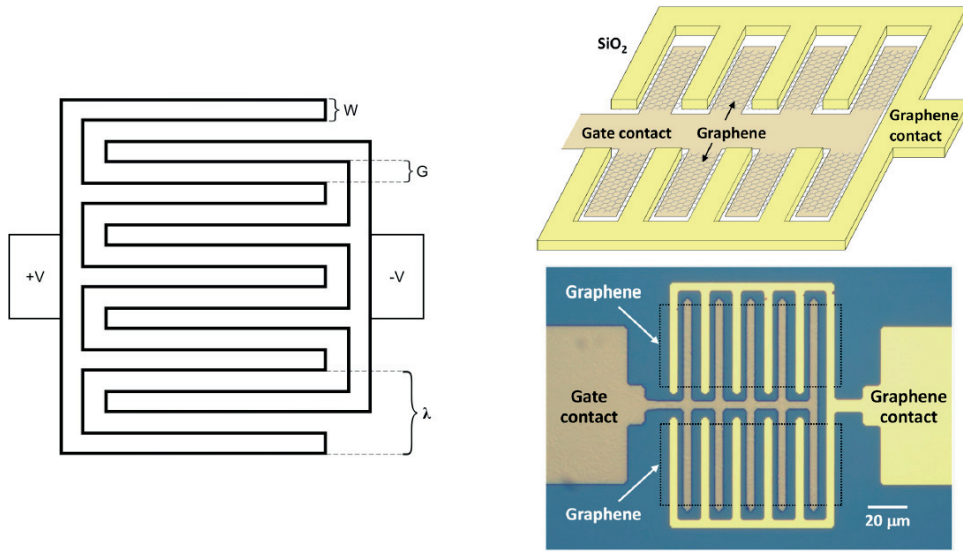
Where the subscripts \mathbf{g} and \mathbf{m} hold respectively for "Graphene" and "Metal", and \mathbf{E} is the electric field between the plates (assumed to be constant and perpendicular to them). The capacitance of the system for *small signals* is given by :

$$\frac{1}{C_{tot}} = \frac{\partial V}{\partial q} = \frac{\partial \chi_g}{\partial q} - \frac{\partial \chi_m}{\partial (-q)} + \frac{\partial E \cdot d}{\partial q}$$

For metals, χ_m is constant and hence the corresponding term vanishes. Regarding the term involving the electric field, the following classical relation holds (from Gauss's theorem) :

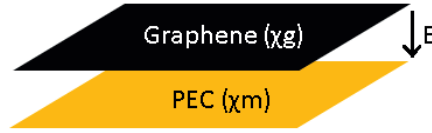
8.1. A simplified theory of a quantum capacitor

$$\frac{\partial E}{\partial q} = \frac{1}{\epsilon A}$$



(a) Interdigitated capacitor for sensors - courtesy of [89].

(b) Interdigitated capacitor using graphene - courtesy of [90].



(c) First simplified goal : a rectangular shaped capacitor with graphene.

Figure 8.1: Interdigitated capacitors and the introduction of graphene in this technology.

For graphene finally -and this is an important fact that is known by physicists but not implemented yet in simulators- χ_g changes and we have :

$$\frac{\partial \chi_g}{\partial q} = \frac{1}{A} \frac{\partial \chi_g}{\partial \rho} = \frac{1}{AC_q}$$

And thus the *small signal* capacitance is the series of the quantum and electrostatic capacitance :

$$\frac{1}{C_{tot}} = \frac{d}{\epsilon A} + \frac{1}{AC_q}$$

The quantum term is particularly interesting because it turns out to increase when the thickness of the substrate decreases; and it increases much faster than the electrostatic term, in

Chapter 8. Numerical study of a graphene-based variable capacitor

such a way that it dominates when the nanometer scale is reached. In order to observe and to manipulate this effect, it is possible to produce capacitors that would be etched on a silicon substrate ($\epsilon_r = 11.66$) with a thin layer of hafnium oxide (ϵ_r ranging from 20 to 30) separating the graphene sheet and the metallic part.

It is necessary to simulate this structure before building it, and one thus needs to model it properly as a 2D-infinite three layers system (the third layer is the vacuum). Then, applying a unitary differential voltage between both plates, one should be able to determine the charge distribution, from which the capacitance can be deduced. A classical and efficient way to solve such electrostatics problems is to use the so-called Method Of Moments, and to make its implementation as simple as possible.

In a nutshell, the idea consists in dividing -or meshing- the (continuous) unknown charge distribution (on the rectangular plates) in a finite set of unknown ponctual charges. Then, the potential at each point of the mesh can be expressed as a function of the unknown charges, and because the potential is fixed on the plates, a set of linear equation is obtained and the sought-after charge distribution is given by the inversion of a large linear system :

$$\begin{pmatrix} \dots & \dots & \dots \\ \vdots & IEMATRIX & \vdots \\ \dots & \dots & \dots \end{pmatrix} \begin{pmatrix} \vdots \\ \rho \\ \vdots \end{pmatrix} = \begin{pmatrix} \vdots \\ V \\ \vdots \end{pmatrix}$$

At least this is the case for a "classical" capacitor. For a quantum capacitor, the diagonal term must also be augmented with a new contribution :

$$\begin{pmatrix} \dots & \dots & \dots \\ \vdots & IEMATRIX & \vdots \\ \dots & \dots & \dots \end{pmatrix} \begin{pmatrix} \vdots \\ \rho \\ \vdots \end{pmatrix} = \begin{pmatrix} \vdots \\ V \\ \vdots \end{pmatrix} - \begin{pmatrix} \vdots \\ \frac{\rho}{C_q} \\ \vdots \end{pmatrix}$$

which can be written equivalently :

$$\left[\begin{pmatrix} \dots & \dots & \dots \\ \vdots & IEMATRIX & \vdots \\ \dots & \dots & \dots \end{pmatrix} + C_q^{-1} I \right] \begin{pmatrix} \vdots \\ \rho \\ \vdots \end{pmatrix} = \begin{pmatrix} \vdots \\ V \\ \vdots \end{pmatrix}$$

And in principle there is nothing more to be done. Matlab is a typical choice for writing such programs, especially because of the presence of efficient built-in functions for inverting linear systems. The only missing element which is not trivial at all is to be able to express the potential created by a source point charge at any other point in space. These terms constitute

8.1. A simplified theory of a quantum capacitor

the entries in the above matrices and are called the "Green's functions" of the system. They depend on the global structure, namely the substrate permittivities and thicknesses, and there expressions will be derived through a mathematically involved process in the next section.

Before going to the next practical step, we will briefly give a few justifications and explanations about this quantum self-term that appeared earlier. The theory of graphene capacitors is well described in a 2007 paper by Fang [91]. *et al.* and the reader is sent to this litterature for a deeper understanding of the underlying principles. It is not the point here to reproduce all the mathematical steps of the proof, so we will just report important milestones.

The differential capacitance is expressed by the rate of change of charge versus voltage :

$$C_q = \frac{dq}{dV} = \frac{d(pe - ne)}{d(\mu_c/e)} = e^2 \left(\frac{dp}{d\mu_c} - \frac{dn}{d\mu_c} \right)$$

e is the elementary charge, n and p are the charge negative and positive charge densities given by the famous Fermi-Dirac statistics :

$$\left\{ \begin{array}{l} n = \int_0^{\infty} \rho(E) f(E, \mu_c) dE \\ p = \int_{-\infty}^0 \rho(E) (1 - f(E, \mu_c)) dE = \int_0^{\infty} \rho(-E) f(E, -\mu_c) dE \\ f(E, \mu_c) = \frac{1}{1 + \exp(\frac{E - \mu_c}{k_B T})} \\ \rho(E) = \frac{2|E|}{\pi v_f^2 \hbar^2} \end{array} \right.$$

Where μ_c is the chemical potential, k_B the Boltzmann constant, T the temperature in Kelvins, and \hbar the reduced Planck constant.

Once the above formulas are injected in the expression for the capacitance, the derivation and the integration operation have to be swapped; then all the operations can be carried out and the resolution yields the following result :

$$C_q = \frac{2e^2 k_B T \ln(2(1 + \cosh(\frac{\mu_c}{k_B T})))}{\pi v_f^2 \hbar^2}$$

8.2 The Green's Functions of a point charge

In order to study the structure described in the previous section, a specific home-made code is then required. The Method of Moments (MoM) is at the same time the most accessible for LEMA students, due to the common cultural background of the laboratory, but also the most suitable for solving electrostatic problems involving this quantum effect that we are interested in. A typical MoM code is roughly splitted in two parts : first, we need a set of subroutines that can compute efficiently the Green's Functions for an elementary point charge, namely the potential that a point charge placed at some location in space will create at some other arbitrary location. Then, we need the core of the code, which will fill a Matrix with results of these computations and inverse this linear system to retrieve the charge distribution.

If the code is written in Matlab -which is the usual choice of LEMA researchers-, one can take advantage of built-in routines to invert large linear systems or to integrate functions. It is performed in an efficient but completely transparent way from the programmer's point of view, using respectively tools like matrix LU decomposition or Simpson's integration rules in the background. The main part of the work is then about computing these Green's Functions, and the present section is dedicated to this topic.

In vacuum, the Green's Function for the potential created by a point charge is simply given by the inverse of the distance between the charge and the observation point (up to some multiplicative constants). But in our model, two infinite and planar dielectric layers are added and they must be taken into account. Physically speaking, a surface polarization charge is induced by the presence of the source all over the dielectric interfaces, and finding the potential in this context is substantially more difficult than in the free space case.

Let us first begin with the recall that finding a Green's function in electrostatics means in practice solving the Laplace equation with given boundary conditions (here the presence of the dielectric interfaces and the point charge itself) :

$$\Delta V(x, y, z) = \left(\frac{\partial^2}{\partial x^2} + \frac{\partial^2}{\partial y^2} + \frac{\partial^2}{\partial z^2} \right) V(x, y, z) = 0$$

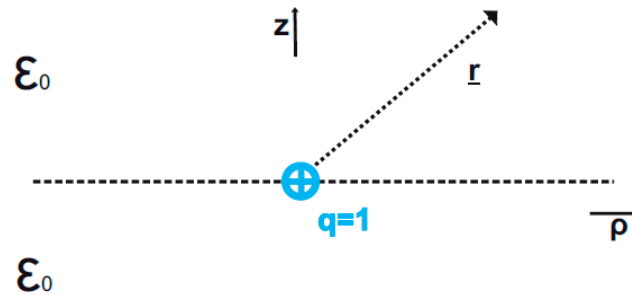
Finding a closed-form solution in the most general case is clearly hopeless, and we are thus bound to the use of more indirect methods. A classical resolution pattern is to apply the (2D) Fourier transform, which was historically developed for the purpose of solving differential equations :

$$\Delta \tilde{V}(x, y, z) = \frac{1}{2\pi} \int_0^\infty \int_0^\infty V(x, y, z) \exp^{jk_x x} \exp^{jk_y y} dx dy$$

8.2. The Green's Functions of a point charge

This transformation is linear and behaves in a clever way towards the derivation. In practice, it formally transforms the derivations into polynomial terms, and that's why we perform it on both x and y to "get rid" of both of them. For example with the x variable, we get :

$$\frac{\partial}{\partial x} \rightarrow j k_x x \quad , \quad \frac{\partial^2}{\partial x^2} = -k_x^2 x^2$$



(a)

Figure 8.2: Case of a point charge in vacuum - description and parameters.

Before going further in the resolution of the general problem, it is a good practice to apply the Fourier theory to the case of a point charge in vacuum, as described in Fig. 8.2a. A fundamental remark that will remain true all over this chapter, is that the infinite 2D multilayer system around a point charge presents an obvious azimuthal symmetry, which implies the use of polar coordinates for a simplified resolution. This remark is valid in both spatial and spectral domains as illustrated in Fig. 8.3a, and the following set of relations hold :

$$\left\{ \begin{array}{l} x = \rho \cos(\phi) \\ y = \rho \sin(\phi) \\ k_x = k_\rho \cos(k_\phi) \\ k_y = k_\rho \sin(k_\phi) \\ \rho = \sqrt{x^2 + y^2} \end{array} \right.$$

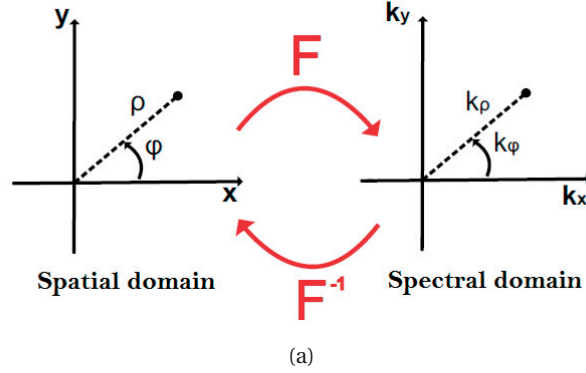


Figure 8.3: A 2D Fourier Transform with azimuthal symmetry, also called "Hankel Transform".

Two remarks will now motivate the previous operations. First, the change of coordinates implies a change in the Fourier transform, which becomes a "Fourier-Bessel" or "Hankel" transform :

$$\tilde{f}(k_x, k_y) = \frac{1}{2\pi} \int_{\phi=0}^{2\pi} \int_{\rho=0}^{\infty} f(\rho) \exp^{jk_\rho \rho \cos(k_\phi - \phi)} \rho \, d\rho \, d\phi$$

Because of the azimuthal symmetry, the first integral reduces to 2π . Moreover, the occurrence of the name of "Bessel" is not innocent here, due to the integral identity that appears and turns out to be known :

$$J_0(\omega) = \frac{1}{2\pi} \int_{\phi=0}^{2\pi} \exp^{j\omega \cos(\phi)} \, d\phi$$

Thus the Hankel transform and its inverse appear to be given by a pair of single improper integrals :

$$\tilde{f}(k_\rho) = \int_0^{\infty} J_0(k_\rho \rho) f(\rho) \rho \, d\rho$$

$$f(\rho) = \int_0^{\infty} J_0(k_\rho \rho) \tilde{f}(k_\rho) k_\rho \, dk_\rho$$

A second striking fact is that application of this Hankel transform to the Laplace equation yields :

$$(-k_x^2 - k_y^2 + \frac{\partial^2}{\partial z^2}) \tilde{V}(x, y, z) = (-k_\rho^2 + \frac{\partial^2}{\partial z^2}) \tilde{V}(x, y, z) = 0$$

8.2. The Green's Functions of a point charge

Namely a trivial second order differential equation in variable \mathbf{z} whose solutions in a homogeneous domain are written in the most general form as :

$$\tilde{V}(k_\rho, z) = A(k_\rho) \exp^{-k_\rho z} + B(k_\rho) \exp^{+k_\rho z}$$

Starting from now, we will employ the "Sommerfeld notation" $\lambda = k_\rho$, for the sake of respecting historical conventions. It appears that the resolution of the problem is in general divided in three steps :

- Defining a set of solutions with unknown coefficients as above, one for each homogeneous domain of space. In the case of a single charge located at the origin of the coordinate system, we will denote the $z > 0$ half-space with the subscript 1, and the $z < 0$ half-space with the subscript 2.
- Finding the coefficients with three types of boundary conditions : the necessity of a convergent solution at infinity, the continuity of the potential and the continuity of the electric field.
- Applying an inverse Hankel transform for retrieving the potential at a point in space domain. This very last step is most of the time only possible numerically.

There are two equations of type 8.2 and four coefficients A_1, B_1, A_2, B_2 to be found. Conditions at infinity imply quickly that $A_2 = B_1 = 0$. The continuity of potential at $z = 0$ implies $A_1 = B_2$. A single unknown A is now required and will be found with a little bit more subtle condition on the continuity of field at $z = 0$:

$$\begin{cases} \tilde{E}_{z1} = -\frac{\partial \tilde{V}_1}{\partial z} = \lambda A \exp^{-\lambda z} \\ \tilde{E}_{z2} = -\frac{\partial \tilde{V}_2}{\partial z} = \lambda A \exp^{+\lambda z} \end{cases}$$

$$\epsilon_0 (\tilde{E}_{z1} - \tilde{E}_{z2})_{z=0} = \tilde{\rho}_S \rightarrow A = \frac{q}{4\pi\epsilon_0\lambda}$$

For this last step, we used the fact that a point charge can be modeled by a Dirac distribution multiplied by the charge value q , and that the Fourier transform of such a distribution is a constant. We thus end up with the frequency domain solution :

$$\tilde{V} = \frac{q}{4\pi\epsilon_0} \frac{\exp^{-\lambda|z|}}{\lambda}$$

Chapter 8. Numerical study of a graphene-based variable capacitor

And coming back to the spatial domain, we find the famous "Sommerfeld identity" by identifying the inverse Hankel transform with the usual solution :

$$V(\rho, z) = \frac{1}{4\pi\epsilon_0 r} = \frac{1}{4\pi\epsilon_0 \sqrt{\rho^2 + z^2}}$$

$$\frac{1}{\sqrt{\rho^2 + z^2}} = \int_0^\infty J_0(\lambda\rho) \exp^{-\lambda|z|} d\lambda$$

Once this particular case is solved, the more complex situation of three dielectric layers, described in Fig. 8.4a can be tackled in principle in the same way.

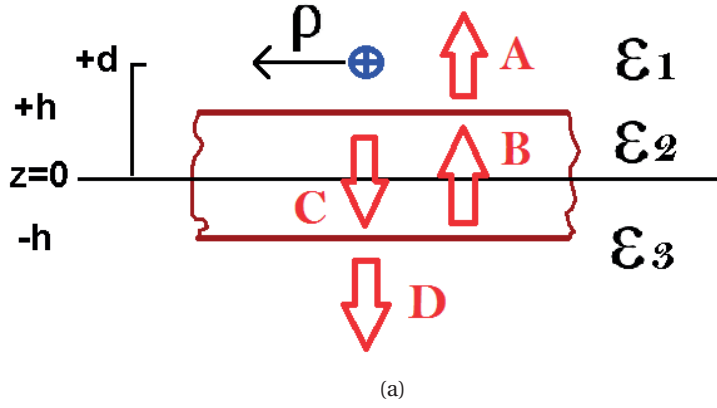


Figure 8.4: A point charge and three 2D-infinite dielectric layers; parameterization of the problem.

We start with the case where a charge is located in domain 1 (upper part) and we are looking for the potential in the rest of the space. In the three domains, the solution can be expected to be of the form :

$$\left\{ \begin{array}{l} \tilde{V} = \frac{\exp^{-\lambda|z-d|}}{\lambda} + A \exp^{-\lambda z} \\ \tilde{V} = B \exp^{-\lambda z} + C \exp^{+\lambda z} \\ \tilde{V} = D \exp^{+\lambda z} \end{array} \right.$$

Here we made use of the fact that the free space solution is already known to guess the form of the solution in the upper part of the space. Thus, "only" four coefficients have to be determined, with two conditions on the continuity of the potential at both interfaces, and two conditions on the field that are written as :

$$\begin{cases} \epsilon_1 \tilde{E}_{z1}(+h) = \epsilon_2 \tilde{E}_{z2}(+h) \\ \epsilon_2 \tilde{E}_{z2}(-h) = \epsilon_3 \tilde{E}_{z3}(-h) \end{cases}$$

All this can be summarized in a 4x4 system, and finding the coefficients is equivalent to inverting it :

$$\begin{pmatrix} -exp^{-\lambda h} & exp^{-\lambda h} & exp^{+\lambda h} & 0 \\ exp^{-\lambda h} & \frac{-\epsilon_2 exp^{-\lambda h}}{\epsilon_1} & \frac{\epsilon_2 exp^{-\lambda h}}{\epsilon_1} & 0 \\ 0 & exp^{\lambda h} & exp^{-\lambda h} & -exp^{-\lambda h} \\ 0 & \epsilon_2 exp^{\lambda h} & -\epsilon_2 exp^{-\lambda h} & \epsilon_3 exp^{-\lambda h} \end{pmatrix} \begin{pmatrix} A \\ B \\ C \\ D \end{pmatrix} = \begin{pmatrix} q \frac{exp^{-\lambda|d-h|}}{4\pi\epsilon_1\lambda} \\ q \frac{exp^{-\lambda|d-h|}}{4\pi\epsilon_1\lambda} \\ 0 \\ 0 \end{pmatrix}$$

There are some angles of attack to invert this system manually, but it would be pointless to do so. The best solution was to declare this system as a symbolic variable in Matlab and to invert it automatically; it resulted unsurprisingly in very cumbersome expressions, but they can be copied and reused directly inside Matlab subroutines for Green's Functions computation. The complexity of finding these constants is growing very fast while layers are being added to the system, and we reported the expression found for A,B,C, and D in the last appendix of this thesis.

Once these coefficients are obtained, we are in fact close to solving completely our engineering problem due to the two following remarks. Firstly, we don't need coefficients B and C, because the charges involved in the MoM resolution will always be located in graphene or metal (namely in the upper or bottom dielectrics) even though they are very close to the interface with the central dielectric. Secondly, if the source charge is located in the bottom substrate, we don't need to set up again a system and to invert it in Matlab, because of the symmetry of the system. One can deduce the proper formulas just by changing the signs of \mathbf{z} , \mathbf{d} , \mathbf{h} and by swapping ϵ_1 and ϵ_3 .

8.3 Global structure of a code implementing the Method of Moments

The Matlab code has been split in several files, and the best way to visualize its operation is to present it on a diagramm (Fig. 8.5). The file associated with the red color is the main one, while the green and yellow colors represent respectively debugging files and subroutines. We are going to give now a systematic review of each of them.

sym_inv.m and benchmark.m : The first file is just used once while inverting symbolically the quite complex system that gives the spectral Green's function coefficients; this was explained in detail in the previous section. The second file is a compilation of tests that call the Sommerfeld_quad function in different circumstances and plots the results in order to check their validity. It will be discussed in the next section.

Main.m : The core of the project. All the parameters are declared here, such as the dimensions of the square-shaped capacitor, the permittivities of substrates or the position of source charges and observation points for the Green's functions. The use of global variables was preferred to local ones in order to be able to access any information at any place in the code without having to manage too many arguments for the subroutines. It can be considered a good practice as long as the code keeps a reasonable size.

MoM.m : The Method Of Moments code itself. The capacitor that is solved from now by our software is simply made up of two rectangular plates, that are meshed as a cartesian lattice of point charges. The matrix can thus be decomposed in four blocks, that are fed in a double loop on x and y and concatenated just before the linear system inversion. The upper left block represents the "influence of the upper plate on itself" while the bottom right block represents the "influence of the bottom plate on itself". The diagonal blocks represent the influence on both plates on each other. If the capacitor topology is changed to a more complex shape -for instance, interdigitated fingers-, all the code modifications shall occur accordingly in this file.

In order to fill the matrix entries, the double loop repeatedly calls the Sommerfeld_quad function (described below). The only delicate part is about filling the so-called "self-term", the diagonal entry of the matrix composed of two contributions : firstly, the quantum contribution explained in the previous section, which is the most fundamental part and the core of this research. Secondly, there is always the classical electrostatic self-term modeling the influence of a point charge on itself. One could think of neglecting it completely, hoping that with a proper refinement of the mesh, its influence would tend to vanish. But this very rough approximation turned out to bring an instability effect while computing the capacitance, and so this problem had to be tackled anyway.

Studying this issue would be worth a chapter by itself, so we will stick to the following set of remarks : if the model of point charges is kept for assessing the self-term, an indeterminate

8.3. Global structure of a code implementing the Method of Moments

value is obtained due to the singularity. The model has to be refined, and a uniformly charged rectangle is considered instead. The searched-after value is then given by a complicated four-dimensional integral, which can be solved approximately, numerically or even with exact but cumbersome closed-form expressions; notable recent LEMA results in this domain are for example reported in [92] or [93]. A last technical detail is that the aforementioned solutions hold for self-terms computed in vacuum; in our case, the self-term corresponds to a charged rectangle at the interface between two dielectrics. In that case, the vacuum permittivity ϵ_0 should just be replaced by the mean permittivity $\frac{\epsilon_1 + \epsilon_2}{2}$; this intuitive idea can be fully justified by the generalized theory of images [94], that will be briefly reviewed in the next section.

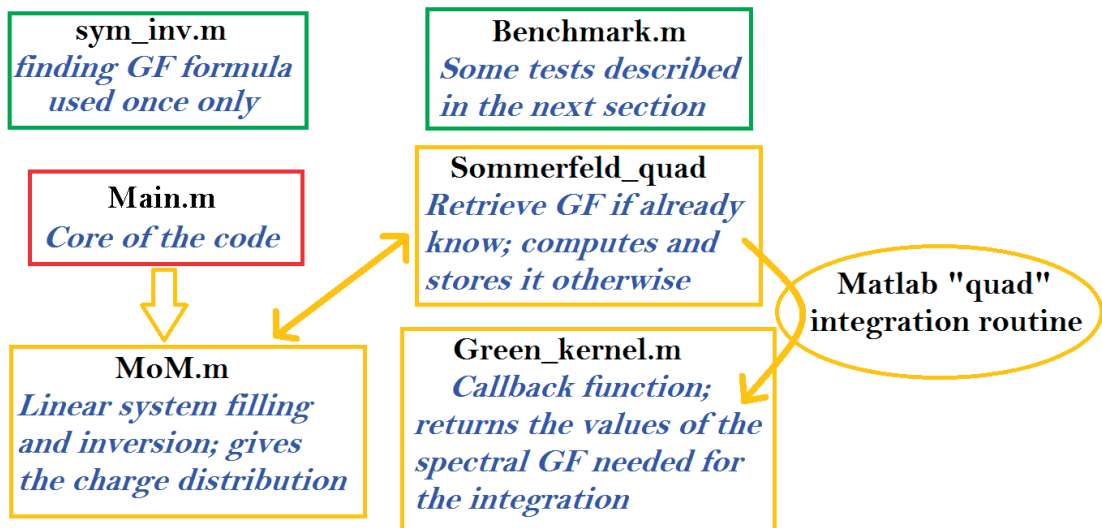


Figure 8.5: General structure of the Matlab code. In red : main file; in yellow : subroutines and arrows indicating the execution flow; in green : files only called during the preparation / debugging process.

Sommerfeld_quad.m : The subroutine implementing the computation of the inverse Hankel transform. Because of the Bessel function involved in it, the corresponding integral is oscillating and can be seen an alternate series. Knowing the zeroes of the Bessel function, the integral can be performed piece by piece thanks to the Matlab "quad" routine and summed, a process known as "integration then summation method". Theoretical works performed since the 1980s propose acceleration methods for extrapolating quickly the values of these integrals, but also for solving some divergences that may occur in the electrodynamic case; an account on the most recent developments is for example given by Mosig in [95]. Yet in the very simple electrostatic case solved here, and because computation times are not critical, these refinements have not been implemented and the code remains globally trivial.

The only highly important optimization included in this file stems from the following remark.

Chapter 8. Numerical study of a graphene-based variable capacitor

The Green's function are defined by the radial distance ρ between the source point and the observation point, as well as their vertical coordinates d and z . Most of the time, the Green's functions asked by the MoM.m file while filling the matrix are redundant, and one can get significative improvements if by storing the values corresponding to a triplet (ρ, d, z) after each new computation. When the function is called later, this database is first explored by a loop and the corresponding existing value can be returned immediately.

Green_kernel.m : This call-back function is passed as an argument to the Matlab "quad" routine, and called with a list of values required by the quadrature algorithm. It simply returns the spectral domain Green's function images (multiplied by the proper Bessel function) according to the formulas obtained with Hankel transforms.

8.4 Validation of the code with benchmarks

The MoM code analyzed over the two last sections was written "from scratch" using the theory of Hankel transforms and Sommerfeld integrals. It is supposed to perform computations on quantum capacitors that are not available anywhere else for comparison and validation purposes, either in commercial or in home-made softwares. On the other hand, the nanoscale prototyping process associated to these capacitors is very delicate and brings from now another level of uncertainty in the results. One would need to have a good deal of faith in both Matlab and Green's function theory to trust the pieces of code and the cumbersome formulas presented up to now, and to consider this software as a reference to validate -or not- experimental results. That's why a substantial amount of time was devoted to the elaboration of a set of benchmarks.

An ideal benchmark in our case would be a comparison between our MoM code and some relatively simple and trustful closed-form solution. Of course and as was mentioned before, no such expressions exist in general and that's why we went quite far into integral and differential calculus. But there is a quite simple approach to benchmarking this code : our numerical solution has to provide correct results in all particular situations that can be deduced from the most general case and solved analytically. We can classify them in three categories :

- If all the substrate tend to be the same (for instance, vacuum) the solution should reduce to a free space Green's function. Depending on the vertical position of the source and observation points (upper substrate, bottom substrate) a few first benchmarks are obtained. The variation of the potential with the radial distance from the origin is then our variable.
- If the central substrate tends to be equal to one of its neighbors, we are reduced to the case of a single dielectric interface, which can be solved with the generalized image theory as presented by Jackson in his reference book [94]. A lot of benchmarks can be derived from it, with various and random values for the substrate permittivities, the vertical position of the charge and of the observation points which can be taken to be very close to the interfaces (as will be the case with the capacitor) or rather far away from them.
- If the upper and bottom substrates tend to be the same, we get a dielectric slab inside a homogeneous material, which can be partially solved with a series according to a relatively recent result by Sometani [96].

Let us just make a brief recall about image theory. It is well known that an electric charge in the presence of an infinite ground plane can be replaced by the equivalent situation of two point charges of opposite signs, located in a symmetric way on both sides of the ground plane which is then remove. Following Jackson (see Fig. 8.6a) for the case of a single dielectric interface, one and also solve the Laplace equation in space domain (without any Hankel transform), and

Chapter 8. Numerical study of a graphene-based variable capacitor

using the boundary conditions at the interface find that the solution can be written thanks to the "virtual charges" and the formulas below. Here the q' charge replaces the original charge, and the q'' charge is its symmetric with respect to the interface, while R_1 and R_2 are simply the distance from source to observation points as they would be in free space.

$$\left\{ \begin{array}{l} q' = q \frac{\epsilon_1 - \epsilon_2}{\epsilon_2 + \epsilon_1} \\ q'' = q \frac{2\epsilon_2}{\epsilon_2 + \epsilon_1} \\ \Phi = \frac{1}{\epsilon_1} \left(\frac{q}{R_1} + \frac{q'}{R_2} \right), \quad z > 0 \\ \Phi = \frac{1}{\epsilon_2} \frac{q''}{R_1}, \quad z < 0 \end{array} \right. \quad (8.1)$$

$$\left\{ \begin{array}{l} \beta = \frac{\epsilon_2 - \epsilon_1}{\epsilon_2 + \epsilon_1} \\ q_{aan} = \beta^{2n-1} (-q_0) \\ q_{abn} = \beta^{2n} (-q_0) \\ q_{bbn} = \beta^{2n-1} (q_0) \\ q_{ban} = \beta^{2n} (q_0) \\ V_{aan} = \frac{q_{aan}}{4\pi\epsilon_0} \frac{1}{|z-a| + (2n-2)c+d} \\ V_{abn} = \frac{q_{abn}}{4\pi\epsilon_0} \frac{1}{|z-b| + (2n-1)c+d} \\ V_{bbn} = \frac{q_{bbn}}{4\pi\epsilon_0} \frac{1}{|z-b| + (2n-1)c+d} \\ V_{ban} = \frac{q_{ban}}{4\pi\epsilon_0} \frac{1}{|z-a| + (2n)c+d} \\ V = \frac{q}{4\pi\epsilon_1 |z-a+d|} + \sum_{n=1}^{\infty} V_{aan} + V_{abn} + V_{bbn} + V_{ban} \end{array} \right. \quad (8.2)$$

The case of the dielectric slab in a homogeneous media is more complicated, and was solved in 2000 by Sometani [96]. The situation is depicted in Fig. 8.6b : a point charge is placed outside the central dielectric slab, and we consider the axis perpendicular to the interfaces and crossing the charge. Then one can write the solution *on this axis* as an infinite series obtained from image theory (equation 8.2). This formula was particularly useful for observing if our code was robust for computing the potential when the source and observation points are both in the upper substrate, and when we approach the singularity of the charge from above or below.

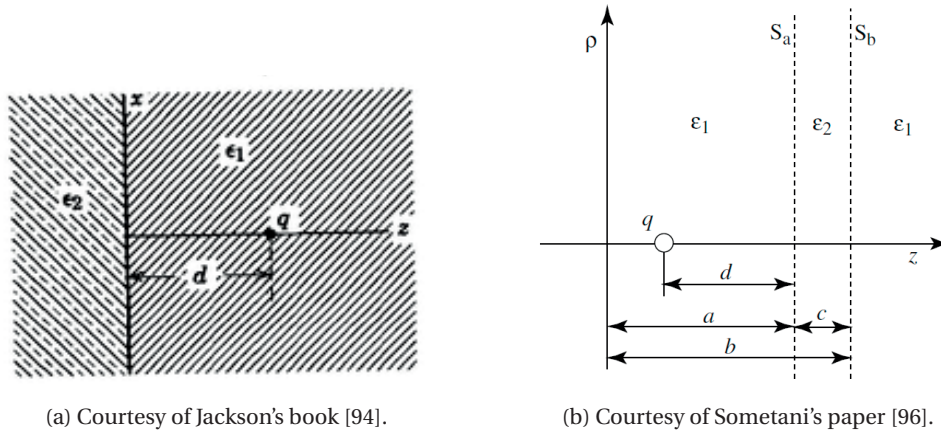


Figure 8.6: Illustration of Image Theory for a point charge near dielectric interfaces. The first case is a classical single-interface problem, the second case was solved more recently and consists of a dielectric slab in vacuum (double-interface).

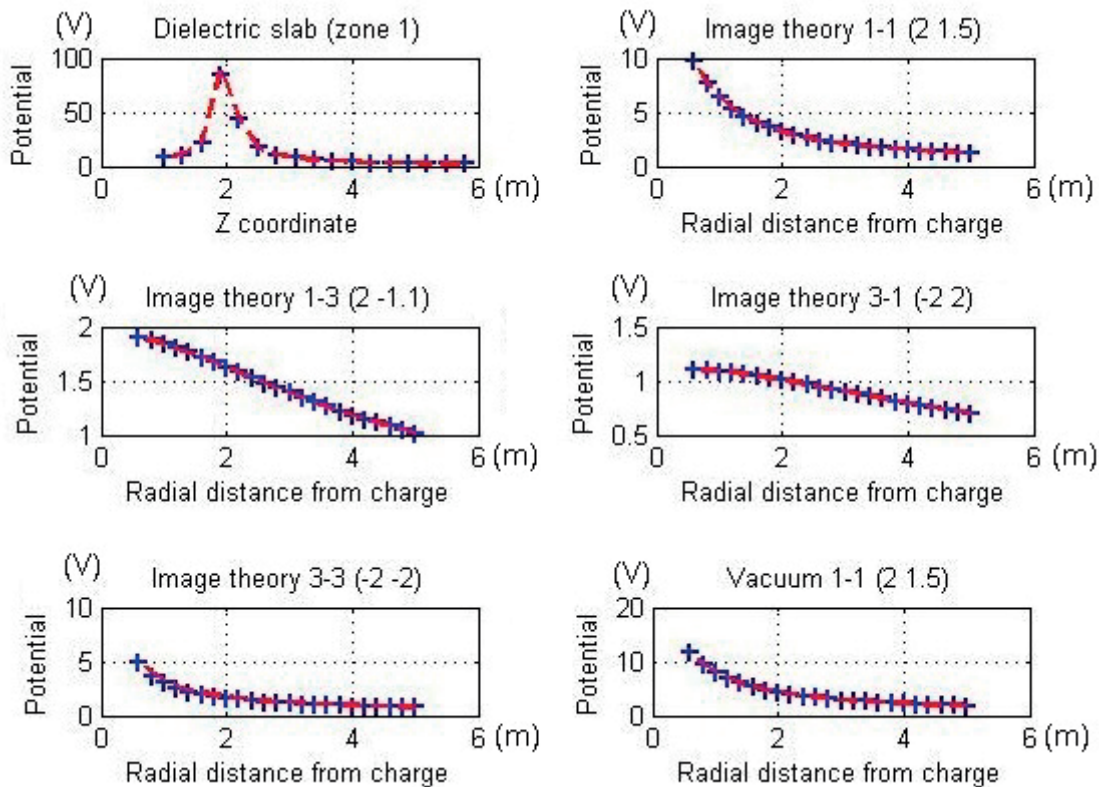
Table 8.1: Parameters and dimensions used for the Matlab benchmarks (comparing our code with image theory results).

Name	ϵ_1 (GHz)	ϵ_2 (GHz)	ϵ_3 (GHz)	d	h	z
Dielectric slab (zone 1)	1	2	1	2	1	-
Image theory 1-1 (2 1.5)	1	2	2	2	1	1.5
Image theory 1-3 (2 -1.1)	1	2	2	2	1	-1.1
Image theory 3-1 (-2 2)	1	3	3	-2	1	2
Image theory 3-3 (-2 -2)	1	3	3	-2	1	-2
Vacuum 1-1 (2 1.5)	1	1	1	2	1	1.5
Vacuum 1-3 (2 -0.5)	1	1	1	2	1	-0.5
Vacuum 3-1 (-1.5 1.5)	1	1	1	-1.5	1	1.5
Vacuum 3-3 (-1.5 -1.5)	1	1	1	-1.5	1	-1.5
Image theory 1-1 (2 1.5) second case	1	1	2	2	1	1.5
Image theory 1-3 (2 -1) second case	1	1	2	2	1	-1
Image theory 3-1 (-2 1.5) second case	1	1	3	-2	1	1.5
Image theory 3-3 (-2 -1) second case	1	1	3	-2	1	-1

Chapter 8. Numerical study of a graphene-based variable capacitor

Table 8.1 offers a summary of the 13 cases that have been tested and reported here, and the resulting plots are available in Fig. 8.7a. Please note that the units in these computations are not really important. What matters is to set them in such a way that no extreme values of any kind would appear in Matlab, resulting typically in warnings in the terminal and more and more approximate results. In this case we kept distances in meters, the elementary charge was a nano-Coulomb (nC) and the permittivities were multiplied by the usual value of ϵ_0 . Once the proper units are found for solving a problem at some scale, the programmer should just pay attention to these units while post-processing the MoM results.

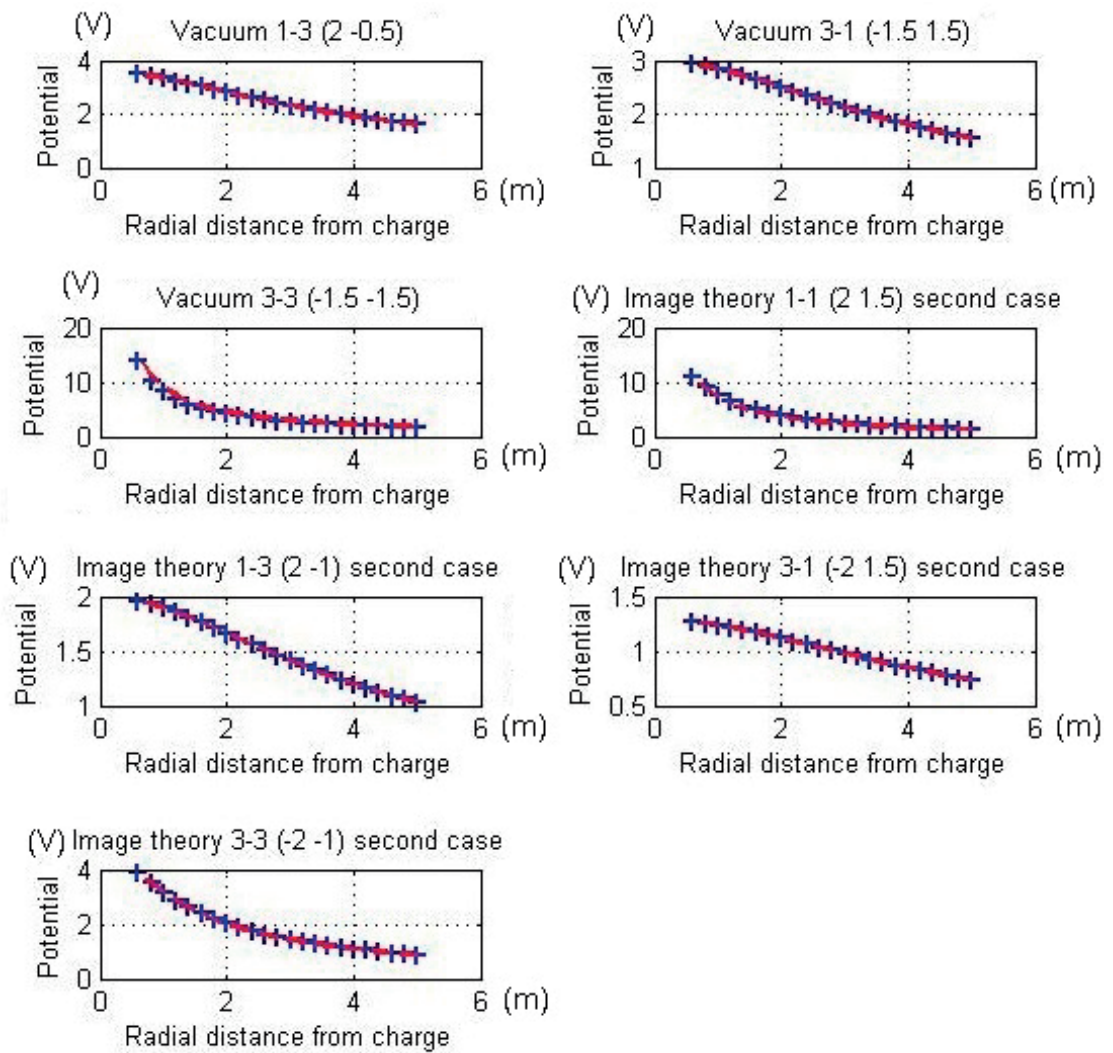
Besides these practical considerations, the curves are matching perfectly, even though it took quite a lot of time to correct all the bugs; most of the time they were trivial ones, while the apparently most complicated steps of programming or building the Green's functions. Yet it was necessary to implement many different tests, because it happened several times that some of them were working approximately or even perfectly, while some others were not at all.



(a)

Figure 8.7: Benchmarks for the Green's Function computation - Comparison between our code (in blue) and some particular closed-form results using image theory (in red). See table 8.1 for a description of each test performed.

8.4. Validation of the code with benchmarks



(a)

Figure 8.8: Benchmark plots (end).

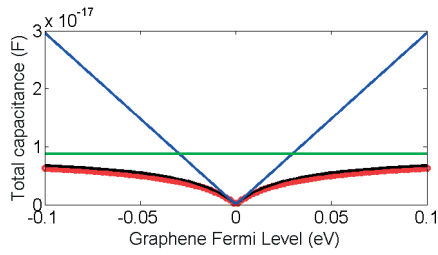
8.5 Simulation of a graphene capacitance

The proposed method of moments can be scaled to predict the behavior of nanometric structures where the quantum capacitance in graphene becomes relevant. In this example we consider two layers of graphene. The first layer is placed between the substrate dielectric (silicon, $\epsilon_r = 11.66$) and the gate oxide (hafnium oxide, $\epsilon_r = 20$), while the second one is placed on top of the gate oxide and air superstrate is assumed ($\epsilon_r = 1$). The two graphene patches have size of 50nm x 50nm and the thickness of the gate oxide is 10nm.

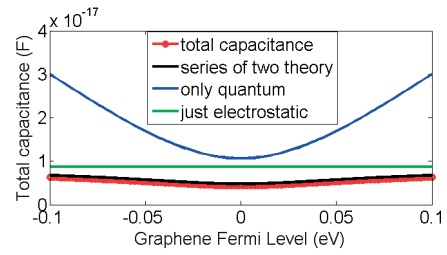
Figure 8.9a shows the capacity computation at temperature of 3K for different graphene Fermi levels. We see how quantum capacitance dominates close to the charge neutrality point. Figure 8.9b shows the capacity computation at temperature of 300K (room temperature), while figure 8.9c shows an intermediate case ($T=100K$). In these more realistic cases the graphene quantum capacitance is important but the effect of temperature limits the reconfigurability of the varactor.

Finally figure 8.9d and 8.9e represent charge density on the top plate of the varactor for Fermi levels of 0.01eV and 0.1eV respectively (3K in both cases). We notice that the charge density for the 0.1eV case takes a familiar shape seen in parallel plate capacitors, while for the 0.01eV case the charge density is lower and much more uniform. These effects are both due to the series quantum capacitance which dominates in this case, reducing the total capacitance and reducing the effect linked to the geometry of the conductor.

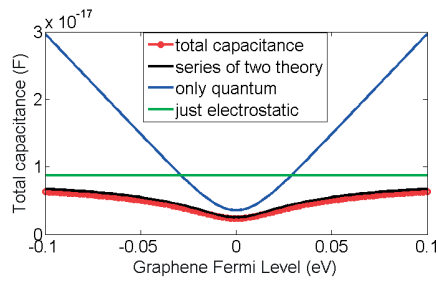
8.5. Simulation of a graphene capacitance



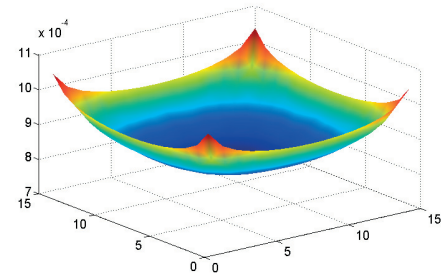
(a) Capacity at 3K for different graphene Fermi levels.



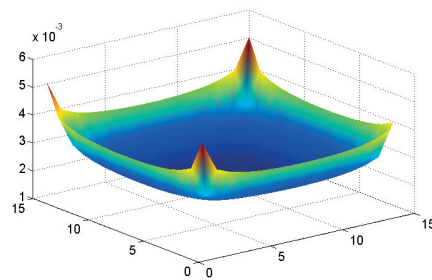
(b) Capacity at 300K for different graphene Fermi levels.



(c) Capacity at 100K for different graphene Fermi levels.



(d) Charge density distribution on the top plate (0.01eV).



(e) Charge density distribution on the top plate (0.1eV).

Figure 8.9: Simulations on nanometric structures using our MoM code.

8.6 Final example and conclusion

Finally we validated the code with an example of tridimensional structure, namely a parallel plane capacitor where one or both the plates includes quantum capacity effects. We first computed the classical method of moment matrix using the aforementioned method, and then we added the quantum capacity term and solved the system. For this first test we validated the code using arbitrary and varying values of the quantum capacity of the plate, while keeping the geometry unchanged.

The reason is to illustrate an important property of quantum capacity: for lower quantum capacity values the quantum capacity dominates on the electrostatic term, a condition which is desirable for varicaps, the quantum capacity being tuneable. Fig. 8.10 shows the total capacitance of the parallel plate system as a function of the quantum capacitance of the plates. For large values of the quantum capacitance the total capacitance tends to the electrostatic limit, while for small values the expected behavior predicted above is observed.

In this example, we see that in the low region of quantum capacitance the total capacitance of the device could be easily tuned within at least one order of magnitude (10-100pF). This is an excellent prospect for using this varicap as a control element in an antenna array.

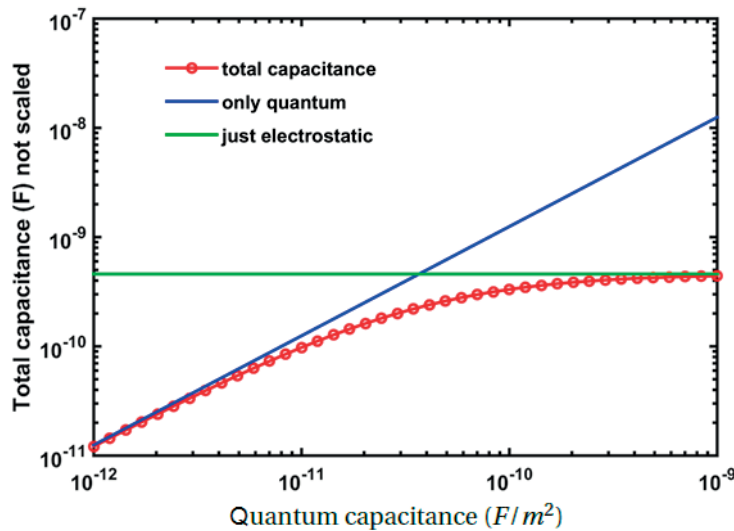


Figure 8.10: Evolution of the complete capacitance vs quantum capacitance.

9 Conclusion and perspectives

I hope that posterity will judge me kindly, not only as to the things which I have explained, but also to those which I have intentionally omitted so as to leave to others the pleasure of discovery.

René Descartes

The present work contains an overview of the design of several antenna elements and small subarrays intended for low-profile phased array antennas. The main target was the reception of Internet through SATCOM links, which involved the use of the 10.7GHz-12.7GHz Band (located across the X and Ku Bands). The case of the transmission band (14GHz-14.5GHz) was treated separately, due to the fact that two different antenna arrays can be considered for uplink and downlink. This approach simplifies the design, especially because the bandwidth required for the Tx-Band alone is narrow. During the last year of the thesis, there was also a growing interest in K/Ka-Band services. The possibility of rescaling the 14GHz narrow band antenna element towards 20GHz was discussed.

The desired antenna array should fulfill many stringent requirements at the same time. It must be low-profile and highly directive, but also able to steer the beam with accuracy far away from the broadside, while handling high quality dual-circular polarization. The dual circular polarization was treated successfully, but it turned out that designing proper antenna elements for narrow bandwidth -either for the Tx-Band or at higher frequencies in K/Ka-Band- was much easier than for the Rx-Band. This is due to the fact that the mutual coupling between neighboring elements became quickly a serious problem, that was successfully mitigated with the use of metallic cavities. Yet these cavities reduce the bandwidth and the strategy can be used only for antenna elements having a relatively low bandwidth.

An important aspect in this thesis was the manufacturing of various prototypes to validate the simulated concepts. The corresponding PCB layers have been produced in our EPFL

Chapter 9. Conclusion and perspectives

workshop, while the assembling operation, the soldering of discrete components and the mounting of the connectors have been performed manually. Although it can cause some uncertainties in the results, it also brings an invaluable practical knowledge to the PhD student and more control on the whole production process. In particular the dual-circularly polarized Rx-Band and Tx-Band planar antenna elements gave a fully satisfactory operation in terms of both impedance matching and radiation.

In the future it would be possible to move the researches towards the K/Ka-Bands for the following reasons. Firstly, as was mentioned before, the relative bandwidths required are lower than their Ku-Band counterparts (at least the Rx one) and it brings a considerable simplification to the design. Secondly, the requirements in terms of polarization are less constraining in these bands, because generating a single circular polarization at a time is enough, provided that we can switch from right-handed to left-handed. In particular, it would not be necessary anymore to use an advanced and complex directional coupler solution as the one that was presented in chapter 3.

In a general manner, it seems that there is an increasing interest for Ka-Band both from the point of view of research laboratories and industry actors. The idea that manufacturing antennas for higher and higher frequencies becomes more and more difficult because of fabrication tolerances is not wrong, but we are convinced that one should not be afraid of deploying antennas in Ka-Band for that reason.

A few words can be said about the last chapter of this thesis, which deserves a different treatment. It was dedicated to the numerical simulation of infinite 2D layered structures involving Graphene. The goal of this research was to model varicaps based on a quantum effect specific to Graphene structures. It involved the use of the Method of Moments and of electrostatic Green's functions, a topic that belongs to the traditional knowledge of the LEMA laboratory. This is a very prospective research but it is hoped that the obtained results will be useful in future antenna array designs when the graphene technology will reach full maturity thanks to projects like the EC Graphene Flagship.

A Appendix 1 : Microwave connectors.

The experimental aspect of microwaves often represents a challenge, sometimes even more than the theoretical aspect. The discrepancies between measured and simulated results, especially the degraded quality of S parameters or radiation properties of some circuit or antenna, stem from a various set of sources. During this thesis, three of them have been identified as potential recurrent issues :

- Chemical etching tolerances. Depending on the configuration (thickness of metal of the substrate, presence of metallized holes or not), the width of manufactured microstrip lines can be a few tens of microns below what was expected; this is due to the fact that acid tends to attack slightly the sides of lines during the etching process.
- Air gaps or bad contacts between layers in a stackup circuit.
- Bad contact of RF connectors at the edges of the PCB microstrip circuits.

The first problem often doesn't matter cause much trouble, because most of the lines (or holes) are large compared to the tolerances (a few hundreds of microns compared to a few tens). Lines down to 200 microns of width can be done at EPFL with a reasonable accuracy. When these orders of magnitude are reached anyway, one can for example increase in advance the width of the line in order to compensate this effect. On the other hand, the second problem is a purely practical one, which depends on many factors such as the glues that are used or the care that is taken for assembling layers.

The last issue in the list, namely the placement of connectors, can have a surprisingly bad impact on the operation of a microwave circuit; that's why we decided to include an appendix about this topic which becomes time consuming if it is not immediately and properly taken into account.

While people are working at relatively low frequencies, which means up to a few Gigahertz, few attention can be paid to connectors because they won't influence the measurements as

Appendix A. Appendix 1 : Microwave connectors.

long as they are soldered in a clean way. But whenever a circuit is operating in Ku-Band, or even in Ka-Band, the reflections cause by a poor contact impact directly on S parameters. And if there are several connectors, and structures such as directional coupler that require good matching at their ends to operate properly, mismatches can lead to standing waves or any kind of parasitic effects that even impact on the radiation.

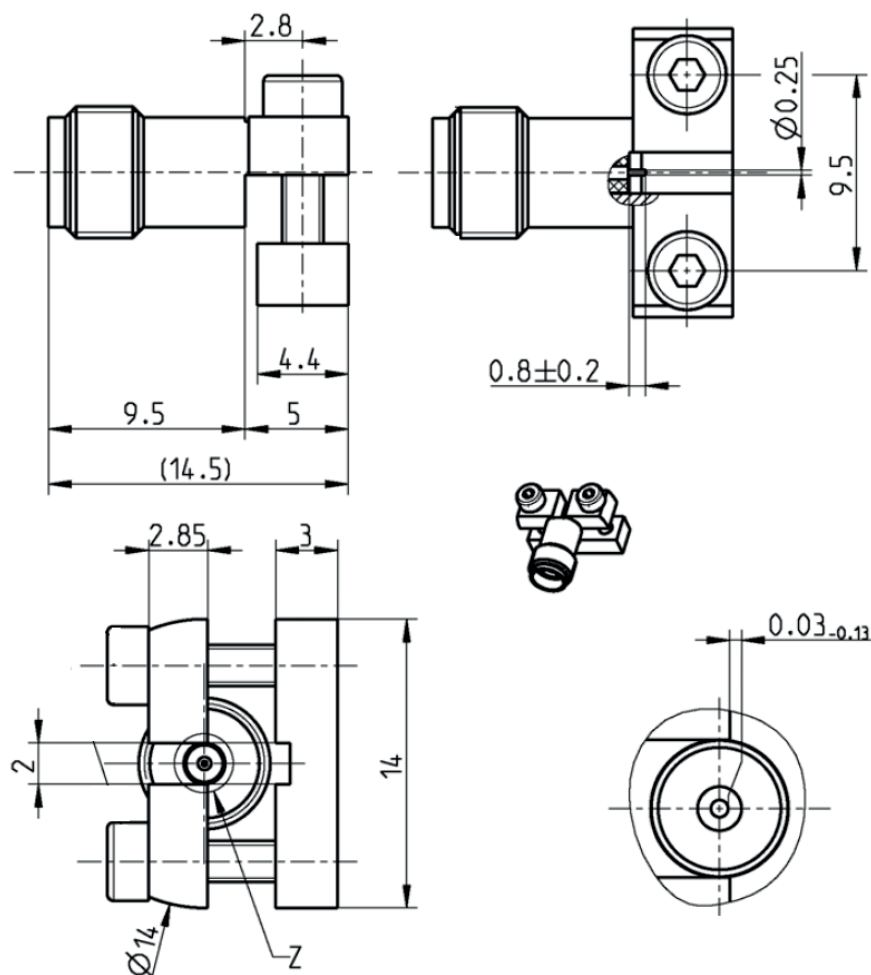
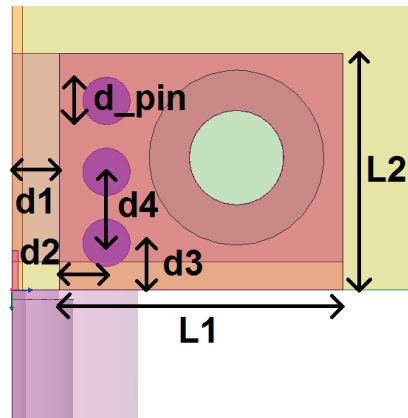


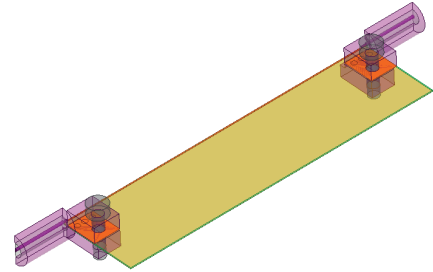
Figure A.1: Rosenberger connector dimensions extracted from the datasheet (SMA JACK PCB 32K243-40ML5).

In order to make an efficient use of connectors, the following steps have to be followed:

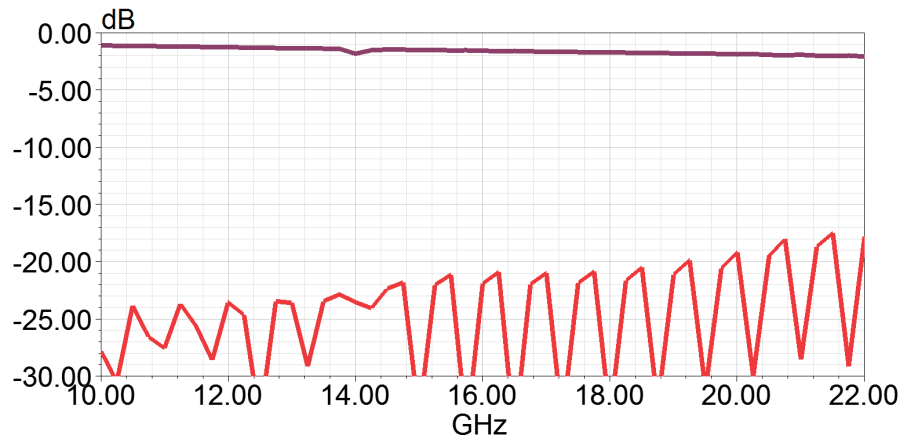
- A proper connector has to be bought first, which seems obvious but deserves already to be mentioned. It is not only necessary to check the frequency range in the datasheet, but one should also pay attention to the type of connector that is chosen.
- The second step consists in preparing a correct and custom "footprint" to optimize the contact. A full description is given below.



(a) Footprint for a Rosenberger connector and its parameters (Top view of HFSS model).



(b) HFSS model for a couple of Rosenberger connectors (perspective view).



(c) Best S parameters obtained for a couple of Rosenberger connectors (Ku-band + lowest part of Ka-Band - 0.203mm RO4003C substrate).

Figure A.2: Rosenberger connectors studied with HFSS.

For microstrip feedings, the best choice turns out to be connectors with screws that can be "clamped" around the substrate : these are more stable from a mechanical point of view, they can be unmounted as many times as required and they require no soldering, which could introduce random parasitic effects. A typical Ku-Band reference that matches these requirements is the 32K243-40ML5 SMA PCB JACK by Rosenberger, and all the prototypes that will be presented in this thesis have been built with this one. Some views and dimensions from the datasheet are reported in Fig. A.1. A footprint associated to this connector, as mentioned in the second point above, means a set of metallized pads and holes to ensure a contact between the upper metallic part of the connector and the ground plane.

Thanks to a discussion with Rosenberger, a .sat model file was obtained for it, and a HFSS project was set up to simulate a pair of connectors around a microstrip line. One can see it on Fig. A.2b, or rather half of it because a symmetry operation was applied for accelerating the simulation. The footprint suggested and modeled is depicted in Fig. A.2a : it consists

Appendix A. Appendix 1 : Microwave connectors.

Table A.1: Geometrical parameters for an optimized Rosenberger connector footprint.

Parameter	value (mm)
d1	1
d2	1
d3	1
d4	1.5
d_pin	1
L1	6
L2	5

in a rectangular with a hole for the screw, and three metallized holes aligned close to the feeding line that act as short circuit between the connector and the ground plane. The optimal dimensions depend on the targetted frequency range, but also to a larger extent to the substrate used.

The optimal parameters were found thanks to a parametric sweep in HFSS. The starting values were given by Rosenberger from a previous optimization that was performed for another customer, with a different layer stackup. The dimensions are reported in table A.1.

B Appendix 2 : Green's function.

The complete expressions for the Green's functions coefficients in spectral domain are reported here.

$$A = (q \cdot \exp(-\lambda \cdot \text{abs}(d - h)) \cdot \exp(h \cdot \lambda) \cdot (\epsilon_2 - \epsilon_3 + \epsilon_2 \cdot \exp(4 \cdot h \cdot \lambda) + \epsilon_3 \cdot \exp(4 \cdot h \cdot \lambda))) / (4 \cdot \pi \cdot \lambda \cdot (\epsilon_1 \cdot \epsilon_2 - \epsilon_1 \cdot \epsilon_3 + \epsilon_2 \cdot \epsilon_3 + \epsilon_2^2 \cdot \exp(4 \cdot h \cdot \lambda) - \epsilon_2^2 + \epsilon_1 \cdot \epsilon_2 \cdot \exp(4 \cdot h \cdot \lambda) + \epsilon_1 \cdot \epsilon_3 \cdot \exp(4 \cdot h \cdot \lambda) + \epsilon_2 \cdot \epsilon_3 \cdot \exp(4 \cdot h \cdot \lambda))) - (q \cdot \exp(-\lambda \cdot \text{abs}(d - h)) \cdot \exp(h \cdot \lambda) \cdot (\epsilon_2 \cdot \epsilon_3 + \epsilon_2^2 \cdot \exp(4 \cdot h \cdot \lambda) - \epsilon_2^2 + \epsilon_2 \cdot \epsilon_3 \cdot \exp(4 \cdot h \cdot \lambda))) / (4 \cdot \pi \cdot \epsilon_1 \cdot \lambda \cdot (\epsilon_1 \cdot \epsilon_2 - \epsilon_1 \cdot \epsilon_3 + \epsilon_2 \cdot \epsilon_3 + \epsilon_2^2 \cdot \exp(4 \cdot h \cdot \lambda) - \epsilon_2^2 + \epsilon_1 \cdot \epsilon_2 \cdot \exp(4 \cdot h \cdot \lambda) + \epsilon_1 \cdot \epsilon_3 \cdot \exp(4 \cdot h \cdot \lambda) + \epsilon_2 \cdot \epsilon_3 \cdot \exp(4 \cdot h \cdot \lambda)))$$

$$B = (q \cdot \exp(-\lambda \cdot \text{abs}(d - h)) \cdot \exp(h \cdot \lambda) \cdot (\epsilon_2 - \epsilon_3)) / (4 \cdot \pi \cdot \lambda \cdot (\epsilon_1 \cdot \epsilon_2 - \epsilon_1 \cdot \epsilon_3 + \epsilon_2 \cdot \epsilon_3 + \epsilon_2^2 \cdot \exp(4 \cdot h \cdot \lambda) - \epsilon_2^2 + \epsilon_1 \cdot \epsilon_2 \cdot \exp(4 \cdot h \cdot \lambda) + \epsilon_1 \cdot \epsilon_3 \cdot \exp(4 \cdot h \cdot \lambda) + \epsilon_2 \cdot \epsilon_3 \cdot \exp(4 \cdot h \cdot \lambda))) + (q \cdot \exp(-\lambda \cdot \text{abs}(d - h)) \cdot \exp(h \cdot \lambda) \cdot (\epsilon_1 \cdot \epsilon_2 - \epsilon_1 \cdot \epsilon_3)) / (4 \cdot \pi \cdot \epsilon_1 \cdot \lambda \cdot (\epsilon_1 \cdot \epsilon_2 - \epsilon_1 \cdot \epsilon_3 + \epsilon_2 \cdot \epsilon_3 + \epsilon_2^2 \cdot \exp(4 \cdot h \cdot \lambda) - \epsilon_2^2 + \epsilon_1 \cdot \epsilon_2 \cdot \exp(4 \cdot h \cdot \lambda) + \epsilon_1 \cdot \epsilon_3 \cdot \exp(4 \cdot h \cdot \lambda) + \epsilon_2 \cdot \epsilon_3 \cdot \exp(4 \cdot h \cdot \lambda)))$$

$$C = (q \cdot \exp(-\lambda \cdot \text{abs}(d - h)) \cdot \exp(3 \cdot h \cdot \lambda) \cdot (\epsilon_2 + \epsilon_3)) / (4 \cdot \pi \cdot \lambda \cdot (\epsilon_1 \cdot \epsilon_2 - \epsilon_1 \cdot \epsilon_3 + \epsilon_2 \cdot \epsilon_3 + \epsilon_2^2 \cdot \exp(4 \cdot h \cdot \lambda) - \epsilon_2^2 + \epsilon_1 \cdot \epsilon_2 \cdot \exp(4 \cdot h \cdot \lambda) + \epsilon_1 \cdot \epsilon_3 \cdot \exp(4 \cdot h \cdot \lambda) + \epsilon_2 \cdot \epsilon_3 \cdot \exp(4 \cdot h \cdot \lambda)))$$

Appendix B. Appendix 2 : Green's function.

$$\begin{aligned} & \epsilon_3 + \epsilon_2\epsilon_3 + \epsilon_2^2\exp(4h\lambda) - \\ & \epsilon_2^2 + \epsilon_1\epsilon_2\exp(4h\lambda) + \epsilon_1\epsilon_3\exp(4h\lambda) + \epsilon_2\epsilon_3\exp(4h\lambda) \\ & + (q\exp(-\lambda|d-h|)\exp(3h\lambda)(\epsilon_1\epsilon_2 + \epsilon_1\epsilon_3)) / (4\pi\epsilon_1\lambda(\epsilon_1\epsilon_2 - \epsilon_1\epsilon_3 + \epsilon_2\epsilon_3 + \epsilon_2^2\exp(4h\lambda) - \epsilon_2^2 + \epsilon_1\epsilon_2\exp(4h\lambda) + \epsilon_1\epsilon_3\exp(4h\lambda) + \epsilon_2\epsilon_3\exp(4h\lambda))) \end{aligned}$$

$$\begin{aligned} D = & (\epsilon_2q\exp(-\lambda|d-h|)\exp(3h\lambda)) / (\pi\lambda(\epsilon_1\epsilon_2 - \epsilon_1\epsilon_3 + \epsilon_2\epsilon_3 + \epsilon_2^2\exp(4h\lambda) - \epsilon_2^2 + \epsilon_1\epsilon_2\exp(4h\lambda) + \epsilon_1\epsilon_3\exp(4h\lambda) + \epsilon_2\epsilon_3\exp(4h\lambda))) \end{aligned}$$

Bibliography

- [1] Roberto Torres Sanchez. *Analysis and Design of a Planar Radiating Element for Automotive Satellite Broadcasting Reception Systems*. PhD thesis, Ecole Polytechnique Fédérale de Lausanne, 2011.
- [2] M.A. Antoniadou and G.V. Eleftheriades. A metamaterial series-fed linear dipole array with reduced beam squinting. In *Antennas and Propagation Society International Symposium 2006, IEEE*, pages 4125–4128, July 2006.
- [3] Leonard Thomas Hall. *Broadband Monolithic Constrained Lens Design*. PhD thesis, The University of Adelaide, Australia, 2009.
- [4] J. Perruisseau-Carrier, R. Fritschi, P. Crespo-Valero, and A.K. Skrivervik. Modeling of periodic distributed mems-application to the design of variable true-time delay lines. *Microwave Theory and Techniques, IEEE Transactions on*, 2006.
- [5] Masayoshi Aikawa Toshiaki Tanaka, Kikuo Tsunoda. Slot coupled directional couplers on a both sided substrate mic and their applications. *Electronics and communications in Japan*, 1989.
- [6] Sener Uysal Chelsia Lim. Design of a broadband directional coupler using microstrip-like multilayer technology. *Microwave and optical technology letters*, 1999.
- [7] Marek Bialkowski Amin Abbosh. Design of compact directional couplers for uwb applications. *Microwave theory and techniques, IEEE Transactions on*, 2007.
- [8] K. Woelder and J. Granholm. Cross-polarization and sidelobe suppression in dual linear polarization antenna arrays. *Antennas and Propagation, IEEE Transactions on*, 1997.
- [9] J. L. Wong H. E. King. A shallow ridged-cavity crossed-slot antenna for the 240- to 400-mhz frequency range. *IEEE Transactions on Antennas and Propagation*, Sep 1975.
- [10] K. M. Luk W. K. Lo, C. H. Chan. Bandwidth enhancement of circularly polarized microstrip patch antenna using multiple l-shaped probe feeds. *Microwave and Optical Technology Letters*, Jan 2004.
- [11] M. R. Pino P. Nepa G. Manara A. Buffi, R. Caso. A novel slot-coupling feeding technique for circularly polarized patch antennas. *IEEE*, 2010.
- [12] M. R. Pino P. Nepa G. Manara A. Buffi, R. Caso. Dual-polarized slot-coupled patch antenna excited by a square ring slot. *IET Microwaves, Antennas and Propagation*, 2010.

Bibliography

- [13] V. P. Meshchanov L. V. Shikova D. S. Gubin, A. P. Krenitskii. Synthesis of phase shifters based on a single stepped transmission line with a stub. *Journal of Communications Technology and Electronics*, May 2007.
- [14] J. F. Zurcher. The ssfp: a global concept for high-performance broadband planar antennas. *Electronics Letters*, 1988.
- [15] F. E. Gardiol J. F. Zurcher. *Broadband Patch Antennas*. Artech House, Inc., 1995.
- [16] Robert J. Mailloux. *Phased array antenna handbook*. Artech House, Inc., 1994.
- [17] E.G. Cristal and L. Young. Theory and tables of optimum symmetrical tem-mode coupled-transmission-line directional couplers. *Microwave Theory and Techniques, IEEE Transactions on*, 1965.
- [18] Robert B. Crane and C. B. Sharpe. Limitations of series-fed arrays in broadband communications. *Aerospace and Electronic Systems, IEEE Transactions on*, AES-2(6):659 –664, nov. 1966.
- [19] Tatsuo Itoh Christophe Caloz. *Electromagnetic Metamaterials*. John Wiley & sons, 2006.
- [20] M.A. Antoniadis and G.V. Eleftheriades. A negative-refractive-index transmission-line (nri-tl) leaky-wave antenna with reduced beam squinting. In *Antennas and Propagation Society International Symposium, 2007 IEEE*, pages 5817 –5820, june 2007.
- [21] H. Mirzaei and G.V. Eleftheriades. An active artificial transmission line for squint-free series-fed antenna array applications. In *Microwave Conference (EuMC), 2011 41st European*, pages 503 –506, oct. 2011.
- [22] M. A. G. Laso Txema Lopetegi Jose Azana David Plant Joshua D. Schwartz, Israel Arnedo. An electronic uwb continuously tunable time-delay system with nanosecond delays. *Antennas and Propagation Magazine, IEEE*, 2008.
- [23] R. C. Williamson V. S. Dolat. A continuously variable delay-line system. *Antennas and Propagation Magazine, IEEE*, 2007.
- [24] M. J. Erro D. Benito M. J. Garde M. A. Muriel M. Sorolla M. Guglielmi M. A. G. Laso, T. Lopetegi. Real-time spectrum analysis in microstrip technology. *Antennas and Propagation Magazine, IEEE*, 2001.
- [25] M. J. Erro D. Benito M. J. Garde M. A. Muriel M. Sorolla M. Guglielmi M. A. G. Laso, T. Lopetegi. Chirped delay lines in microstrip technology. *Antennas and Propagation Magazine, IEEE*, 2001.
- [26] M. Chudzik I. Arregui T. Lopetegi M. A. G. Laso A. Lujambio, I. Arnedo. Dispersive delay line with effective transmission-type operation in coupled-line technology. *Antennas and Propagation Magazine, IEEE*, 2011.
- [27] H.V. Nguyen, S. Abielmona, and C. Caloz. Analog dispersive time delayer for beam-scanning phased array without beam-squinting. In *Antennas and Propagation Society International Symposium, 2008. AP-S 2008. IEEE*, pages 1 –4, july 2008.

-
- [28] C. Liang C. W. Domier C. Luhmann C. C. Chang, R. P. Hsia. 2-dimensional nonlinear delay line-based phased antenna arrays. *Antennas and Propagation Magazine, IEEE*, 2000.
- [29] C. Liang C. W. Domier C. Luhmann C. C. Chang, R. P. Hsia. True time phased antenna array systems based on nonlinear delay line technology. *Antennas and Propagation Magazine, IEEE*, 2001.
- [30] J. Perruisseau-Carrier, R. Fritschi, and A.K. Skrivervik. Design of enhanced multi-bit distributed mems variable true-time delay lines. In *Research in Microelectronics and Electronics, 2005 PhD*, 2005.
- [31] E. Gandini, M. Ettorre, M. Casaletti, K. Tekkouk, L. Le Coq, and R. Sauleau. Siw slotted waveguide array with pillbox transition for mechanical beam scanning. *Antennas and Wireless Propagation Letters, IEEE*, 2012.
- [32] M. Ettorre, Erio Gandini, and R. Sauleau. Multi-beam pillbox antennas in the millimeter-wave range. In *Antennas and Propagation (EUCAP), Proceedings of the 5th European Conference on*, 2011.
- [33] J. D. Kraus. *Antennas, 1st ed.* New York: McGraw-Hill, 1950.
- [34] A. Ludwig. The definition of cross polarization. *Antennas and Propagation, IEEE Transactions on*, Jan 1973.
- [35] G. A. Deschamps. Microstrip microwave antennas. *3rd USAF Symp. on Antennas*, 1953.
- [36] H. Gutton and G. Baissinot. Flat aerial for ultra high frequencies. *3rd USAF Symp. on Antennas*, 1955.
- [37] Keith R. Carver and J. Mink. Microstrip antenna technology. *Antennas and Propagation, IEEE Transactions on*, 1981.
- [38] R.J. Mailloux, John F. McIlvenna, and N. Kernweis. Microstrip array technology. *Antennas and Propagation, IEEE Transactions on*, 1981.
- [39] Constantine A. Balanis. *Antenna Theory, Analysis and Design - third edition.* John Wiley & sons, New Jersey, 2005.
- [40] K.M. Luk K.F. Lee. *Microstrip Patch Antennas.* Imperial College Press, 2010.
- [41] R.S. Tomar P. Barthia, K.V.S Rao. *Millimeter-Wave Microstrip and Printed Circuit Antennas.* Artech House, Inc., 1991.
- [42] P. Hannan. The element-gain paradox for a phased-array antenna. *Antennas and Propagation, IEEE Transactions on*, 1964.
- [43] D.M. Pozar. The active element pattern. *Antennas and Propagation, IEEE Transactions on*, 1994.
- [44] S.D. Targonski, R.B. Waterhouse, and D.M. Pozar. Design of wide-band aperture-stacked patch microstrip antennas. *Antennas and Propagation, IEEE Transactions on*, 1998.

Bibliography

- [45] David M. Pozar. *Microwave engineering - second edition*. John Wiley & sons, New Jersey, 1998.
- [46] M. Muraguchi, T. Yukitake, and Y. Naito. Optimum design of 3-dB branch-line couplers using microstrip lines. *Microwave Theory and Techniques, IEEE Transactions on*, 1983.
- [47] Duxiang Wang, A. Huynh, P. Hakansson, Ming Li, and Shaofang Gong. Study of wideband microstrip 90°; 3-dB two-branch coupler with minimum amplitude and phase imbalance. In *Microwave and Millimeter Wave Technology, 2008. ICMMT 2008. International Conference on*, 2008.
- [48] Ihn Seok Kim Werner Arriola, Jae Young Lee. Wideband 3dB branch line coupler based on $\lambda/4$ open circuited coupled lines. *IEEE microwave components letters*, 2011.
- [49] David Lacombe Raymond Waugh. Unfolding the Lange coupler. *Microwave theory and techniques, IEEE Transactions on*, 1972.
- [50] Gordon Riblet. A directional coupler with very flat coupling. *Microwave theory and techniques, IEEE Transactions on*, 1983.
- [51] Julius Lange. Interdigitated stripline quadrature hybrid. *Microwave theory and techniques, IEEE Transactions on*, 1969.
- [52] B.F. Hornecker and J.R. Mosig. Practical issues related to the design of uwb directional couplers in stripline technology. In *Applied Electromagnetics and Communications (ICECom), 2013 21st International Conference on*, pages 1–4, Oct 2013.
- [53] P.S. Hall. Application of sequential feeding to wide bandwidth, circularly polarised microstrip patch arrays. *Microwaves, Antennas and Propagation, IEE Proceedings H*, Oct 1989.
- [54] M.S. Smith. Grating lobes of sequentially rotated antenna arrays. In *Antennas and Propagation, 1991. ICAP 91., Seventh International Conference on (IEE)*, 1991.
- [55] P.S. Hall and M.S. Smith. Sequentially rotated arrays with reduced sidelobe levels. *Electronics Letters*, 1992.
- [56] L. C. Ong Y. X. Guo, K. W. Khoo. Ultra-wideband circularly-polarized patch antenna. *Proceedings of Asia-Pacific Microwave Conference*, 2006.
- [57] L. C. Ong X. Q. Shi L. Bian, Y. X. Guo. Wideband circularly-polarized patch antenna. *IEEE Transactions on Antennas and Propagation*, 2006.
- [58] L. C. Ong Y. X. Guo, K. W. Khoo. Wideband circularly polarized patch antenna using broadband baluns. *Proceedings of Asia-Pacific Microwave Conference*, 2008.
- [59] B.M. Schiffman. A new class of broad-band microwave 90-degree phase shifters. *Microwave Theory and Techniques, IRE Transactions on*, April 1958.
- [60] T. K. Sarkar M. Salazar-Palma S. H. Yeung, Z. Mei. Design and testing of a single-layer microstrip ultrawideband 90° differential phase shifter. *IEEE Microwave and Wireless Components Letters*, Mar 2013.

-
- [61] A. Abbosh L. Guo. Multilayer phase shifter with wide range of phase and ultra-wideband performance. *Asia-Pacific Microwave Conference Proceedings*, 2013.
- [62] A. Abbosh L. Guo. Phase shifters with wide range of phase and ultra-wideband performance using stub-loaded coupled structure. *IEEE Microwave and Wireless Components Letters*, 2013.
- [63] W. S. Chan S. H. Yeung, K. F. Man. The multiple circular sectors structures for phase shifter designs. *IEEE Transactions on Microwave Theory and Techniques*, Feb 2011.
- [64] K. F. Man S. Y. Zheng, W. S. Chan. Broadband phase shifter using loaded transmission line. *Microwave and Wireless Components Letters, IEEE*, Sep 2010.
- [65] Man K. F. Zheng S. Y., Chan W. S. Broadband parallel stubs phase shifter. In *Microwave Conference, 2009. APMC 2009. Asia Pacific*, Dec 2009.
- [66] B.F. Hornecker, M.G. Vigueras, and J.R. Mosig. Wideband dual-circularly polarized patch antenna sequentially-fed through a ring slot. In *Antennas and Propagation Conference (LAPC), 2014 Loughborough*, Nov 2014.
- [67] M.W. McAllister and S.A. Long. Resonant hemispherical dielectric antenna. *Electronics Letters*, 20(16):657 –659, 2 1984.
- [68] Pierre Guillon Darko Kajfez. *Dielectric Resonators*. Artech House, Inc., 1986.
- [69] J. Van Bladel. The excitation of dielectric resonators of very high permittivity. *Microwave Theory and Techniques, IEEE Transactions on*, 23(2):208 – 217, feb 1975.
- [70] S. Long, M. McAllister, and Liang Shen. The resonant cylindrical dielectric cavity antenna. *Antennas and Propagation, IEEE Transactions on*, 31(3):406 – 412, may 1983.
- [71] Aldo Petosa. *Dielectric Resonator Antenna Handbook*. Artech House, Inc., 2007.
- [72] J. R. James K. M. Luk, K. W. Leung. *Dielectric Resonator Antennas*. Research studies press, UK, 2002.
- [73] A. Petosa and A. Ittipiboon. Dielectric resonator antennas: A historical review and the current state of the art. *Antennas and Propagation Magazine, IEEE*, 52(5):91 –116, oct. 2010.
- [74] Georgios Almpanis. *On the geometry and the coupling schemes of broadband dielectric resonator antennas*. PhD thesis, Swiss Federal Institute of Technology, 2009.
- [75] Yong-Xin Guo, Kwai-Man Luk, and Kwok-Wa Leung. Mutual coupling between millimeter-wave dielectric-resonator antennas. *Microwave Theory and Techniques, IEEE Transactions on*, 47(11):2164 –2166, nov 1999.
- [76] A. Petosa, S. Thirakoun, M. Zuliani, and A. Ittipiboon. Comparison between planar arrays of perforated dras and microstrip patches. In *Antennas and Propagation Society International Symposium, 2005 IEEE*, volume 2A, pages 168 – 175 vol. 2A, july 2005.
- [77] Murata, 2012. Dielectric Resonators (RESOMICS) - Technical Datasheet.




Bibliography

- [78] A. Petosa, A. Ittipiboon, and S. Thirakoune. Perforated dielectric resonator antennas. *Electronics Letters*, 38(24):1493 – 1495, nov 2002.
- [79] A. Petosa, S. Thirakoune, and A. Ittipiboon. Array of perforated dielectric resonator antennas. In *Antennas and Propagation Society International Symposium, 2004. IEEE*, volume 1, pages 1106 – 1109 Vol.1, june 2004.
- [80] S.H. Zainud-Deen, S.M. Gaber, A.M. Abd-Elhady, K.H. Awadalla, and A.A. Kishk. Wide-band perforated rectangular dielectric resonator antenna reflectarray. In *Antennas and Propagation (APSURSI), 2011 IEEE International Symposium on*, pages 113 –116, july 2011.
- [81] M. Abd-Elhady, Wei Hong, and Yan Zhang. A ka-band reflectarray implemented with a single-layer perforated dielectric substrate. *Antennas and Wireless Propagation Letters, IEEE*, 11:600 –603, 2012.
- [82] Bin Li and Kwok-Wa Leung. Strip-fed rectangular dielectric resonator antennas with/without a parasitic patch. *Antennas and Propagation, IEEE Transactions on*, 2005.
- [83] Bin Li and Kwok-Wa Leung. On the differentially fed rectangular dielectric resonator antenna. *Antennas and Propagation, IEEE Transactions on*, 2008.
- [84] B. Li, K.W. Leung, and X.Q. Sheng. Differentially fed rectangular dielectric resonator antenna. 2008.
- [85] B.F. Hornecker and J.R. Mosig. High profile rectangular dielectric resonator antenna sequentially-fed for improved quality dual circular polarization. In *Antennas and Propagation (EuCAP), 2015 9th European Conference on*, pages 1–5, April 2015.
- [86] R. Glogowski, J.-F. Zurcher, C. Peixeiro, and J.R. Mosig. A low-loss planar ka-band antenna subarray for space applications. *Antennas and Propagation, IEEE Transactions on*, Sept 2013.
- [87] R. Glogowski, J. Zurcher, J.R. Mosig, and C. Peixeiro. Circularly polarized aperture coupled stacked patch antenna element for ka-band. In *Antennas and Propagation (APSURSI), 2011 IEEE International Symposium on*, July 2011.
- [88] N.H. Noordin, A.O. El-Rayis, N. Haridas, B. Flynn, A.T. Erdogan, and T. Arslan. Triangular lattices for mutual coupling reduction in patch antenna arrays. In *Antennas and Propagation Conference (LAPC), 2011 Loughborough*, pages 1–4, Nov 2011.
- [89] Edgar Lopez-Luna Heber Hernandez-Arriaga Gabriel Gonzalez, Eleazar Samuel Kolosovas-Machuca and Francisco Javier Gonzalez. Design and fabrication of interdigital nanocapacitors coated with hfo₂. *Open Access Sensors*, 2015.
- [90] H. Shao M. A. Ebrish and S. J. Koester. Operation of multi-finger graphene quantum capacitance varactors using planarized local bottom gate electrodes. *Applied Physics Letters*, 2012.
- [91] Huili Xing Debdeep Jena Tian Fang, Aniruddha Konar. Carrier statistics and quantum capacitance of graphene sheets and ribbon. *Applied Physics Letters*, 2007.

- [92] S. Lopez-Pena and J. R. Mosig. Analytical evaluation of the quadruple static potential integrals on rectangular domains to solve 3-d electromagnetic problems. *Progress In Electromagnetics Research*, 2009.
- [93] A. G. Polimeridis S. Lopez-Pena and J. R. Mosig. On the double potential integrals arising in the method of moments and their analytic-numeric hybrid treatment. *IEEE Transactions on Electromagnetics Reasearch*, 2011.
- [94] John D. Jackson. *Classical Electrodynamics*. John Wiley & sons, New Jersey, 1962.
- [95] J. Mosig. The weighted averages algorithm revisited. *Antennas and Propagation, IEEE Transactions on*, 2012.
- [96] T. Sometani. Image method for a dielectric plate and a point charge. *European Journal of Physics*, 2000.

Baptiste Hornecker

Etudiant doctorant (Génie électrique)
Laboratoire d'ElectroMagnétisme et d'Antennes (LEMA)
Ecole Polytechnique Fédérale de Lausanne (EPFL), Suisse.

Contact  ELB-034, STI-IEL-LEMA, Station 11, EPFL, 1015 Lausanne, Suisse
 +41 216934631
 baptiste.hornecker@epfl.ch

Web <http://people.epfl.ch/baptiste.hornecker>

Divers Né le 10/09/1988 à Strasbourg
Nationalité française
Permis de Conduire B

FORMATION

- 2012 – Actuel** Etudiant doctorant à l'Ecole Polytechnique Fédérale de Lausanne (EPFL), Suisse
Directeur de thèse: Prof. Juan R. Mosig (EPFL, LEMA)
Co-directeur: Dr. Nicolas Vukadinovic
- 2008 – 2011** Diplômé de l'Institut National des Sciences Appliquées (INSA) de Strasbourg
Département de Génie Electrique à l'INSA de Strasbourg
Obtention du TOEIC (score : 955 / 990)
- 2006 – 2008** Classe Préparatoire Intégrée à l'INSA de Strasbourg
- Vice-Major de Promotion aux Second et Dernier Semestres
 - Premier admissible au concours de l'ENS Cachan (3A – Génie Electrique)
- 2006** Baccalauréat Scientifique Option Mathématiques – Mention Bien
- 2003** Obtention du Certificat Régional d'Excellence en Allemand (CREA)

EXPÉRIENCES

- Hiver 2015** Stage de deux mois à *Dassault Aviation, Saint-Cloud, sur l'emploi du logiciel SPECTRE pour la simulation de grands réseaux par la méthode de factorisation*
- 2011** Projet de Fin d'Etudes au Laboratoire d'ElectroMagnétisme et d'Antennes intitulé *Power Transmission System for Satellites Using Microwave Beams*. Note finale : 19.5/20
- 2010** Stage Technicien de deux mois sur le drone « Cigogne » de l'INSA : Travail sur la carte électronique dédiée à la transmission au sol de la vidéo embarquée
- 2009** Stage ouvrier de cinq semaines dans la chocolaterie industrielle CFCC SCHAAL à Illkirch

ENSEIGNEMENT

- Assistant des cours d'électromagnétisme et d'antennes depuis 2012 (EPFL)
- Assistant examinateur des examens oraux de Photonique 2014-2015
- Reviewer pour la conférence Eucap 2016 (Lisbonne)

COURS D'ECOLE DOCTORALE

- European School of Antennas (ESoA) "**mm-Wave Antenna Design and Technologies**", Rennes 21-25 Mai 2012
- European School of Antennas (ESoA) "**Frequency Domain Techniques for Antenna Analysis**", Florence 16-20 Septembre 2013
- Cours EPFL "**Digital Speech and Audio Coding**", Automne 2012 (Prof. Magimai Doss Mathew et Motlicek Petr)
- Cours EPFL "**Advanced topics in microwaves and antennas**", Printemps 2013 (Prof. Anja Skrivervik et Dr. Zürcher Jean-François)
- Cours EPFL "**Integral equations in Electromagnetics**", Printemps 2014 (Prof. Juan R. Mosig)

COMPETENCES GENERALES

Langues

Français : langue maternelle

Anglais : courant (oral et écrit) pour tout type de conversation

Allemand : niveau scolaire / académique

Electromagnétisme

- Conception d'antennes par simulation numérique (logiciels HFSS, CST, Ansoft Designer, SPECTRE de Dassault Aviation)
- Prototypage d'antennes
- Caractérisation hyperfréquence d'antennes

Informatique / Electronique

Bon niveau : Langage C, Administration Linux en général, Matlab, LaTeX, Microcontrôleurs PIC (environnement Microchip)

Notions : Catia, VHDL, Quartus, FPGA, Cadence Software, Java, PHP, Delphi (Pascal), Réseaux et Sécurité

CONFERENCES INTERNATIONALES

- B. F. Hornecker, J. R. Mosig, "High Profile Rectangular Dielectric Resonator Antenna Sequentially-fed For Improved Quality Dual Circular Polarization", 9ème *European Conference on Antennas and Propagation (EuCAP)*, Lisbonne, 2015.
- B. F. Hornecker, M. Garcia Viguera, J. R. Mosig, "Wideband Dual-Circularly Polarized Patch Antenna Sequentially-fed Through a Ring Slot", 10ème *Loughborough Antennas and Propagation Conference (LAPC)*, Loughborough, 2014.
- B. F. Hornecker, J. R. Mosig, "Practical Issues Related to the Design of UWB Directional Couplers in Stripline Technology", 20ème *International Conference on Applied Electromagnetics and Communications (ICECOM)*, Dubrovnik, 2013.

CENTRES D'INTERÊTS GENERAUX

- Histoire de France et de l'Europe
- Histoire des Sciences
- Tennis de Table pratiqué en club plusieurs années